



Title	Effect of Reaction Environment on Photo-driven Catalytic Properties
Author(s)	孟, 憲光
Citation	北海道大学. 博士(理学) 甲第12037号
Issue Date	2015-09-25
DOI	10.14943/doctoral.k12037
Doc URL	http://hdl.handle.net/2115/59992
Type	theses (doctoral)
File Information	Meng_Xianguang.pdf



[Instructions for use](#)



Effect of Reaction Environment on Photo-driven Catalytic Properties

(反応環境場の制御による光触媒特性への影響に関する研究)

Xianguang Meng

Graduate School of Chemical Sciences and Engineering

Hokkaido University

2015

CONTENTS

Contents	I
Abstract	1
Chapter 1 Introduction	5
1.1 General introduction	5
1.2 Construction of heterogeneous photocatalysts and their limitations	6
1.3 Photocatalytic reactions: materials and reaction environment modulation	8
1.3.1 Photocatalytic degradation	9
1.3.2 Photocatalytic H ₂ evolution	11
1.3.3 Photocatalytic CO ₂ conversion	13
1.4 Application of plasmonic effect in photo-driven catalysis	14
1.5 Research motivations and thesis organization	21
References	24
Chapter 2 Enhancement of photocatalytic activity for WO₃ by NaOH loading	30
2.1 Introduction	30
2.2 Experimental methods	31
2.2.1 Photocatalyst preparation	31
2.2.2 Sample characterization	32
2.2.3 Photocatalytic degradation in gas phase	32
2.3 Results and discussion	33

Contents

2.3.1 Crystal structure	33
2.3.2 Optical absorption property	34
2.3.3 Energy band alignment	35
2.3.4 Photocatalytic activity and reaction mechanism	37
2.4 Conclusions	45
References	46
Chapter 3 Enhancement of H₂ production in alkaline environment over plasmonic Au/TiO₂ photocatalysts	48
3.1 Introduction	48
3.2 Experimental methods	50
3.2.1 Photocatalyst preparation	50
3.2.2 Sample characterization	52
3.2.3 Photocatalytic H ₂ evolution	52
3.2.4 Photoelectrochemical measurements	53
3.3 Results and discussion	54
3.3.1 Sample characterization and photocatalytic activity	54
3.3.2 Photoelectrochemical measurements	61
3.4 Conclusions	64
References	64
Chapter 4 Photocatalytic CO₂ reduction into CH₄ over alkali modified TiO₂ without loading noble metal cocatalysts	67
4.1 Introduction	67
4.2 Experimental methods	68
4.2.1 Photocatalyst preparation	68

Contents

4.2.2 Sample characterization	68
4.2.3 Photocatalytic CO ₂ conversion	69
4.3 Results and discussion	70
4.3.1 Photocatalytic activity and sample characterization	70
4.3.2 Photocatalytic reaction mechanism	73
4.4 Conclusions	78
References	79
Chapter 5 Plasmon-mediated CO₂ activation and conversion with active hydrogen source	81
5.1 Introduction	81
5.2 Experimental methods	83
5.2.1 Catalyst preparation	83
5.2.2 Sample characterization	84
5.2.3 Photothermal CO ₂ conversion with H ₂	84
5.2.4 CO ₂ reforming with CH ₄ under visible light	85
5.3 Results and discussion	86
5.3.1 Photothermal CO ₂ conversion with H ₂	86
5.3.2 CO ₂ reforming with CH ₄ under visible light	92
5.3.3 Optical simulations and the mechanism of enhanced activity	96
5.4 Conclusions	100
References	101
Chapter 6 General conclusions and future prospects	103
6.1 General conclusions	103

Contents

6.2 Future prospects	105
References	108
Acknowledgement	110

Abstract

Photocatalysis is a green technology and has attracted extensive attentions due to its potential applications for solar-to-chemical energy conversion. However, great efforts are still needed to further increase the efficiency of current photocatalytic system for practical application. Previous work mainly focused on how to design efficient photocatalysts to enhance the photocatalytic performances. In this work, the research target is to investigate how reaction environment modulates the photocatalytic performance of current reaction system. The reaction environments herein include both the chemical and physical reaction environments which can exert positive effects on increasing the photocatalytic activity. Especially, the influence of a simple chemical reaction environment, alkaline reaction environment, on various photocatalytic reactions, including photocatalytic degradation, H₂ evolution, and CO₂ conversion was studied. Moreover, the influence of a photophysical phenomenon, surface plasmon resonance (SPR) on highly efficient CO₂ conversion with H₂ and CH₄ was investigated.

Chapter 1 gave a general introduction of the material design of heterogeneous photocatalyst, the typical photocatalytic reactions related to this work, and the significance of reaction environment modulation in enhancing the photocatalytic performance.

Chapter 2 investigated the influence of NaOH (solid base) loading on the photocatalytic performance of WO₃ for gaseous organics degradation under visible light. The influence of NaOH loading on photocatalytic reactions included two

Abstract

aspects. The first was that NaOH changed the surface crystal structure through mild reaction with WO_3 (an acidic oxide) surface and lifted the surface energy band position of photocatalyst. This promoted the oxygen reduction ability of conduction band electrons during the photocatalytic degradation. Secondly, it is well known that H_2O_2 , an important intermediate in photocatalytic degradation, is very unstable in alkaline environment. Therefore, the loading of NaOH on the surface of WO_3 promoted the decomposition of H_2O_2 . Since the accumulation of H_2O_2 suppressed the consumption of photoexcited electrons on WO_3 , NaOH loading overcame this drawback and enhanced the photocatalytic degradation.

In addition to the photocatalytic degradation, an alkaline reaction environment is also favorable for photocatalytic H_2 production and CO_2 reduction, as shown in chapter 3 and 4. Since the two reactions generally require the semiconductor with high conduction band positions, TiO_2 was used as the main component of photocatalysts in these studies.

The alkaline reaction environment enhanced deprotonation process in electrooxidation of alcohol over Au electrodes has been reported in the previous electrocatalysis studies. In Chapter 3, this function was employed for photocatalytic H_2 evolution over plasmonic Au/ TiO_2 composites. Under the excitation of Au SPR band in the visible light range, H_2 production was remarkably boosted over Au/ TiO_2 /Pt photocatalyst in alkaline reaction environment. The photoelectrochemical studies showed that alkaline environment promoted the photooxidation of alcohol over plasmonic Au nanoparticles (NPs), which accelerated the consumption of holes in Au NPs.

Due to the acidic nature of CO_2 molecules, loading of alkali on photocatalyst will promote the chemisorption and possible activation of CO_2 . This found application in

Abstract

the photocatalytic CO₂ reduction over TiO₂ in chapter 4. Surface modification of TiO₂ with NaOH was found to be an effective way for the CO₂ adsorption, activation, and led to highly effective conversion of CO₂ into CH₄ without loading any noble metal cocatalyst.

In order to further enhance the current CO₂ conversion efficiency, H₂ and CH₄ were used as hydrogen sources for CO₂ conversion in chapter 5. The influences of SPR-induced photothermal or local electric field on these reactions were investigated. The results showed that CO₂ conversion with these hydrogen sources achieved much superior efficiency to water. Compared with photothermal CO₂ conversion with H₂ over Ru nanocatalyst, CH₄ is a more promising hydrogen source due to an uphill reaction. In the reaction of CO₂ reforming of CH₄, Au NPs were used as plasmonic promoter and co-loaded with Rh nanometal catalyst on SiO₂. Rh NPs only shows UV plasmonic behavior and its SPR effect cannot be induced by visible light irradiation. Therefore, conventional Rh catalyst does not show photoenhanced activity for CO₂ reforming of CH₄. When co-loaded with Au NPs, an enhanced SPR effect was induced by interparticle coupling effect between Au and Rh NPs under the visible light irradiation in the SPR band of Au NPs. Accordingly, photoenhanced activity was observed over Au and Rh co-loaded catalysts. During the decay of SPR, some meaningful process, such as the hot electron production, surface polarization, electronic disturbance, or local heating effect will make positive effect on CO₂ reforming of CH₄. Especially, the results show that the SPR effect plays important role on CO₂ activation during the reforming reaction.

In summary, this thesis revealed the significance of surface reaction environment on photocatalytic reactions. The function of surface reaction environment was realized through changing the photocatalyst itself or the photocatalytic reaction

Abstract

pathway. The results of this thesis demonstrated that modulation of surface reaction environment was a promising strategy for enhancing the performance of current photocatalytic reaction systems.

Chapter 1 Introduction

1.1 General introduction

Solar-to-chemical energy conversion is an important research field due to its great significance in solving both energy and environment issues of today. As one of the most potential green technologies, photocatalysis has been studied for several decades and made substantial progress in some important research subjects, such as environment purification,¹⁻³ water splitting,⁴⁻⁷ CO₂ reduction,^{8, 9} organic photosynthesis and transformations,^{10, 11} photocatalytic material design,¹²⁻¹⁴ etc. Photocatalysis utilizes the photogenerated carriers (electrons and holes) to initiate the redox reactions and realize the solar-to-chemistry energy conversion. A typical process of photocatalytic reactions over semiconductors is shown in Fig. 1.1.¹³ The semiconductor is firstly excited by photons to produce electrons and holes at conduction band (CB) and valence band (VB), respectively. These e⁻/h⁺ pairs will partially recombine in the semiconductors and the rest will migrate to the surface to drive the redox reactions. A precondition for a photocatalytic reaction to occur is that the CB and VB level of semiconductor should be more negative or positive than the corresponding reduction or oxidation reaction potential, respectively.

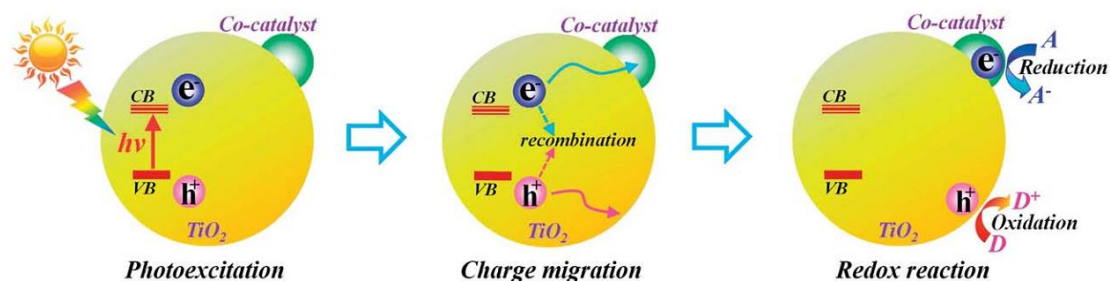


Fig. 1.1. Schematic process of photocatalytic reaction (TiO_2 as example).¹³

1.2 Construction of heterogeneous photocatalysts and their limitations

Semiconductor materials have dominated the study of photocatalysis in history. Semiconductor photocatalysts generally consist of metal cations with d^0 or d^{10} configurations, and the anions such as O, S, N, etc. (Fig. 1.2).¹⁴ Ti, V, Nb, Ta, Mo, and W are typical elements for d^0 cations. Cu, Ag, Zn, Cd, Ga, In, Ge, Sn, Pd, and Bi are typical elements for d^{10} cations. The empty d orbitals (for metal cations with d^0 configurations) and the empty s or sp orbitals (for metal cations with d^{10} configurations) generally construct the CB of photocatalysts. The p orbitals of O, S, and N anions generally construct the VB of photocatalysts. Orbitals of $\text{Cu}3d$ in Cu^+ , $\text{Ag}4d$ in Ag^+ and the s orbital in the low valence p-block elements Sn^{2+} , Pb^{2+} , and Bi^{3+} can also construct VB. Ti, Nb, Ta, Ga, and Ge are important elements to construct the photocatalysts with high CB levels and thus often used for photocatalytic H_2 evolution. V, W, Ag, and Bi are typical elements to construct visible light active photocatalysts with low CB level and thus extensively used for photocatalytic degradation and O_2 evolution from water oxidation. Some transition metal cations such as Cr^{3+} , Ni^{2+} and Rh^{3+} with partially filled d orbitals are generally used as doping elements to form

Chapter 1

impurity levels in the band gaps of host semiconductors and obtain visible light response. Semiconductors with wide band gap can form solid solutions with another narrow band gap semiconductor with similar crystal parameters. The solid solution design can be used to modulate the band gaps (e. g., $(\text{AgNbO}_3)_{1-x}(\text{SrTiO}_3)_x$ ¹⁵, $\text{AgAl}_{1-x}\text{Ga}_x\text{O}_2$ ², etc.). Doping or solid solution design are typical strategies in energy band engineering for the creation of new photocatalysts with visible light response. Because N 2p orbital is higher than O2p, oxynitrides derived from the nitridation of related oxides generally have good visible light response by lifting the VB level. Besides the elements mentioned in Fig. 1.2, other elements, such as C (e.g., C_3N_4)¹⁶, Al (e.g., $\text{AgAl}_{1-x}\text{Ga}_x\text{O}_2$)², P (e.g., Ag_3PO_4)⁶, and Sb (e.g., AgSbO_3)¹⁷ are also used to construct photocatalysts.

Over the past several decades, substantial progress has been made on the design of new photocatalytic materials on the basis of current elements on earth. The limited photoabsorption and low apparent quantum efficiency (AQE) are still two major bottlenecks for the large scale application of semiconductor photocatalysis. The former is determined by the inherent energy band structure of a semiconductor and the latter is mainly caused by the recombination of photogenerated charge carriers. Although the energy band engineering is effective to increase the photoabsorption of current semiconductors, this strategy will possibly cause the crystal defects in semiconductors and further lower the AQE. Compared with the great challenge in designing new photocatalytic materials, modulation of reaction environment provides a promising strategy to enhance the photocatalytic performance.

environment on photocatalytic property will be introduced.

1.3.1 Photocatalytic degradation

Many kinds of harmful organic compounds exist in our daily life and often damage our health. Photocatalysis is a useful technology for removing these harmful organic compounds. In the photocatalytic degradation, the organic pollutant is oxidized by the VB holes and the CB electrons are consumed by O_2 . Although this reaction is always called “photocatalytic degradation” of organic pollutants, if photogenerated electrons are not consumed effectively, these electrons will recombine easily with holes, leading to a decrease in the photocatalytic activity or deactivation of a photocatalyst. In fact, the bottleneck of most of the photocatalytic degradation reactions lies in the oxygen reduction by the CB electrons of semiconductors rather than the oxidation of contaminants, because the oxidation power of the photogenerated holes in the VB of semiconductors is generally sufficient enough to oxidize most of organic compounds.² The redox potentials of single electron oxygen reduction reaction (ORR) ($O_2 + e^- = O_2^-$ (aq), -0.284 V vs SHE; $O_2 + H^+ + e^- = HO_2$ (aq), -0.046 V vs. SHE) are higher (or more negative) than that of multi-electron ORR ($O_2 + 2H^+ + 2e^- = H_2O_2$ (aq), +0.682 V vs. SHE; $O_2 + 4H^+ + 4e^- = 2H_2O$, +1.23 V vs. SHE).²⁴ In the absence of Pt cocatalyst (electron sinks), multi-electron ORR is kinetically unfavorable, and single electron reduction of adsorbed oxygen is generally a control step of the overall reaction rate of photocatalytic degradation. The loaded Pt cocatalyst not only serves as electron sink to accumulate electrons from semiconductor but also provides the active site for the fast multi-electron ORR. This will dramatically enhance reaction rate of photocatalytic degradation. The role of Pt cocatalyst is in particular crucial in improving the photocatalytic performance of semiconductor with low CB position. For example, WO_3 is a visible-light-active photocatalyst with simple composition. However, the CB level of

Chapter 1

WO₃ is very low (~0.5 eV) and thermodynamically unfavorable for single electron ORR. In the absence of cocatalysts, both single electron and multi-electron ORR can hardly proceed. After loading Pt, the fast multi-electron ORR pathway is opened up and thus highly efficient photocatalytic degradation can be achieved.²⁴ Due to the high cost of noble metal cocatalysts, photocatalysts and cocatalysts with cheap elements should be developed for the large scale application. Maybe the most practical photocatalysts for gaseous organics decomposition is Cu or Fe grafted TiO₂ (or doped TiO₂) or WO₃ semiconductors which show outstanding photocatalytic performance under visible light.²⁵⁻²⁷ Grafting CuO_x and FeO_x species as cocatalyst on the surface of TiO₂ or WO₃ plays the vital role for the separation of photogenerated electrons to improve the performance of the two low cost photocatalysts under visible light.

The photocatalytic degradation can be enhanced by proper surface treatment. Fluorinated TiO₂ was reported to show better dispersion stability than untreated TiO₂ particles in water since surface fluorination induced a more negative ζ potential on TiO₂ particles.²⁸ The surface anchored F⁻ anions on TiO₂ can effectively adsorb positively charged groups of some molecules, such as Rhodamine B, and promote the photocatalytic degradation to these pollutants.²⁹ In addition to surface fluorination, surface acidification was also reported as an effective method for enhancing the photocatalytic degradation. Wang and co-workers reported that surface acidification accelerated the photocatalytic aerobic oxidation of alcohols over TiO₂.³⁰ During photocatalytic aerobic oxidation of alcohols, a Ti intermediate, with a side-on peroxide, are formed, which can passivate the surface of TiO₂ and deactivate its activity. The protons of Brønsted acids promoted decomposition of the relatively stable peroxide because the protonation of peroxide remarkably weakens the O-O bond. The same group also reported that addition of acids in the aqueous system could

Chapter 1

change the reaction pathway of ORR.²³ The monocarboxylic and polyprotic acids played different role in ORR process. Polyprotic acids promoted the direct four-electron reduction of O₂ to H₂O on TiO₂ surfaces. In contrast, monocarboxylic acids only enhanced the ORR rate and H₂O₂ formation (by two-electron ORR) but barely changed the reaction pathway of ORR. Therefore, surface reaction environment modulation is an effective and flexible method to enhance the photocatalytic degradation.

1.3.2 Photocatalytic H₂ evolution

Photocatalytic H₂ evolution can be realized in pure water systems or the system containing sacrificial reagents. Photocatalytic H₂ evolution from overall water splitting involve the reduction of H⁺ by CB electrons and the oxidation of water by VB holes. In this case, O₂ will evolve at the same time with stoichiometric ratio of H₂:O₂ = 2:1. In the system containing sacrificial reagents, alcohol or sulfide ion acts as electron donor or hole scavenger. These electron donors are easily photooxidized and thus increase the number of photogenerated electrons to promote H₂ evolution rate.

Pt cocatalyst can greatly enhance the rate of photocatalytic H₂ evolution reaction (HER) from aqueous solutions containing sacrificial alcohol reagent, while HER is difficult to proceed over pure semiconductors. On one hand, Pt has largest work function (~5.65 eV) among all the noble metals with excellent trapping ability for electrons to realize effective separation of photo-generated carriers. On the other hand, Pt shows the best activation ability for proton reduction due to the appropriate metal-hydrogen bond strength according to the characteristic “volcano” relation.^{31,32} Therefore, Pt is generally regarded as the best cocatalyst for photocatalytic HER. Other noble metals (Rh, Pd, Au, etc.) with large work functions are also good cocatalysts for photocatalytic HER. For

Chapter 1

overall water splitting (photolysis of pure water), however, Pt and other noble metal cocatalysts can efficiently catalyse the recombination of H₂ and O₂ and special attention should be paid to the direct use of these cocatalysts in overall water splitting. Previous studies showed that RuO₂ and IrO₂ were proper single cocatalysts for overall water splitting.^{33,34}

Reaction environment also has important influence on photocatalytic H₂ evolution. Arakawa and co-worker reported that photocatalytic overall water splitting over Pt/TiO₂ photocatalyst could be improved by the addition of substantial amount of carbonate salts into the reaction solution.³⁵ The reaction condition for this enhancement is very limited: ~2 mol/L Na₂CO₃, pH 10-11, 0.3 wt% of Pt loading, and low pressure in reactor. It was supposed that the added carbonates suppressed the back reaction (water formation from the recombination of H₂ and O₂) and promoted desorption of O₂ from TiO₂ surface. The author also proposed that carbonate salt consumed the VB holes of TiO₂ to give peroxocarbonates species and mediated the O₂ evolution. Wagner and somorjai also reported the photocatalytic H₂ production from water on Pt-free STO in concentrated NaOH solutions.³⁶ Hydroxide ions adsorbed on the surface of STO served as hole acceptor and suppressed the recombination of electrons and holes. Modulation of alkaline environment also found application for photocatalytic H₂ evolution over semiconductors in sacrificial system containing alcohol. Ouyang and Simon respectively reported the enhanced H₂ evolution over Pt/STO and Ni/CdS photocatalysts in alkaline environment.^{21, 22} The enhanced photocatalytic H₂ production in alkaline environment is proposed to benefit from the non-Nernstian dependence of the band edges shift of semiconductors on the pH of reaction system (i.e., slope \neq -0.059 V/pH). The former proposed that the surface band of STO shifted exponentially with increasing alkalinity of the reaction solution. Since the HER potential shifts linearly

Chapter 1

versus the pH, the surface band of STO will get ahead of HER potential and increase the overpotential for photocatalytic H₂ evolution. While the latter proposed that the surface band of CdS shifted linearly versus the pH (slope = -0.033 V/pH). In the high pH value, the VB potential of CdS is positive enough to oxidize OH⁻ into [•]OH radicals which react quickly with sacrificial ethanol. In this case, the reaction pathway of ethanol oxidation was changed from direct oxidation by holes into indirect oxidation by [•]OH radicals, which promoted the photocatalytic H₂ evolution rate. Therefore, the reaction environment modulation can be a multifunctional strategy for enhancing the photocatalytic H₂ evolution, including suppression of the back reaction, changing the reaction pathway, or modulating the surface band of a semiconductor photocatalyst.

1.3.3 Photocatalytic CO₂ reduction

Solar fuel production through CO₂ conversion is a hot topic in recent years. CO₂ is one of the most stable compounds of carbon. Gaseous CO₂ molecule has a linear structure without dipole moment and is extraordinarily difficult to activate, which can be reflected by the much negative redox potential of one-electron reduction of CO₂ into CO₂^{•-} (-1.9 V vs RHE).^{37, 38} There is growing awareness that this single electron reduction is the key step for CO₂ activation to initiate the subsequent CO₂ conversion process.³⁷⁻³⁹ Another difficulty is that CO₂ conversion into hydrocarbon compounds is generally a proton-coupled electron transfer process (PCET). For example, CO₂ conversion into CH₄ needs the concerted transfer of 8 protons coupled with 8 electrons. This will lead to significant kinetic limitation for the CO₂ reduction process. Theoretically, semiconductor photocatalysts can provide electrons to CO₂ by photoexcitation but generally are incapable of donating protons concertedly with the electron transfer. At least, effective PCET mechanism on semiconductor

Chapter 1

photocatalysts are rarely reported.⁴⁰ Therefore, photocatalytic CO₂ conversion remains very inefficient because of the limited ability of conventional semiconductor to activate thermodynamically stable CO₂ molecules and the kinetic limitation of multiple e⁻/H⁺ transfer process. In addition, because of the obvious uphill reaction characteristic of CO₂ conversion with H₂O (CO₂ + H₂O → hydrocarbon compounds + O₂), suppression of the reverse reaction (oxidation of hydrocarbon compounds) should be carefully considered in an artificial photosynthetic system.

The reports of the influence of reaction environment on photocatalytic CO₂ conversion are very few. Due to the acidic nature of CO₂, alkaline solution is generally used in photocatalytic CO₂ conversion to increase the adsorption capacity of the liquid phase to CO₂.⁴¹ Alkaline oxides were also used as promoter for photocatalytic CO₂ conversion in gas phase. Xie and co-workers reported that photocatalytic reduction of CO₂ over Pt/TiO₂ could be enhanced by addition of MgO and other alkaline oxides.⁴² A synergistic effect between Pt and MgO was proposed. Firstly, CO₂ is chemisorbed on MgO promoter. This adsorption process changed the structure of linear CO₂ molecule and increased its reactivity. Then, the adsorbed CO₂ was further reduced into CH₄ by the accumulated electrons on Pt cocatalysts. Therefore, alkaline environment modulation seems a promising strategy and can be employed in the future studies of photocatalytic CO₂ reduction.

1.4 Application of plasmonic effect in photo-driven catalysis

Metallic nanocatalysts have been extensively used in catalysis industry for hydrogenation, dehydrogenation, oxidation, organic synthesis, etc. Today, nanometals find applications in photo-assisted heterogeneous catalysis through the well-known surface plasmon resonance (SPR) effect. The SPR can be described as the resonant

Chapter 1

photon-induced collective oscillation of valence electrons, established when the frequency of photons matches the natural frequency of surface electrons oscillating against the restoring force of positive nuclei.⁴³ The solar-to-chemical energy conversion over plasmonic metal NPs is realized through the SPR effect. Being different from the nanometal cocatalysts used in the research domain of semiconductor photocatalysis, plasmonic metal NPs themselves can render the excited carriers for redox reaction in plasmonic photocatalysis or photothermal effect in plasmonic photothermocatalysis. The plasmonic photocatalysis can be further classified into two categories:⁴⁴ (i) direct plasmonic photocatalysis, where plasmonic metal NPs act as the light absorber and the catalytically active site independently and (ii) indirect plasmonic photocatalysis, where excitation of SPR is used to transfer photon energy or hot electrons to the nearby semiconductors, molecular photocatalysts, and other metals to drive chemical reactions remotely. Therefore, the plasmonic metal NPs can work independently (in direct plasmonic photocatalysis) and also be used as sensitizer coupled with wide band gap semiconductor photocatalysts (in indirect plasmonic photocatalysis). In plasmonic photocatalysis, all the driving forces of photo-assisted catalysis are derived from the decay (or damping) of SPR through radiative and non-radiative processes. The SPR effect of plasmonic metal NPs is influenced by size, shape, type of element, surrounding mediums (gas, liquid, or semiconductor support), spatial distribution of both nanometals and semiconductor, etc.⁴⁵ Here a summary on the mechanisms of SPR-mediated catalysis will be provided.

A nanometal with SPR effect should have a size roughly between several nanometers and several tens of nanometers when an intense SPR effect can be induced by light. The absorbed resonant photons in the SPR absorption band will cause the intense, spatially non-homogeneous oscillating electric fields in the neighborhood of the

Chapter 1

plasmonic metal NPs. The energy of the intense local electric field is converted from the resonant photon flux (incident electric field). The intensity of incident electric field could be magnified up to $\sim 10^3$ times for an isolated nanometal to $\sim 10^6$ times for two particles separated by ~ 1 nm.⁴⁶⁻⁴⁸ The intensity of the oscillating electric fields will decrease exponentially with distance from the surface within ~ 20 - 30 nm and linearly further away.⁴³ As the generation rate of e^-/h^+ pairs in semiconductor is proportional to the local intensity of the electric field, the enhanced local field will in turn increase the generation rate of e^-/h^+ pairs in the adjacent semiconductors.⁴⁹ This is the so-called near-field or local electric field enhancement mechanism (mechanism 1). The fast recombination of electrons and holes in semiconductor is intrinsically attributed to the short diffusion length of minority charge-carriers (most of semiconductor photocatalysts are n-type and the minority carriers are holes). Because the light absorption depth is generally much larger than the diffusion length of minority charge-carriers in semiconductors, the minority carriers will be retained inside the bulk of semiconductors rather than migrate to the surface for redox reactions. The mechanism 1 is especially beneficial to the semiconductors with short carrier diffusion length. Since the interaction depth of local electric field enhancement mainly distributed near the surface layer (~ 10 nm) of semiconductor, such distance is comparable to the diffusion length of minority carriers. Plasmonic metal NPs can effectively couple the energy from far-field (incident electric field) into near-field and power the generation of e^-/h^+ pairs, this will create opportunity for the minority carriers to migrate onto the semiconductor surface and participate the redox reactions. It should be noted that the plasmonic metal NPs and the counterpart semiconductor are not necessary to form a close contact in mechanism 1 and the SPR energy transfer from plasmonic metal NPs to semiconductor can proceed when the both blocks are separated by insulating layers. This mechanism can be used to

Chapter 1

explain the enhanced photocurrent and photocatalytic reaction rate of TiO₂ or N doped TiO₂ by the PVP-coated plasmonic Ag NPs.⁵⁰ In addition to Ag/TiO₂ system, this mechanism also plays an important role in the Au plasmonic metal NPs-enhanced photocurrent of Fe₂O₃ photoelectrodes.^{49, 51}

Fast electromagnetic decay will take place radiatively or non-radiatively on fs timescale following SPR excitation. The radiative decay of SPR prevailingly happens on the large plasmonic nanostructures (> 50 nm) by emission of photons (i.e., scattering of resonant photons).^{43, 52} As the size of plasmonic metal NPs increases, the SPR absorption will be weakened and the scattering effect of the plasmonic metal NPs to the incident photon will gradually dominate the decay of surface plasmon. Therefore, large plasmonic metal NPs embedded inside a semiconductor can be used to improve the photoabsorption of semiconductor by multiple scattering of the resonant photon to increase the average photon path length as well as the photons' utilization efficiency (Fig. 1.3a). This is the so-called scattering enhancement mechanism (mechanism 2). Non-radiative decay is a dominant process for plasmonic metal NPs with smaller size (2 nm < diameter < 50 nm) and will lead to the generation of hot electrons and holes (also called Landau damping)⁴⁴ through the intraband excitation (between the Fermi level and *sp* CB) or interband excitation (between *d* band and *sp* CB).^{52, 53} Generation of hot electrons is of great importance in driving plasmonic photocatalysis. In direct plasmonic photocatalysis, the energetic hot electrons will be donated to the lowest unoccupied molecular orbital (LUMO) of an available adsorbate (this process also called chemical interface damping, CID)^{44, 54} to realize activation and reduction process (Fig. 1.3b). As for indirect plasmonic photocatalysis, the energetic electrons will overcome the Schottky barrier and be injected into the CB of neighboring semiconductor (Fig. 1.3c). The ultrafast electron injection from Au plasmonic metal NPs to semiconductor has been

Chapter 1

evidenced by in-situ electron paramagnetic resonance and infrared-probe femtosecond transient absorption spectroscopy.^{53, 55} Charge separation by semiconductor can effectively increase the lifetime of hot electrons and the efficiency of the energy conversion. The so-called hot electron generation and injection mechanism (mechanism 3) has been widely reflected in the studies of SPR-enhanced photocatalysis⁵⁶⁻⁶⁰ and photoelectrochemistry⁶¹⁻⁶³. Finally, the remaining photoexcited electrons relax through electron-electron and electron-phonon collisions, leading to a heating effect (also called ohmic damping) in the local environment to enhance the mass transfer and reaction speed of photo-assisted catalysis (mechanism 4). The interaction between light (electric field) and plasmonic metal NPs through SPR will also create inhomogeneous distribution of the charges on plasmonic metal NPs to form a dipole (Fig. 1.4). The dipole will polarizes the nonpolar molecules for a better adsorption and activation (mechanism 5).⁴⁵ Because the nonpolar molecules are generally difficult to activate in conventional thermocatalysis, the SPR may in particular favor the reactions involving the chemical transformation of nonpolar molecules (N₂, CO₂, CH₄, etc.). Above mentioned items 1-5 embrace the physical mechanisms involved in the photo-assisted catalysis over plasmonic metal NPs reported up to date. A realistic catalytic reaction system can possess one or more mechanisms.

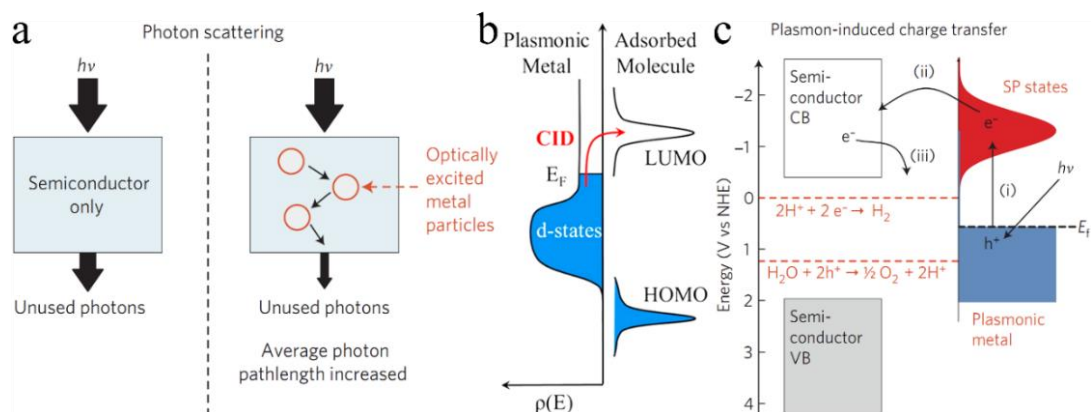


Fig. 1.3. (a) Schematic illustration of the scattering mechanism. The addition of optically excited plasmonic metal NPs increases the average path length of photons in the composite structure.⁴³ (b) Proposed mechanism of direct charge injection from metal to the LUMO of adsorbate molecule.⁴⁴ (c) Mechanism of SPR-induced charge transfer from plasmonic metal NPs to a nearby semiconductor.⁴³

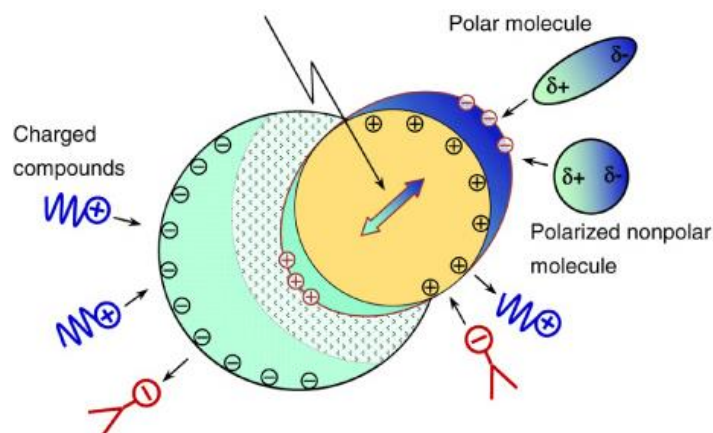


Fig. 1.4. Schematic representation of the enhanced adsorption in the plasmonic photocatalysis. The dipole nature of the local electric field of the surface plasmon attracts the polar molecules and polarizes nonpolar molecules.⁴⁵

Plasmonic photocatalysis is driven by the excited hot carriers from SPR decay. Both interband and intraband transitions will make contributions to plasmonic photocatalysis and they have not been often distinguished especially in the previous studies. However, a recent study has shown that the interband and intraband transitions may play different roles in driving an actual reaction. For the visible-light water oxidation over Au plasmonic metal NPs sensitized STO, the value of AQE decreases almost linearly with

Chapter 1

the increase of the wavelength, showing that the e^-/h^+ pairs for water oxidation mainly come from the interband transition of Au plasmonic metal NPs.⁶⁴ For the mostly studied Cu, Ag, and Au nanometals, the interband transitions correspond to $3d \rightarrow 4sp$ (2.1 eV), $4d \rightarrow 5sp$ (3.8 eV), and $5d \rightarrow 6sp$ (2.2 eV), respectively (the values in the brackets are the energy thresholds of the corresponding interband transitions).⁶⁵⁻⁶⁷ The characteristic color shown macroscopically by the bulk metals of Cu and Au is also a sign of the interband transitions in the visible light range. All of Cu, Ag, and Au nanometals show intraband transition in visible light range and, for ordinary near-spherical plasmonic metal NPs, their absorption peak maxima are positioned at 580 nm (~ 2.1 eV), 400 nm (~ 3.1 eV), and 530 nm (~ 2.3 eV), respectively.^{64, 68-71} Therefore, for Cu and Au plasmonic metal NPs, there will be an overlap between their interband and intraband excitations in the visible light range. Namely, the photoabsorption spectra of both kinds of plasmonic metal NPs in visible light range, in fact, show the superposition of interband and intraband transitions. The tip and edge of plasmonic nanostructures will cause stronger SPR effect. These special parts in nanostructure are also called the “hot spots”. The design and synthesis of plasmonic nanostructures with special size, shape and composition as well as the nanoscale assembly of nanometals and semiconductors were proposed as “hot spot engineering”.⁴³ The performance of plasmonic metal NPs for plasmonic photocatalysis can be improved accordingly by increasing the number of “hot spots” and reasonable assembly of plasmonic metal NPs and semiconductors.^{72, 73}

The lifetime of hot electrons in Au plasmonic metal NPs is very short ($\sim 10^{-3}$ ns)^{52, 74}. When the Au NPs are combined with a semiconductor, the hot electrons generated by Au plasmonic metal NPs will overcome the Schottky barrier and be separated by the neighboring semiconductors, resulting in the extended lifetime of the

Chapter 1

hot electrons ($\sim 10^0$ ns)^{52, 53, 75} to promote the photocatalytic reactions. Therefore, Au plasmonic metal NPs are often used in conjunction with a semiconductor (such as TiO₂). However, the lifetimes of hot electrons in Au plasmonic metal NPs or Au/TiO₂ system are still much shorter than that of the excited charge-carriers in semiconductors (e.g., TiO₂, $\tau > 10^3$ ns⁷⁶), implying that the recombination of e⁻/h⁺ in plasmonic photocatalysts is much more frequent than that in semiconductors. The hot electron injection is a reversible process. For Au/TiO₂ composite, the injected hot electron to TiO₂ will decay back to the Au plasmonic metal NPs just after ~ 1.5 ns to recombine with a hole if no donor can be timely consumed on Au plasmonic metal NPs.⁵² Therefore, to suppress the recombination of hot electrons and holes is crucial to improve the efficiency of plasmonic photocatalysts.

In a word, plasmonic nanometals can not only be used directly as new type of photocatalysts, it can be also used as plasmonic promoter by creating unique physical environment (local electric field and photothermal effect) to promote the adsorption, activation, mass transfer of molecules and improve the performance of host photocatalyst.

1.5 Research motivation and thesis organization

Overall, although the reaction environment shows significant influence on photocatalytic property, the attention paid on this subject remains very insufficient. In this dissertation, we focused on improving the photocatalytic performance by reaction environment modulation, including both chemical and physical environment control. The influences of these reaction environments on photocatalytic degradation, H₂ evolution, and CO₂ conversion were investigated. There are six chapters. A summary of the remaining five chapters is as follows:

Chapter 1

Chapter 2 Enhancement of photocatalytic activity for WO₃ by NaOH loading

WO₃ is an excellent photocatalyst for photocatalytic degradation under visible light. However, ORR is difficult to proceed over unmodified WO₃ due to its low CB position. Cocatalysts, such as noble metals, must be used to assist the separation of photogenerated electrons and suppress the deactivation of WO₃. Large scale application of WO₃ still needs low-cost and effective method to further improve the performance of WO₃ photocatalyst. In this chapter, we examined photocatalytic activity of NaOH-loaded WO₃ under visible-light irradiation. NaOH (solid base) treatment of WO₃ (an acidic oxide) is expected to realize two purposes. The first is change the surface structure and band position of photocatalyst and improve the ORR activity. The second is to render an alkaline reaction environment and change the reaction pathway (such as decomposition of H₂O₂) during the photocatalytic degradation over WO₃.

In addition to the photocatalytic degradation, the influence of alkaline environment on solar fuel production, i.e., photocatalytic H₂ evolution and CO₂ reduction into hydrocarbon compounds, was studied in chapter 3 and 4.

Chapter 3 Enhancement of H₂ production in alkaline environment over plasmonic Au/TiO₂ photocatalysts

Plasmonic Au NP is a new type of visible light active photocatalyst. However, photocatalytic H₂ production through plasmonic photocatalysis over Au NPs is still very inefficient to date. In the previous studies of electrocatalysis, Au is an excellent catalyst for the electrocatalytic oxidation of alcohols (methanol, ethanol, glycerol etc.) under alkaline environment.⁷⁷ In this chapter, plasmonic photocatalysis successfully employed electrocatalytic methanol oxidation mechanism to improve the plasmon-assisted H₂ production over Au/TiO₂ photocatalys in alkaline reaction environment.

Chapter 1

The fast consumption of the holes in plasmonic Au NPs by methanol in alkaline reaction system is expected to effectively suppress the recombination of hot electrons and holes, leading to enhanced H₂ production.

Chapter 4 Photocatalytic CO₂ reduction into CH₄ over alkali modified TiO₂ without loading noble metal cocatalysts

Due to the acidic nature of CO₂ molecules, NaOH was loaded on the surface TiO₂ to promote the chemisorption and activation of CO₂. In this chapter, NaOH was modified on TiO₂ to enhance the photocatalytic conversion of CO₂ into CH₄.

Chapter 5 Plasmon-mediated CO₂ activation and conversion with active hydrogen source

In view of the low efficiency of current water-based photocatalytic CO₂ conversion over semiconductor photocatalysts, new type of hydrogen source, H₂ and CH₄ were used to increase the CO₂ conversion efficiency in chapter 5. Firstly, H₂ was used for photo-induced CO₂ conversion over Ru catalyst. Ru nanocatalyst has two predominant features, namely i) highly efficient utilization of solar light and excellent photothermal performance, and ii) unique activation ability for the hydrogenation of CO₂ with H₂ (downhill reaction). Photothermal CO₂ conversion with H₂ over Ru is expected to realize a much higher efficiency than conventional photocatalytic method using water as hydrogen source. Compared with H₂, CH₄ is a more promising hydrogen source for CO₂ conversion (dry reforming of methane, DRM) due to an uphill reaction. Rh is the best catalyst in conventional thermal-driven catalytic DRM reaction. However, Rh did not show photoenhanced activity for DRM reaction. Au NPs were co-loaded with Rh NPs on SiO₂ and served as plasmonic promoter of the catalyst to enhance the DRM reaction rate by visible light.

Chapter 6 General Conclusion and Future Prospects

Chapter 1

This chapter gives an overall summary and conclusions of achievements of this dissertation. The prospects for further work were also presented.

References

1. R. Asahi, T. Morikawa, T. Ohwaki, K. Aoki and Y. Taga, *Science*, 2001, **293**, 269-271.
2. S. Ouyang and J. Ye, *J. Am. Chem. Soc.*, 2011, **133**, 7757-7763.
3. J. Tang, Z. Zou and J. Ye, *Angew. Chem. Int. Ed.*, 2004, **43**, 4463-4466.
4. A. Fujishima and K. Honda, *Nature*, 1972, **238**, 37-38.
5. Z. Zou, J. Ye, K. Sayama and H. Arakawa, *Nature*, 2001, **414**, 625-627.
6. Z. Yi, J. Ye, N. Kikugawa, T. Kako, S. Ouyang, H. Stuart-Williams, H. Yang, J. Cao, W. Luo, Z. Li, Y. Liu and R. L. Withers, *Nat. Mater.*, 2010, **9**, 559-564.
7. K. Maeda, K. Teramura, D. Lu, T. Takata, N. Saito, Y. Inoue and K. Domen, *Nature*, 2006, **440**, 295-295.
8. S. Yan, J. Wang, H. Gao, N. Wang, H. Yu, Z. Li, Y. Zhou and Z. Zou, *Adv. Funct. Mater.*, 2013, **23**, 1839-1845.
9. S. Navalón, A. Dhakshinamoorthy, M. Álvaro and H. Garcia, *ChemSusChem*, 2013, **6**, 562-577.
10. X. Lang, X. Chen and J. Zhao, *Chem. Soc. Rev.*, 2014, **43**, 473-486.
11. A. Inagaki and M. Akita, *Coord. Chem. Rev.*, 2010, **254**, 1220-1239.
12. H. Tong, S. Ouyang, Y. Bi, N. Umezawa, M. Oshikiri and J. Ye, *Adv. Mater.*, 2012, **24**, 229-251.
13. H. Xu, S. Ouyang, L. Liu, P. Reunchan, N. Umezawa and J. Ye, *J. Mater. Chem. A*, 2014, **2**, 12642-12661.

Chapter 1

14. A. Kudo and Y. Miseki, *Chem. Soc. Rev.*, 2009, **38**, 253-278.
15. D. Wang, T. Kako and J. Ye, *J. Phys. Chem. C*, 2009, **113**, 3785-3792.
16. X. Wang, K. Maeda, A. Thomas, K. Takanabe, G. Xin, J. M. Carlsson, K. Domen and M. Antonietti, *Nat. Mater.*, 2009, **8**, 76-80.
17. T. Kako, N. Kikugawa and J. Ye, *Catal. Today*, 2008, **131**, 197-202.
18. Y. Bi, S. Ouyang, N. Umezawa, J. Cao and J. Ye, *J. Am. Chem. Soc.*, 2011, **133**, 6490-6492.
19. J. S. Jang, H. G. Kim and J. S. Lee, *Catal. Today*, 2012, **185**, 270-277.
20. J. Ran, J. Zhang, J. Yu, M. Jaroniec and S. Z. Qiao, *Chem. Soc. Rev.*, 2014, **43**, 7787-7812.
21. S. Ouyang, H. Tong, N. Umezawa, J. Cao, P. Li, Y. Bi, Y. Zhang and J. Ye, *J. Am. Chem. Soc.*, 2012, **134**, 1974-1977.
22. T. Simon, N. Bouchonville, M. J. Berr, A. Vaneski, A. Adrović, D. Volbers, R. Wyrwich, M. Döblinger, A. S. Sussha, A. L. Rogach, F. Jäckel, J. K. Stolarczyk and J. Feldmann, *Nat. Mater.*, 2014, **13**, 1013-1018.
23. H. Sheng, H. Ji, W. Ma, C. Chen and J. Zhao, *Angew. Chem. Int. Ed.*, 2013, **52**, 9686-9690.
24. R. Abe, H. Takami, N. Murakami and B. Ohtani, *J. Am. Chem. Soc.*, 2008, **130**, 7780-7781.
25. H. Yu, H. Irie, Y. Shimodaira, Y. Hosogi, Y. Kuroda, M. Miyauchi and K. Hashimoto, *J. Phys. Chem. C*, 2010, **114**, 16481-16487.
26. M. Liu, X. Qiu, M. Miyauchi and K. Hashimoto, *Chem. Mater.*, 2011, **23**, 5282-5286.
27. Y. Nosaka, S. Takahashi, H. Sakamoto and A. Y. Nosaka, *J. Phys. Chem. C*, 2011, **115**, 21283-21290.

Chapter 1

28. J.-H. Kim, H. Sato, T. Kubo, S. Yonezawa and M. Takashima, *Chem. Lett.*, 2011, **40**, 230-232.
29. Q. Wang, C. Chen, D. Zhao, W. Ma and J. Zhao, *Langmuir*, 2008, **24**, 7338-7345.
30. Q. Wang, M. Zhang, C. Chen, W. Ma and J. Zhao, *Angew. Chem. Int. Ed.*, 2010, **49**, 7976-7979.
31. S. Trasatti, *J. Electroanal. Chem. Interfacial Electrochem.*, 1972, **39**, 163-184.
32. M. G. Walter, E. L. Warren, J. R. McKone, S. W. Boettcher, Q. Mi, E. A. Santori and N. S. Lewis, *Chem. Rev.*, 2010, **110**, 6446-6473.
33. R. Asai, H. Nemoto, Q. Jia, K. Saito, A. Iwase and A. Kudo, *Chem. Commun.*, 2014, **50**, 2543-2546.
34. J. Sato, N. Saito, Y. Yamada, K. Maeda, T. Takata, J. N. Kondo, M. Hara, H. Kobayashi, K. Domen and Y. Inoue, *J. Am. Chem. Soc.*, 2005, **127**, 4150-4151.
35. K. Sayama and H. Arakawa, *J. Chem. Soc., Faraday Trans.*, 1997, **93**, 1647-1654.
36. F. T. Wagner and G. A. Somorjai, *Nature*, 1980, **285**, 559-560.
37. V. P. Indrakanti, J. D. Kubicki and H. H. Schobert, *Energy & Environ. Sci.*, 2009, **2**, 745-758.
38. L. Zhang, D. Zhu, G. M. Nathanson and R. J. Hamers, *Angew. Chem. Int. Ed.*, 2014, **53**, 9746-9750.
39. Y. Hori, in *Modern Aspects of Electrochemistry*, eds. C. Vayenas, R. White and M. Gamboa-Aldeco, Springer New York, 2008, vol. 42, pp. 89-189.
40. J. N. Schrauben, R. Hayoun, C. N. Valdez, M. Braten, L. Fridley and J. M. Mayer, *Science*, 2012, **336**, 1298-1301.
41. S. Liu, Z. Zhao and Z. Wang, *Photochem. Photobiol. Sci.*, 2007, **6**, 695-700.
42. S. Xie, Y. Wang, Q. Zhang, W. Fan, W. Deng and Y. Wang, *Chem. Commun.*, 2013, **49**, 2451-2453.

Chapter 1

43. S. Linic, P. Christopher and D. B. Ingram, *Nat. Mater.*, 2011, **10**, 911-921.
44. M. J. Kale, T. Avanesian and P. Christopher, *ACS Catal.*, 2014, **4**, 116-128.
45. Z. Xuming, C. Yu Lim, L. Ru-Shi and T. Din Ping, *Rep. Prog. Phys.*, 2013, **76**, 046401.
46. Jiang, K. Bosnick, M. Maillard and L. Brus, *J. Phys. Chem. B*, 2003, **107**, 9964-9972.
47. L. Gunnarsson, T. Rindzevicius, J. Prikulis, B. Kasemo, M. Käll, S. Zou and G. C. Schatz, *J. Phys. Chem. B*, 2004, **109**, 1079-1087.
48. T. Chung, S.-Y. Lee, E. Y. Song, H. Chun and B. Lee., *Sensors*, 2011, **11**, 10907-10929.
49. J. Wang, S. L. Pan, M. Y. Chen and D. A. Dixon, *J. Phys. Chem. C*, 2013, **117**, 22060-22068.
50. D. B. Ingram and S. Linic, *J. Am. Chem. Soc.*, 2011, **133**, 5202-5205.
51. I. Thomann, B. A. Pinaud, Z. B. Chen, B. M. Clemens, T. F. Jaramillo and M. L. Brongersma, *Nano Lett.*, 2011, **11**, 3440-3446.
52. C. Clavero, *Nat. Photon*, 2014, **8**, 95-103.
53. A. Furube, L. Du, K. Hara, R. Katoh and M. Tachiya, *J Am. Chem. Soc.*, 2007, **129**, 14852-14853.
54. D. Menzel, K. Hyun Kim, D. Mulugeta and K. Watanabe, *J. Vac. Sci. Technol. A*, 2013, **31**, 050817.
55. J. B. Priebe, M. Karnahl, H. Junge, M. Beller, D. Hollmann and A. Bruckner, *Angew. Chem. Int. Ed.*, 2013, **52**, 11420-11424.
56. H. Yuzawa, T. Yoshida and H. Yoshida, *Appl. Catal. B-Environ.*, 2012, **115**, 294-302.
57. Z. Y. Zhang, A. R. Li, S. W. Cao, M. Bosman, S. Z. Li and C. Xue, *Nanoscale*,

Chapter 1

- 2014, **6**, 5217-5222.
58. M. S. Zhu, P. L. Chen and M. H. Liu, *ACS Nano*, 2011, **5**, 4529-4536.
59. G. N. Wang, X. F. Wang, J. F. Liu and X. M. Sun, *Chem-Eur. J.*, 2012, **18**, 5361-5366.
60. L. Liu, P. Li, T. Wang, H. Hu, H. Jiang, H. Liu and J. Ye, *Chem. Commun.*, 2015, **51**, 2173-2176.
61. Y. Nishijima, K. Ueno, Y. Kotake, K. Murakoshi, H. Inoue and H. Misawa, *J. Phys. Chem. Lett.*, 2012, **3**, 1248-1252.
62. X. Shi, K. Ueno, N. Takabayashi and H. Misawa, *J. Phys. Chem. C*, 2013, **117**, 2494-2499.
63. J. Lee, S. Mubeen, X. L. Ji, G. D. Stucky and M. Moskovits, *Nano Lett.*, 2012, **12**, 5014-5019.
64. L. Liu, P. Li, B. Adisak, S. Ouyang, N. Umezawa, J. Ye, R. Kodiyath, T. Tanabe, G. V. Ramesh, S. Ueda and H. Abe, *J. Mater. Chem. A*, 2014, **2**, 9875-9882.
65. H. Wang, F. Tam, N. K. Grady and N. J. Halas, *J. Phys. Chem. B*, 2005, **109**, 18218-18222.
66. A. Pinchuk, U. Kreibig and A. Hilger, *Surf. Sci.*, 2004, **557**, 269-280.
67. R. H. Doremus, *J. Chem. Phys.*, 1964, **40**, 2389-2396.
68. A. Marimuthu, J. W. Zhang and S. Linic, *Science*, 2013, **339**, 1590-1593.
69. P. Christopher, H. Xin and S. Linic, *Nat. Chem.*, 2011, **3**, 467-472.
70. C. Wang and D. Astruc, *Chem. Soc. Rev.*, 2014, **43**, 7188-7216.
71. A. O. Govorov, H. Zhang, H. V. Demir and Y. K. Gun'ko, *Nano Today*, 2014, **9**, 85-101.
72. L. Liu, T. D. Dao, R. Kodiyath, Q. Kang, H. Abe, T. Nagao and J. Ye, *Adv. Funct. Mater.*, 2014, **24**, 7754-7762.

Chapter 1

73. S. Sun, H. Liu, L. Wu, C. E. Png and P. Bai, *ACS Catal.*, 2014, **4**, 4269-4276.
74. H. Inouye, K. Tanaka, I. Tanahashi and K. Hirao, *Phys. Rev. B*, 1998, **57**, 11334-11340.
75. L. Du, A. Furube, K. Hara, R. Katoh and M. Tachiya, *J. Photochem. Photobiol. C: Photochem. Rev.*, 2013, **15**, 21-30.
76. C. Colbeau-Justin, M. Kunst and D. Huguenin, *J. Mater. Sci.*, 2003, **38**, 2429-2437.
77. Y. Kwon, S. C. S. Lai, P. Rodriguez and M. T. M. Koper, *J. Am. Chem. Soc.*, 2011, **133**, 6914-6917.

Chapter 2 Enhancement of photocatalytic activity for WO₃ by NaOH loading

2.1 Introduction

Photocatalysis under visible light irradiation is regarded as a promising technology for the removal of indoor harmful organics because indoor illumination contains large amounts of visible light. At present, visible light active photocatalysts with higher activity is limited. WO₃ is a simple binary-oxide semiconductor with high activity for photocatalytic O₂ evolution from an aqueous AgNO₃ solution under visible-light.^{1, 2} However, its photocatalytic activity for gaseous organic contaminant decomposition is limited due to the low conduction band position.³ Although the Co-catalyst loading (such as Pt or Pd) is an effective method for higher activity,^{4,5} the high cost of these precious metals limits the use of WO₃ photocatalyst in large scale. In addition, these precious metals may deactivate easily by poisoning effect of sulphur-containing gases such as H₂S and CH₃SH in human living environments.⁶

The addition of alkali hydroxide enhances the photocatalytic water-splitting property over Pt loaded TiO₂- and SrTiO₃-related materials.⁷⁻¹⁰ It is reported that the enhancement is attributed to the suppression of reverse reactions ($2\text{H}_2 + \text{O}_2 = 2\text{H}_2\text{O}$) on the Pt surface by alkali addition.^{7,11} However, this enhancement mechanism is not applicable for the case of

Chapter 2

photocatalytic organic decomposition because the reaction system for water splitting differs greatly from that of organic decomposition. Furthermore, photocatalytic decomposition of gaseous organics in alkali condition has been scarcely studied.

Wada et al. described that WO_3 , an acidic oxide, dissolves easily in the solution with high NaOH concentration. This dissolution brings the challenge for the application of WO_3 in alkaline reaction conditions.¹² In this chapter, we examined the photocatalytic activity of NaOH-loaded WO_3 under visible-light irradiation. Results demonstrated that the NaOH (solid base)-loaded WO_3 showed marked photocatalytic activity and high durability for gaseous organics decomposition.

2.2 Experimental methods

2.2.1 Photocatalysts preparation

Powder of NaOH-loaded WO_3 was prepared by the following method: 10 mL of an aqueous NaOH (Wako Pure Chemical Industries Ltd., Japan) solution (NaOH concentration: 20 g/L) and 4 g of monoclinic WO_3 (Wako) were mixed on a mortar for over 30 min, and the mixed powder was dried in an oven at 343 K for 4-5 h. Finally, we obtained the sample, of which the mixing ratio of NaOH to WO_3 was 5 wt% (NaOH: WO_3 = 5:100). Additionally, 25 wt%-NaOH-loaded WO_3 was prepared by using this method. As a reference sample, 0.075 wt% of KOH-loaded WO_3 powder was prepared using the method described in the earlier report. This powder was obtained by heating of the mixed KOH- WO_3 powder at 723 K for 2 h.¹³

2.2.2 Sample characterization

The prepared samples were characterized with an X-ray diffraction meter (XRD, X'pert Pro; PANalytical Co., Netherlands) with Cu K α radiation. Using the Kubelka-Munk relationship, optical absorption spectra of the prepared samples were converted from their respective reflectance spectra, which were measured using a UV-Vis spectrophotometer (UV-2500PC; Shimadzu Corp. Japan). Results of valence-band X-ray photoemission spectroscopic data (VB-XPS) were obtained by measuring the samples using an X-ray photoelectron spectrometer (AXIS-HS; Shimadzu-Kratos Analytical Com., Japan) with an X-ray source of monochromatic Al. Binding energy was calibrated using C 1s peak with binding energy of 284.5 eV.

2.2.3 Photocatalytic degradation in gas phase

Photocatalytic activity at room temperature was evaluated from 2-propanol (IPA) into CO₂ via acetone. Details of the evaluation method are the following: the powder sample with weight of 0.4 g spread evenly on the dish with the area of about 8 cm². The dish was set on the glass reactor with a volume of 500 cm³. The inside atmosphere of the reactor was replaced with pure air. Furthermore, IPA gas was injected into the reactor. Then, the concentration of the IPA in the reactor was estimated as 700-800 ppm. Subsequently, the reactor was kept in the dark until the IPA gas reached the adsorption-desorption equilibrium state. Then, the reactor was irradiated with visible light (400 nm < λ < 530 nm), which was emitted from a 300 W Xe lamp equipped with a water filter and glass filters of three kinds [UV-cutoff filter (Y-44), blue filter (B390), and IR cutoff filter (HA-30), Hoya. Corp., Japan]. The light intensity was about 1 mW cm⁻², which was evaluated using

a spectroradiometer (UV-40, Ushio Inc., Japan). The IPA, acetone, and CO₂ gases were measured using a gas chromatograph (GC-14B; Shimadzu) with flame-ionized detectors (FID) and a methanizer. The specific surface area was evaluated with a surface area analyzer (Gemini-2460; Micromeritics Instrument Corp., USA) using Brunauer-Emmett-Teller (BET) method at 77 K. Furthermore, the areas were 5.8, 7.0, 8.6, and 4.5 m²/g, respectively, for pure WO₃, 5wt%-NaOH-WO₃, 25 wt%-NaOH-WO₃, and 0.075 wt%-KOH-WO₃.

2.3 Results and discussion

2.3.1 Crystal structure

Fig. 2.1 shows the XRD patterns of pure WO₃ and 5 wt%-NaOH-loaded WO₃. From the XRD results, the 5 wt%-NaOH-loaded WO₃ mainly consists of monoclinic WO₃ (PDF No. 43-1035). A small amount of crystallized Na₂WO₄·2H₂O with orthorhombic structure (PDF No. 13-0431) also exists in the sample and should be formed from the reaction of NaOH with the surface layer of WO₃.¹³

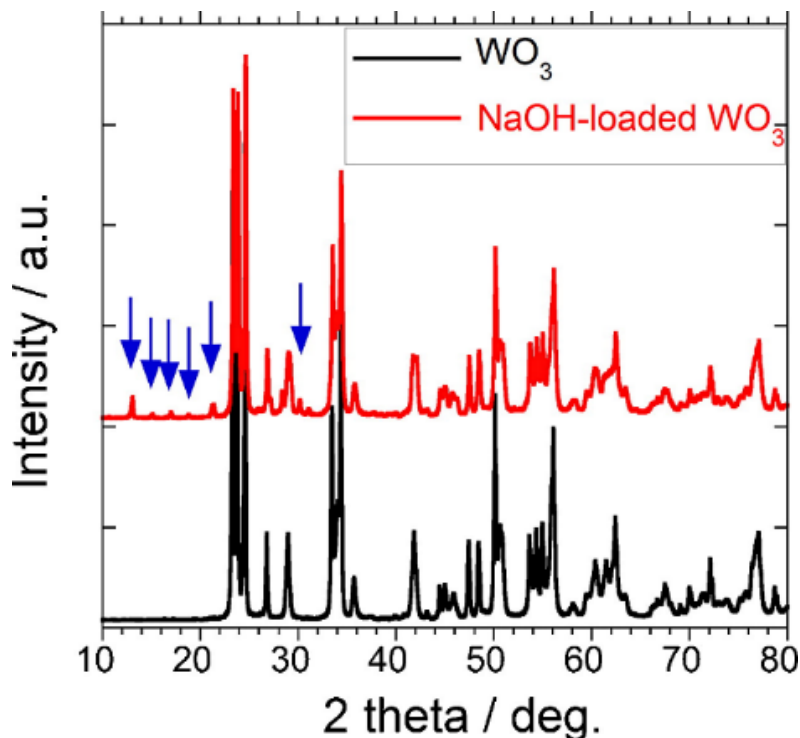


Fig. 2.1. XRD patterns of pure WO_3 and 5 wt% of NaOH-loaded WO_3 . Arrows indicate the XRD pattern of $\text{Na}_2\text{WO}_4 \cdot 2\text{H}_2\text{O}$.

2.3.2 Optical absorption property

As described above, the new phase was formed on the sample (NaOH-loaded WO_3) and this formation might affect the absorption property. Therefore, optical absorption spectra were measured using a UV-vis spectrophotometer. The optical absorption spectra of WO_3 and the 5 wt%-NaOH-loaded WO_3 are shown in Fig. 2.2. Both samples can absorb visible light well. Furthermore, the absorption spectrum of the NaOH-loaded WO_3 slightly blue-shifted compared with that of WO_3 . This blue shift is possibly attributed to the change of surface structure that is induced by NaOH treatment.

Next, the absorption properties were evaluated qualitatively to elucidate their differences in the properties. First, the band gaps were calculated from the onset absorption edges. The band gaps of pure WO_3 and the NaOH-loaded WO_3 were estimated,

respectively, as 2.6 and 2.7 eV. As a reference, the absorption spectrum of $\text{Na}_2\text{WO}_4 \cdot 2\text{H}_2\text{O}$ was also measured and the band gap was about 4.8 eV. Its band gap is over 2 eV larger than that of the NaOH-WO_3 , and will not show the photocatalytic activity under visible light.

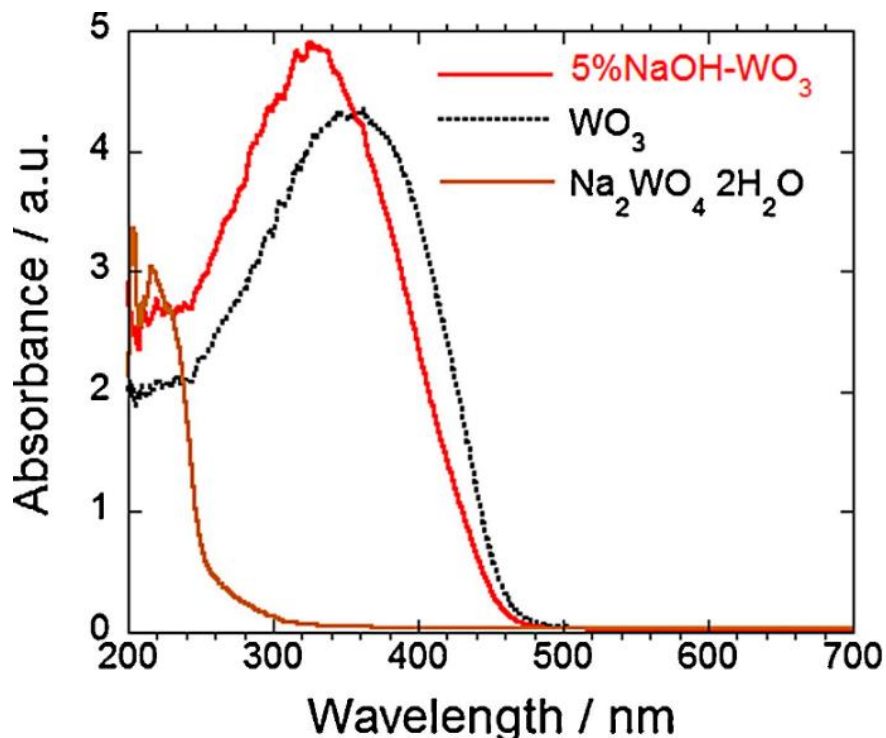


Fig. 2.2. Optical absorption spectra of WO_3 , 5 wt% of NaOH -loaded WO_3 and the reference sample $\text{Na}_2\text{WO}_4 \cdot 2\text{H}_2\text{O}$.

2.3.3 Energy band alignment

The band structure of a photocatalyst usually affects its photocatalytic activity. Therefore, information related to the band structure is important. Consequently, the potentials for top of the valence band (VB) for the samples were estimated. Then, the band structures were discussed using these estimated potentials and the band gaps. First, the potentials for top of the VB were estimated using VB-XPS technique. Fig. 2.3 presents the XPS spectra of the samples at around 0 eV in the binding energy. The result suggests that

Chapter 2

the potential for the top of VB for the NaOH-loaded WO_3 was 0.5 eV smaller than that for WO_3 . Furthermore, the potential for top of VB for WO_3 can be estimated as +3.0 V (vs SHE) because the band gap of WO_3 was 2.6 eV and its potential for bottom of CB was reported as +0.4 V (vs. SHE).¹⁴ Therefore, the potentials for the top of VB and bottom of CB for the NaOH-loaded WO_3 were estimated as -0.2 and +2.5 V (vs. SHE), respectively. Based on these results, the energy band alignment can be depicted in Fig. 2.4.

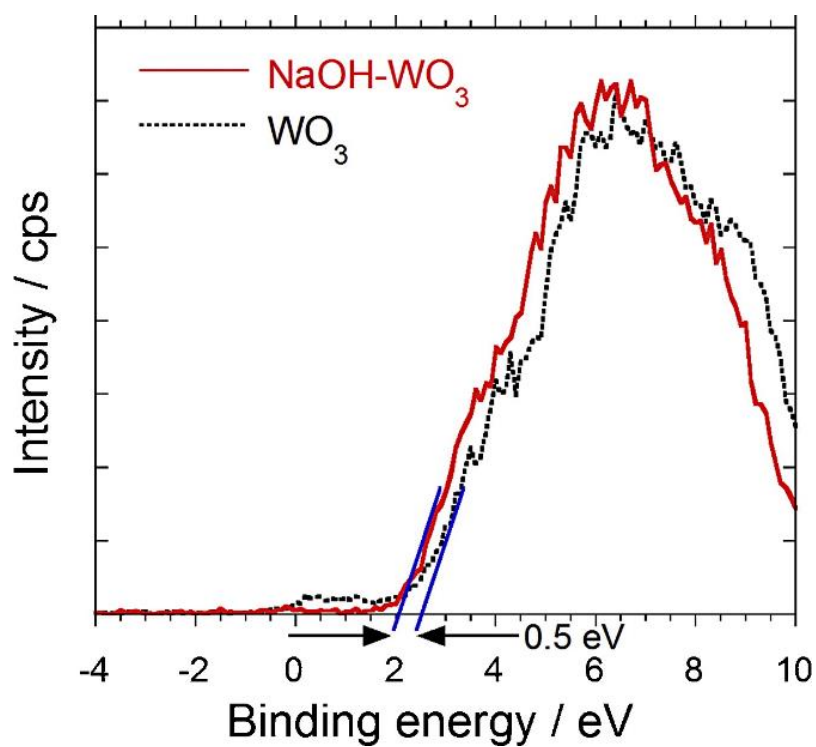


Fig. 2.3. VB-XPS spectra of WO_3 and 5 wt% of NaOH-loaded WO_3 .

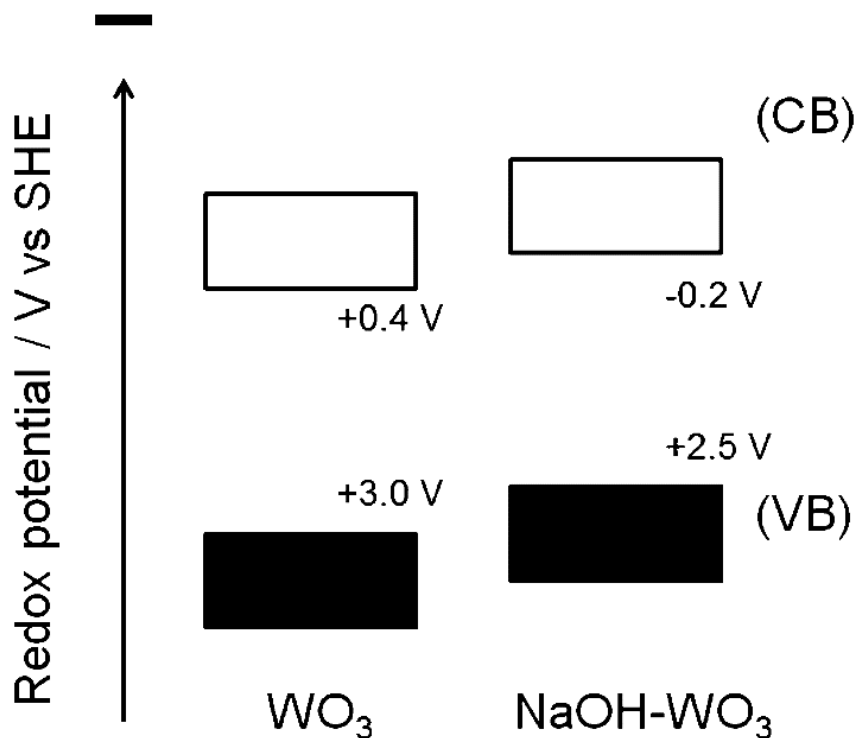


Fig. 2.4. Schematic illustration of the proposed band structure of WO_3 and 5 wt% of NaOH-loaded WO_3 .

2.3.4 Photocatalytic activity and reaction mechanism

Photocatalytic activity was evaluated from IPA decomposition into CO_2 via acetone because IPA is a frequently used VOC in industry. First, we evaluated IPA decomposition into acetone by photogenerated holes at the initial reaction stage. Fig. 2.5 shows a change in concentrations of acetone generation in IPA decomposition between 0 and 2 h of visible-light irradiation. Between 0 and 40 min, the acetone concentration over WO_3 is almost equal to that over the NaOH-loaded WO_3 . Subsequently, however, pure WO_3 was partially deactivated. The acetone concentration for WO_3 is half that for the NaOH-loaded WO_3 at 2 h of light irradiation. This result suggests that the NaOH loading does not work as enhancement of WO_3 photocatalytic activity itself. However, the loading functions as suppression of deactivation for WO_3 activity. By further visible light irradiation,

Chapter 2

intermediate acetone can be decomposed into the final product CO_2 by photogenerated holes. The time dependence of changes of acetone and CO_2 concentrations in Fig. 2.6 shows more marked difference in the activity between WO_3 and the NaOH-loaded WO_3 . For the NaOH-loaded WO_3 , acetone was mainly generated. The concentration of acetone generation increased linearly with irradiation time of 0-24 h. After about 24 h, the concentration of acetone in the gas phase decreased and CO_2 concentration increased drastically and linearly, indicating that intermediate acetone was decomposed into CO_2 . Furthermore, after about 200 h of visible-light irradiation, the injected IPA was decomposed almost completely into CO_2 by photogenerated holes for the NaOH-loaded WO_3 . For WO_3 , the concentrations of acetone and CO_2 generation increased slowly with irradiation time. The concentrations were extremely low. When the photocatalytic activity of the NaOH-loaded WO_3 is compared with that of pure WO_3 using CO_2 concentrations after 160 h, the activity of the NaOH (5 wt%)-loaded WO_3 was over 120 times higher than that of pure WO_3 . Larger surface area contributed little to higher photocatalytic activity of 5 wt%-NaOH- WO_3 because the surface area of the 5 wt%-NaOH- WO_3 ($7.0 \text{ m}^2/\text{g}$) was only 1.2 times higher than that of pure WO_3 ($5.8 \text{ m}^2/\text{g}$). The reason for this higher surface area is expected to be derived from the surface reaction of WO_3 with NaOH. The NaOH-loaded WO_3 shows much higher activity than WO_3 , which might be attributable to the ease of consumption for photogenerated electrons. Apparently, the reactions for consumption of photogenerated electrons on the NaOH-loaded WO_3 should be different from those for WO_3 . For WO_3 , photogenerated electrons can be reacted with O_2 through two-electron oxygen reduction (Eq. (3)), and H_2O_2 is formed.¹⁵ However, H_2O_2 is saturated quickly and the rate for H_2O_2 consumption is very slow (Fig. 2.6),¹⁵ indicating that H_2O_2 formation

Chapter 2

almost stops on the WO_3 after saturation. Because the other electron consumption cannot occur, little electron consumption occurs at H_2O_2 saturation. The accumulated photogenerated electrons will quickly deactivate WO_3 by either the possible production of low valence state of W (+5) or the recombination with photogenerated holes. This lead to a short time activity of WO_3 at just the initial stage of photoirradiation.

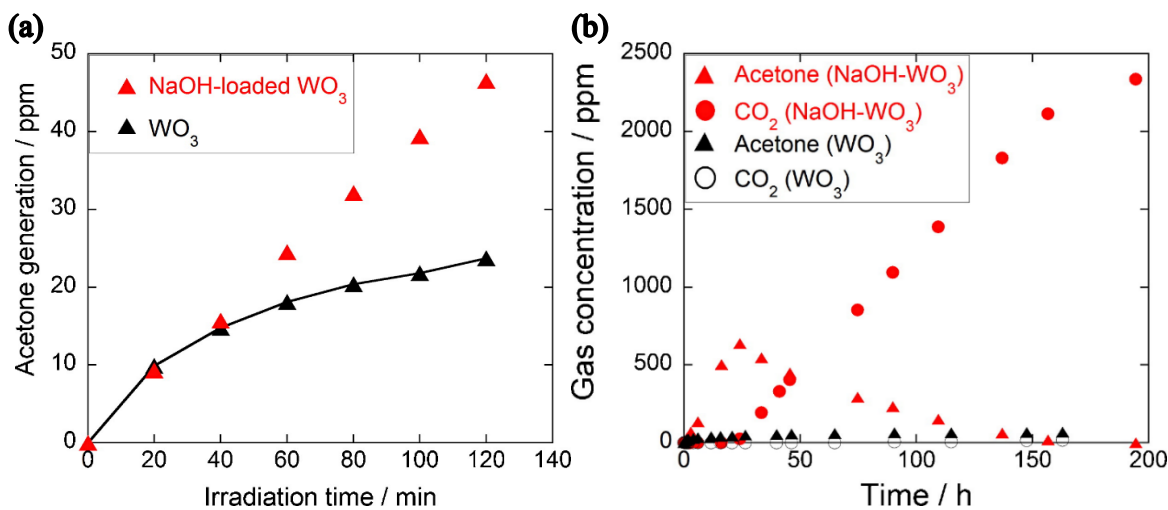


Fig. 2.5. (a) Photocatalytic IPA decomposition into acetone at the initial stage and (b) photocatalytic IPA decomposition into CO_2 via acetone between 0 and 200 h under visible-light irradiation over WO_3 and 5 wt% of NaOH-loaded WO_3 .

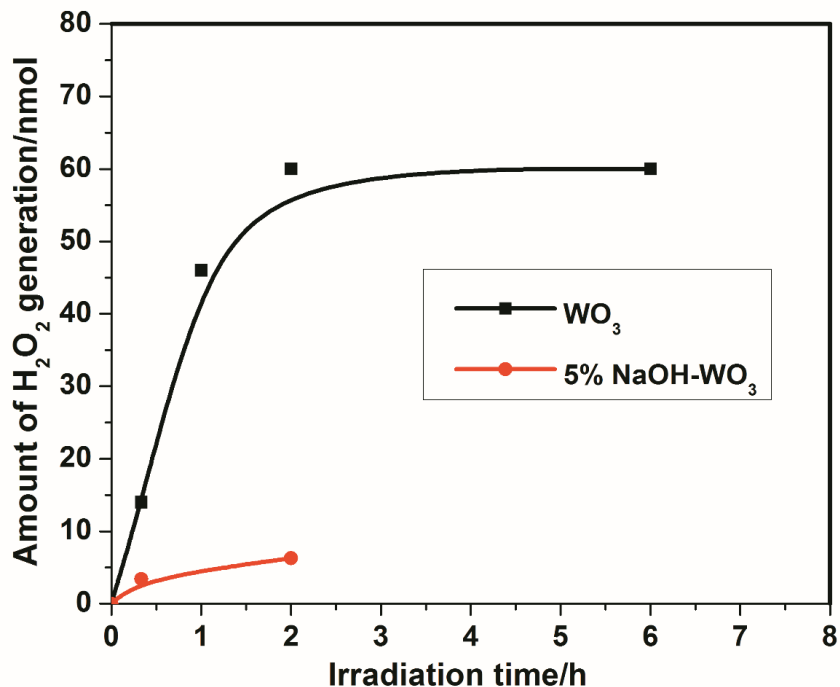
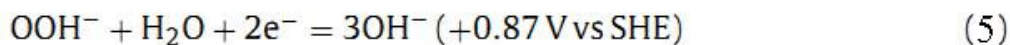
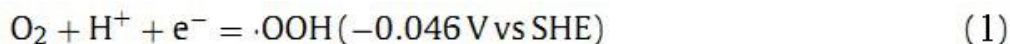


Fig. 2.6. Irradiation time dependence of amounts of H₂O₂ generation on WO₃ and 5wt%-NaOH-loaded WO₃.



For the NaOH-loaded WO₃, the electrons can be consumed by two-electron or even one-electron O₂ reductions. As shown in Fig. 2.4, the negative shift of bottom of CB for the NaOH-loaded WO₃ opens up possibility for one-electron O₂ reduction (Eqs. (1) and (2))⁵ and also increases the overpotential (the driving force of reaction) for two-electron O₂ reduction. Therefore, one-electron O₂ reduction may occur. The rate of this reduction is regarded as much higher than that of the two-electron oxygen reduction (Eq. (3)) reaction,¹⁶

Chapter 2

leading to higher activity of the NaOH-loaded WO_3 . Aside from one-electron O_2 reduction, two-electron O_2 reduction (Eqs. (3) and (5)) is expected to occur on the NaOH-loaded WO_3 . For the reduction described in Eq. (3), one must consider whether H_2O_2 is saturated on the surface of the NaOH-loaded WO_3 . This is because H_2O_2 saturation decreases the photocatalytic activity easily and heavily, just as WO_3 . However, under alkaline environment, H_2O_2 becomes more reactive. It is rapidly decomposed into reactive OOH^- (Eq. (4) and (7)), which further reacts with the photoexcited electrons (Eq. (5)). Therefore, for NaOH-loaded WO_3 , H_2O_2 can be consumed more easily via Eqs. (4)-(6).¹⁷ The rate of consumption of H_2O_2 for NaOH-loaded WO_3 is expected to be much higher than that for pure WO_3 , leading to higher activity of NaOH-loaded WO_3 . This expectation is supported by measurement of the H_2O_2 amount on the photocatalyst surface, i.e., the amount of H_2O_2 on the NaOH- WO_3 was much smaller than that on pure WO_3 .

As described above, the 5 wt%-NaOH-loaded WO_3 showed relatively high activity. Furthermore, a larger amount of NaOH-loaded sample, 25 wt%-NaOH-loaded WO_3 showed visible-light sensitivity and relatively high activity (Fig. 2.7). Its activity resembles the activity of 5 wt%-NaOH-loaded WO_3 . In addition, 25 wt%-NaOH-loaded WO_3 consisting of WO_3 , Na_2WO_4 , and NaOH shows stable photocatalytic performance for a long time and repeated test. Based on this result, we found that the photocatalyst maintains its relatively high activity for about 3 months. Furthermore, if 1 mol of IPA ($\text{C}_3\text{H}_8\text{O}$) is considered to be decomposed into 3 mol of CO_2 by 18 holes (Eq. (8)), the turnover number (TON) of this photocatalyst became about 1.1 after the eighth run of the photocatalytic repeated tests. Therefore, we conclude that the IPA decomposition over the NaOH-loaded WO_3 should be regarded as a genuine photocatalytic reaction.

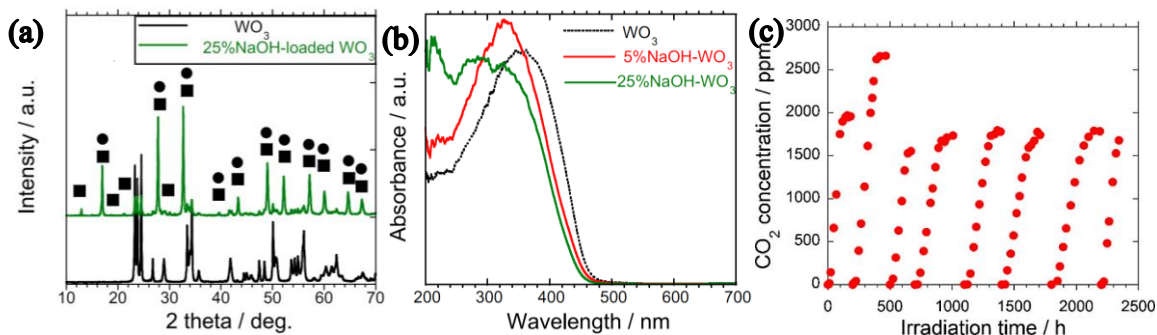
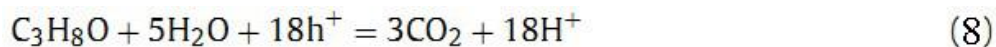


Fig. 2.7. (a) XRD patterns of 25 wt% of NaOH-loaded WO_3 . Closed square: orthorhombic $\text{Na}_2\text{WO}_4 \cdot 2\text{H}_2\text{O}$ (PDF: 13-0431); Closed circle: cubic Na_2WO_4 (PDF: 12-0772). The XRD data indicates that the 25 wt% of NaOH- WO_3 were composed of WO_3 , orthorhombic $\text{Na}_2\text{WO}_4 \cdot 2\text{H}_2\text{O}$, and cubic Na_2WO_4 . (b) UV-vis spectra, and (c) repeated tests for photocatalytic decomposition of IPA into CO_2 over 25 wt% of NaOH-loaded WO_3 under visible-light irradiation. 600-800 ppm of IPA gas in every turn except for the second run was injected into the reactor. In the second run, 860 ppm of IPA was injected.

The results of the activity and heating temperature reported herein completely differ from those of previously reported study by Aminian et al.¹³ In that study, 5 wt% of alkali loading at 723 K was too large. In addition, loading of too much alkali hydroxide cannot enhance the photocatalytic activity of WO_3 because of the complete phase transition and morphology changes from nanoparticles into nanorods. Furthermore, 0.075 wt%-KOH-loaded WO_3 prepared at 723 K reportedly showed the highest activity among the KOH-loaded WO_3 samples, with loading amounts of 0-5 wt% reported for their study. Therefore, we prepared 0.075 wt%-KOH-loaded WO_3 as a reference sample and compared its photocatalytic activity with the activity of our 5 wt% of NaOH-loaded WO_3 to elucidate the activity difference between this study and the previously reported studies. Fig. 2.8

Chapter 2

shows the time dependence of change of CO₂ generation in IPA decomposition under visible-light irradiation in the presence of some photocatalysts. Indeed, IPA can be decomposed by photocatalysis of 0.075 wt%-KOH-loaded WO₃. However, the activity for the 0.075 wt%-KOH-loaded WO₃ was over four times lower than that for the 5 wt%-NaOH-loaded WO₃ when the activity was evaluated from concentrations of CO₂ generation after about 160 h of light irradiation. Since the morphology changes were reported to lead to decrease in the activity as described above,¹³ the morphology of pure WO₃ and these two alkali-treated WO₃ was measured using SEM, which revealed no marked difference (Fig. 2.9). These three samples were composed entirely of nanoparticles, indicating that morphology changes that led to decreased activity did not occur by 5 wt%-NaOH-loading at 343 K. Namely, results show that 5 wt%-NaOH-loading at low temperature did not change the morphology. In addition, because a larger amount of alkali loading can promote decomposition of H₂O₂, the 5 wt%-NaOH-loaded WO₃ can show higher activity than the 0.075 wt%-KOH-loaded WO₃. Aside from these factors, the larger surface area contributed slightly to higher activity of the 5 wt%-NaOH-loaded WO₃. The activity for the 0.075 wt%-KOH-loaded WO₃ annealed at 723 K was reportedly much higher than that for 5 wt% of KOH-loaded WO₃ at 723 K. Therefore, it can be inferred that 5 wt%-NaOH-loaded WO₃ heated at 343 K shows much higher activity than 5 wt%-KOH-loaded WO₃ at 723 K with phase-transferred nanorods. From these results, we infer that the heating temperature is also an important factor for higher activity. Furthermore, we concluded that the loading amount of NaOH should be large (5-25 wt%). The loaded sample should be dried at low temperature, such as 343 K and room temperature, for the development of NaOH-loaded WO₃ with higher activity.

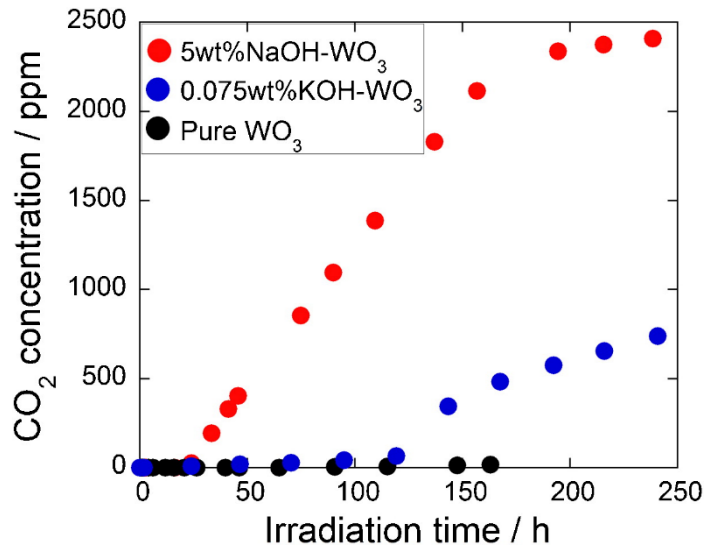


Fig. 2.8. Photocatalytic IPA decomposition into CO₂ under visible-light irradiation over WO₃, 5 wt% of NaOH-loaded WO₃, and 0.075 wt% of KOH-loaded WO₃.

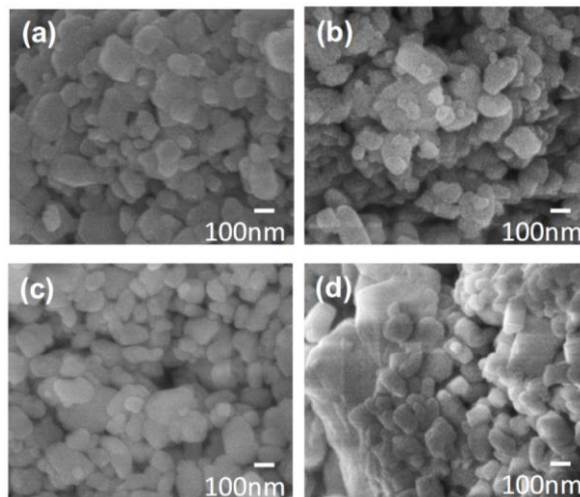


Fig. 2.9. SEM images of the prepared samples. (a) WO₃, (b) 5 wt%-NaOH-loaded WO₃, (c) 0.075 wt%-KOH-loaded WO₃, and (d) 25 wt%-NaOH-loaded WO₃.

2.4 Conclusions

We developed 5 wt%-NaOH-loaded WO_3 sample, which was prepared by drying the mixture of NaOH and WO_3 at 343 K. This sample showed marked photocatalytic activity for IPA decomposition into CO_2 under visible light irradiation. The activity of this sample was 120 times higher than that of pure WO_3 . This higher activity might derive from effective consumption of photogenerated electrons for the NaOH-loaded WO_3 , judging from the initial stage of IPA decomposition and stable photocatalytic performance of the NaOH-loaded WO_3 . IPA is mainly decomposed by photogenerated holes. However, if photogenerated electrons do not consume well, then recombination between holes and electrons occurs easily, leading to deactivation or low activity of the photocatalyst. Therefore, consumption of electrons is extremely important. For pure WO_3 , electrons are first consumed through two-electron O_2 reduction and H_2O_2 forms. H_2O_2 cannot be decomposed well and saturated on the surface, leading to decrease in the activity. However, for NaOH-loaded WO_3 , electrons can be consumed by two reactions including one-electron and two-electron O_2 reduction. For two-electron O_2 reduction, H_2O_2 may form, but this H_2O_2 is decomposed more easily because H_2O_2 becomes reactive in alkali conditions. For one-electron O_2 reduction, H_2O_2 does not form and accumulate on the surface, leading to maintenance of its activity. Additionally, results show that the activity of NaOH (solid base)-loaded WO_3 is affected strongly by heating temperature and loading amount of NaOH. Low heating temperature and a large loading amount engender higher photocatalytic activity. The 5 wt% of NaOH-loaded WO_3 heated at 343 K for this study showed over four times higher activity than the 0.075 wt%-KOH-loaded WO_3 described in the earlier report. In addition, 25 wt%-NaOH-loaded WO_3 showed relatively high

Chapter 2

photocatalytic activity and retains its photocatalytic activity for about 3 months. Based on these results, we conclude that solid-base loading is a promising method for the development of stable photocatalysts with high activity.

In addition to the photocatalytic degradation, an alkaline reaction environment is also favorable for photocatalytic H₂ production and CO₂ reduction as shown in chapter 3 and 4.

References

1. T. Kako, N. Kikugawa and J. Ye, *Catal. Today*, 2008, **131**, 197-202.
2. A. Kudo, K. Ueda, H. Kato and I. Mikami, *Catal. Lett.*, 1998, **53**, 229-230.
3. T. Arai, M. Yanagida, Y. Konishi, Y. Iwasaki, H. Sugihara and K. Sayama, *Catal. Commun.*, 2008, **9**, 1254-1258.
4. T. Arai, M. Horiguchi, M. Yanagida, T. Gunji, H. Sugihara and K. Sayama, *Chem. Commun.*, 2008, 5565-5567.
5. R. Abe, H. Takami, N. Murakami and B. Ohtani, *J. Am. Chem. Soc.*, 2008, **130**, 7780-7781.
6. T. Kako, H. Irie and K. Hashimoto, *J. Photochem. Photobiol. A: Chem.*, 2005, **171**, 131-135.
7. S. Sato and J. M. White, *J. Catal.*, 1981, **69**, 128-139.
8. S. Ouyang, H. Tong, N. Umezawa, J. Cao, P. Li, Y. Bi, Y. Zhang and J. Ye, *J. Am. Chem. Soc.*, 2012, **134**, 1974-1977.
9. K. Domen, S. Naito, T. Onishi and K. Tamaru, *Chem. Phys. Lett.*, 1982, **92**, 433-434.
10. F. T. Wagner and G. A. Somorjai, *Nature*, 1980, **285**, 559-560.
11. M. Kitano and M. Hara, *J. Mater. Chem.*, 2010, **20**, 627-641.

Chapter 2

12. M. Wada, N. Wang, Y. Konishi, Y. Miseki, T. Gunji and K. Sayama, *Chem. Lett.*, 2013, **42**, 395-397.
13. M. Khajeh Aminian and M. Hakimi, *Catal. Sci. Technol.*, 2014, **4**, 657-664.
14. M. Miyauchi, *Phys. Chem. Chem. Phys.*, 2008, **10**, 6258-6265.
15. J. Kim, C. W. Lee and W. Choi, *Environ. Sci. Technol.*, 2010, **44**, 6849-6854.
16. O. Tomita, R. Abe and B. Ohtani, *Chem. Lett.*, 2011, **40**, 1405-1407.
17. E. Yeager, *J Mol. Catal.*, 1986, **38**, 5-25.

Chapter 3 Enhancement of H₂ production in alkaline environment over plasmonic Au/TiO₂ photocatalysts

3.1 Introduction

Photocatalytic H₂ production is an important subject in solar fuel production. Of particular interest in the recent years is to use the alkaline environment to realize highly efficient H₂ production in aqueous system containing alcohol (as sacrificial reagent) over conventional oxide or sulfide semiconductors under visible light.^{1,2} This reaction involves the photooxidation of alcohols by the valence band holes and the photoreduction of protons by conduction band electrons. The enhanced photocatalytic H₂ production in alkaline environment is generally considered to benefit from the non-Nernstian dependence of the band edges shift of semiconductors on the pH of reaction system (i.e., slope $\neq -0.059$ V/pH).^{1,2}

Plasmonic photocatalysis is the cutting-edge research field of visible-light photocatalysis and has found extensive applications in H₂ production, environmental remediation, and organic transformation in the past few years.³⁻⁷ The redox ability of plasmonic photocatalysts originates from the surface plasmonic resonance (SPR).⁷ Au nanoparticles (NPs) are the most popular and widely used visible-light harvesting

Chapter 3

plasmonic photocatalysts up to now. The lifetime of the hot electrons in the SPR process of Au NPs is very short (in the timescale of 10^{-3} ns).^{8,9} Therefore, plasmonic Au NPs are often used in conjunction with a semiconductor (such as TiO_2). The ultrafast hot electrons injection from Au NPs to semiconductor can effectively extend the lifetime of the hot electrons (in the timescale of 10^0 ns) to favor the photocatalytic reactions.^{8, 10, 11} On the basis of the current understanding of electron transfer mechanism in plasmonic photocatalysis,^{11, 12} the redox process of H_2 production through plasmonic photocatalysis can be schematically shown in Fig. 3.1. Although plasmonic photocatalysis provides an alternative approach for visible-light H_2 production, the performance is still far less satisfactory when compared with the achievements of conventional semiconductor photocatalysis.^{13, 14} This is basically because the lifetimes of hot electrons through SPR excitation in Au NPs or Au/ TiO_2 system is still much shorter than that of the excited charge-carriers in semiconductors (e.g., TiO_2 , $> 10^3$ ns),¹⁵ implying that the recombination of e^-/h^+ in plasmonic Au NPs is much more frequent than semiconductors. Therefore, to suppress the recombination of hot electrons and holes in Au NPs is crucial to enhance the efficiency of plasmonic photocatalysts.

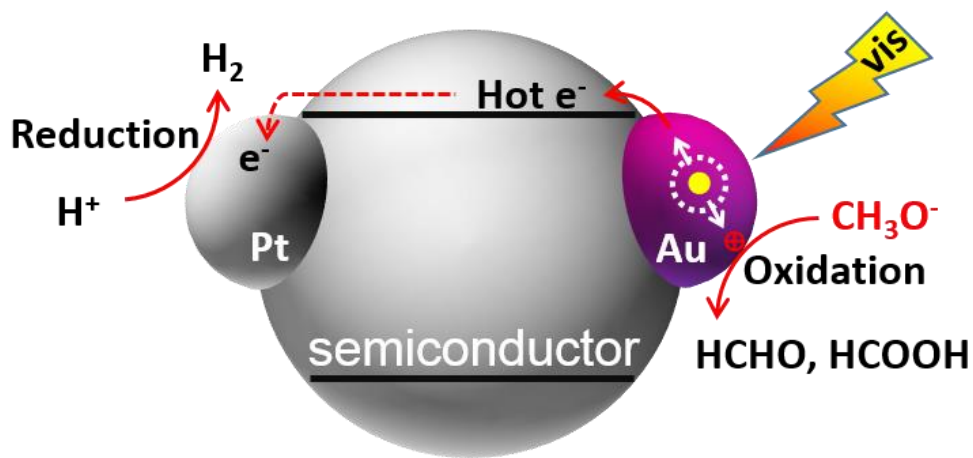


Fig. 3.1. Schematic process of H_2 production through plasmonic photocatalysis.

Chapter 3

Herein, the alkaline environment is employed to enhance the H₂ production over plasmonic Au/TiO₂ photocatalysts. This work was inspired by the growing awareness of the vital role of an alkaline environment for noble metal Au as well as Pt and Pd in showing their excellent electrocatalytic alcohols oxidation performance.¹⁶⁻²² Among these noble metal electrocatalysts, Au is a lucky one having photocatalytic performance because of its distinctive SPR effect in the visible light range. It is reasonable that the mechanism of electrocatalytic redox reaction over Au can provide inspiring knowledge to Au-based plasmonic photocatalysis. This is essentially determined by the identical physical nature in both processes, that is, the former process is driven by the externally applied bias and the latter is driven by the photovoltaic effect of excited Au SPR. In this work, plasmonic photocatalysis successfully drew the lessons from electrocatalytic methanol oxidation mechanism to improve the plasmon-assisted H₂ production over Au/TiO₂ photocatalysts. It is proposed that, in alkaline reaction system, the fast consumption of the holes in plasmonic Au NPs by methanol effectively suppress the recombination of hot electrons and holes, leading to enhanced H₂ production and the high apparent quantum efficiency (AQE).

3.2 Experimental methods

3.2.1 Photocatalyst preparation

Two types of classic Ti-based photocatalytic materials, TiO₂ (commercial P25) and SrTiO₃ (STO) were used as supports of Au NPs in this work. The large difference of their conduction band positions (nearly 1 eV)^{23, 24} can help us estimate to what extent the band edge positions of a semiconductor support will influence the performance of plasmonic

Chapter 3

photocatalyst (as discussed below). The plasmonic Au/P25 and Au/STO composite photocatalysts were prepared by conventional deposition-precipitation method.^{3-5, 25} The detailed preparation process of STO and the deposition-precipitation method refer to previous report.⁴

STO nanoparticles were prepared with a modified PC method.⁴ In brief, 2.88 ml $\text{Ti}(\text{OC}_4\text{H}_9)_4$ (Wako, min. 95.0%) was dissolved in 10 ml 2-methoxyethanol, denoted as solution A. Then, 2.18 g $\text{SrCl}_2 \cdot 6\text{H}_2\text{O}$ (Wako, min. 99.0%) was dissolved in 10 ml 2-methoxyethanol, denoted as solution B, and 30 g citric acid (CA, Wako, min. 98.0%) was dissolved in 30 ml 2-methoxyethanol with heating, denoted as solution C. Solutions A and B were mixed and stirred for 0.5 h to obtain a sol. This sol was transmitted to solution C and continually stirred for 10 min. After that, 5 ml dehydrated ethylene glycol (EG, Wako, min. 99.5%) was added. The mixture was then heated to 125 °C at an increasing rate of 1 °C min^{-1} and maintained for 20 h to evaporate the 2-methoxyethanol solvent. Subsequently, polymerization was carried out at 130 °C for another 20 h. The obtained brown resin was cooled to room temperature. Finally, the resin was heated in a stove at 300 °C for 3 h and calcined at 500 °C for 5 h at an increasing rate of 1 °C min^{-1} . Organic frames were completely removed by calcination at 500 °C, The resulting white powder was denoted as STO.

A series of Au/STO photocatalysts with different loadings (0.49-3.0%) were prepared with deposition-precipitation method by using urea ($\text{CO}(\text{NH}_2)_2$, Wako, min. 99.0%) as the precipitating base, which permits the gradual and homogeneous addition of hydroxide ions throughout the whole solution. In general, 1.0 g of STO was added to 100 ml of an aqueous solution of HAuCl_4 (6.2×10^{-4} M, Wako, min. 99.0%) and urea (0.19 M). The suspension

Chapter 3

maintained at 80 °C was vigorously stirred for 4 h (pH increases), then centrifuged, washed, dried, and calcined at 400 °C for 4 h. The reference sample Au/Pt/SiO₂ was prepared by impregnation of SiO₂ powder (Wako, catalogue No. 192-09071) in precursor solution containing HAuCl₄ and H₂PtCl₆. After dried at 70 °C, the samples were heat treated in 400 °C for 4 hours and reduced by H₂ reduction at 200 °C for 2 hours.

3.2.2 Sample characterization

UV-vis diffusion reflectance absorption spectra were measured by Shimadzu UV-2600 spectrophotometer. The loading amounts of Au on P25 TiO₂ or STO were analyzed by inductively coupled plasma optical emission spectrometry (ICP-OES, SPS3520UV-DD, SII nano technology Inc., Japan). Other basic characterizations and related results refer to previous report.⁴

3.2.3 Photocatalytic H₂ evolution

The photocatalytic H₂ evolution was carried out in a Pyrex glass reaction cell containing 50 ml CH₃OH and 220 ml H₂O. 25 mg of photocatalyst (loading 5 wt% Pt as cocatalyst by 2 hours' photodeposition under UV light from 300 W Xenon lamp) was used in each reaction. The pH of solution was adjusted by NaOH. The reaction cell was connected to a gas-closed system with a gas-circulated pump. A 300 W Xenon lamp equipped with L42 cutoff filter was used as the visible-light source ($\lambda > 400$ nm) of photocatalytic reaction. In the measurement of apparent quantum efficiency (AQE), a series of interference filters (418.5, 440.6, 500.3, 518.7, 548.1, 597.7, and 660.7 nm) were used to obtain monochromatic light. Water filter cooling was applied to avoid the crack of the interference filters. The intensity of incident monochromatic light was measured by a

spectroradiometer (Ushio, USR-40, Japan). The evolved H₂ was analyzed by an online gas chromatograph (GC-8A; Shimadzu Corp., Japan) equipped with a thermal conductivity detector. The AQE of each monochromatic light was calculated by the equation: AQE = (2 × the number of H₂ molecules/the number of incident photons) × 100%.

3.2.4. Photoelectrochemical measurements

Since the photooxidation reaction over plasmonic Au NPs is essentially an electrocatalytic process driven by the photovoltaic effect of excited Au SPR, plasmonic photooxidation of methanol will reasonably undergo an identical mechanism with the electrocatalysis towards methanol oxidation. The plasmonic Au/semiconductor/Pt system (Fig. 3.1) is equivalent to a nano photoelectrochemical system where the semiconductor supported Au and Pt NPs respectively serve as photoanode and photocathode. Photoelectrochemical measurement is used to simulate the reaction process of plasmonic photocatalysis.

Photoelectrochemical measurements were carried out using three-electrode mode on electrochemical station (ALS/CH model 650A). A platinum foil was used as counter electrode and Ag/AgCl electrode was used as the reference electrode. The electrolyte was same as photocatalytic reaction solutions (50 ml CH₃OH and 220 ml H₂O) and the pH was adjusted by NaOH. The working electrodes were fabricated by spin-coating method on ITO conductive glass with an area of 1 cm². 10 mg of 1.2 wt% Au/P25 was firstly suspended in 20 ml of ethanol (95%) by ultrasonic dispersion. The suspension was spin-coated on an ITO substrate with a rate of 800 rpm for 30 s. This process was repeated for 20 times. Before measurements the films were dried at room temperature and then calcined at 400 °C for 1 h (heating rate 5 °C min⁻¹). The P25/ITO film was prepared by the same

procedure. The photocurrent ($I-t$ curve) was measured at 1.1 V vs. RHE, and a 500 W Xenon lamp equipped with L42 cutoff filter was used as the visible light source.

3.3 Results and discussion

3.3.1 Sample characterization and photocatalytic activity

The loading amounts of Au for different samples were determined by ICP-OES method. Thus obtained Au NPs have relatively uniform particle size distribution (3-5 nm, see TEM images in Fig. 3.2 and related references).^{4,25} The UV-Vis spectra of Au/P25 and Au/STO showed that the SPR of Au NPs induced a wide photoabsorption in visible light range (Fig. 3.3) with the peak centered at ~550 nm. Pt was used as H₂-evolution cocatalyst prepared by photodeposition method (Fig. 3.4). The performance of H₂ production of 1.2 wt% Au/P25 loaded with Pt cocatalyst at various pH values was measured under visible light (Fig. 3.5). When the pH value is lower than 13, only a trace amount of H₂ evolution was found over Au/P25 photocatalysts. However, the H₂ production rate was remarkably enhanced when the pH value reached 14. In 5 M NaOH solution, the H₂ production rate achieved more than 200 $\mu\text{mol h}^{-1}$. Similar results were also obtained over Au/STO samples (Fig. 3.6). Activities of the samples with different Au loading amounts on P25 and STO were also measured at pH 14 (Fig. 3.7). The optimized Au loading amount was ~0.5 wt%, indicating that effective H₂ production can be realized in alkaline reaction environment by sensitizing TiO₂ or STO with tiny amount of plasmonic Au NPs. However, the reason for this optimized loading amount is not clear at the present stage. The photocatalysts also showed stable photocatalytic activity in alkaline environment. H₂ production almost kept

Chapter 3

a linear increase after overnight reaction over Au/P25 sample (Fig. 3.8). Control experiment using 0.9 wt% Au/3.6 wt% Pt/SiO₂ did not lead to H₂ evolution at pH 14, implying that a semiconductor support is important to realize the separation of hot electrons to drive the photocatalytic reactions. In addition, control experiment using 0.25 wt% Au/P25 without Pt cocatalyst in pH 7 and 14 just produced a trace amount of H₂ within 6 hours. Such H₂ production amount is lower than the detection limit of gas chromatograph unless the photocatalytic reaction can be further prolonged. As far as we know, the H₂ production activity measured in alkaline environment by this work is obviously higher than the recent reports on plasmon-assisted H₂ production. The AQE of H₂ production over 0.42 wt% Au/P25 photocatalysts was measured in the visible light range at pH 14 (Fig. 3.9). It was observed that the AQE increased linearly from 0 to 6% with the decrease of wavelength from 730 to 420 nm, indicating that the photocatalytic reaction in alkaline environment can be initiated by almost the whole range of visible light photons. AQE measurement over 0.49 wt% Au/STO showed a similar trend (Fig. 3.10). It can be easily speculated that the level of AQE will be further improved at higher pH values than 14.

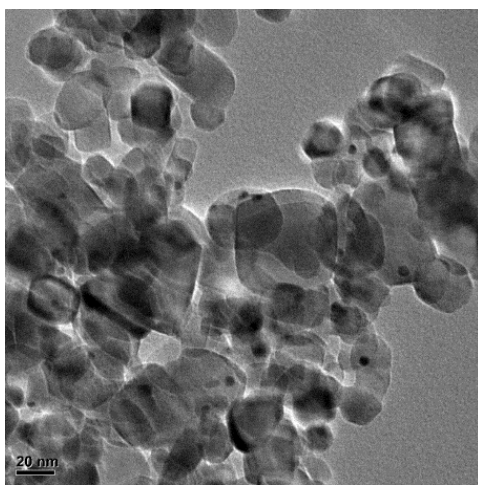


Fig. 3.2. TEM images of Au/P25 photocatalyst.

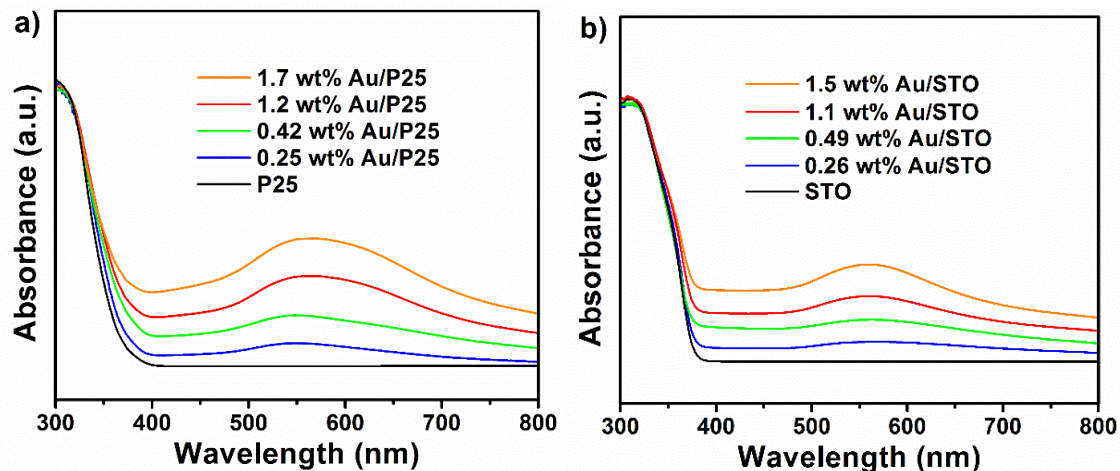


Fig. 3.3. UV-vis spectra of a) Au/P25 and b) Au/STO.

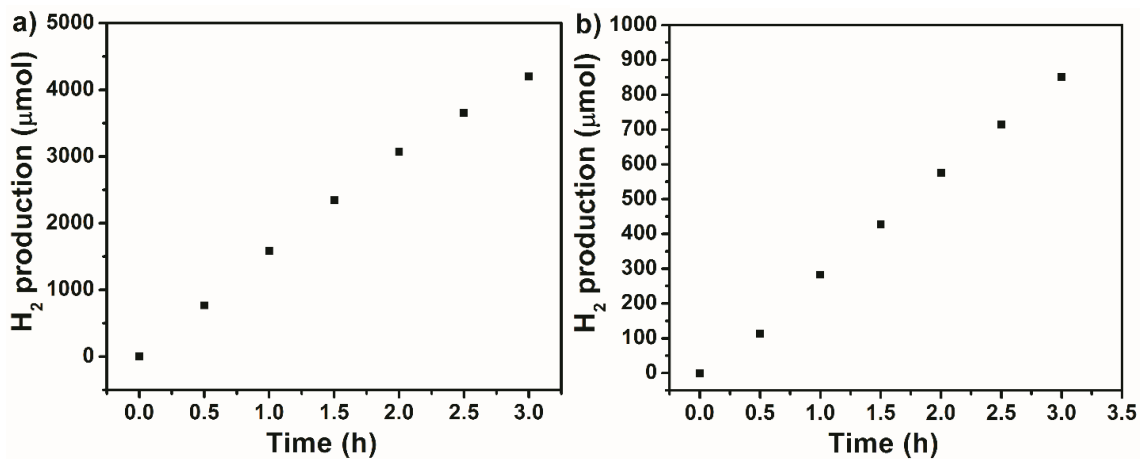


Fig. 3.4. H₂ production during the photodeposition of 5 wt% Pt on a) P25 and b) STO under UV light from 300 W Xenon lamp. The deposition of Pt finished within ~0.5 hour on P25 and ~1 hour on STO.

Chapter 3

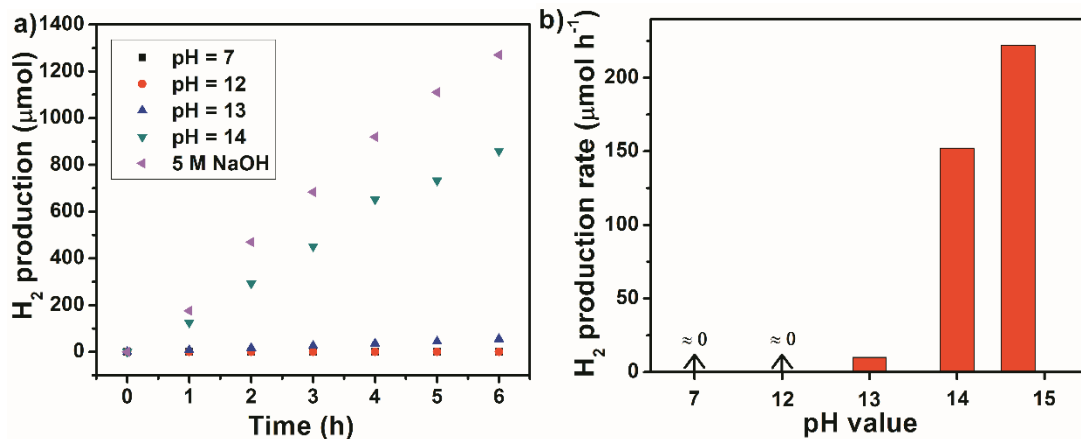


Fig. 3.5. (a) H₂ production over 1.2 wt% Au/P25 at varied pH values under visible light irradiation (300 W Xenon lamp with L42 cutoff filter, $\lambda > 400$ nm). (b) H₂ production rates in (a).

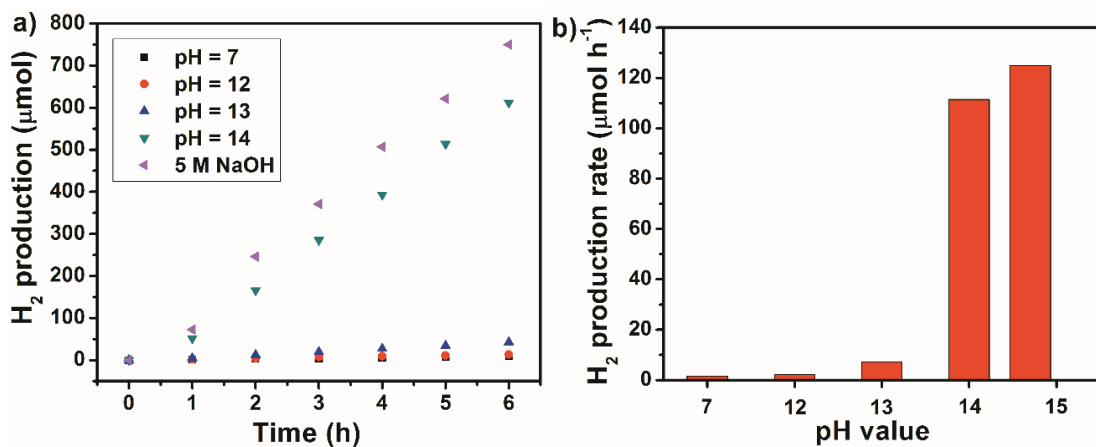


Fig. 3.6. (a) H₂ production over 1.1 wt% Au/STO at varied pH values under visible light irradiation (300 W Xenon lamp with L42 cutoff filter, $\lambda > 400$ nm). (b) H₂ production rates in (a). The photocatalytic H₂ production was carried out in a Pyrex glass reaction cell containing 50 ml CH₃OH and 220 ml H₂O. 25 mg of photocatalyst (loading 5 wt% Pt as cocatalyst by 2 hours' photodeposition under 300 W Xenon lamp) was used in each reaction. The pH of solution was adjusted by NaOH.

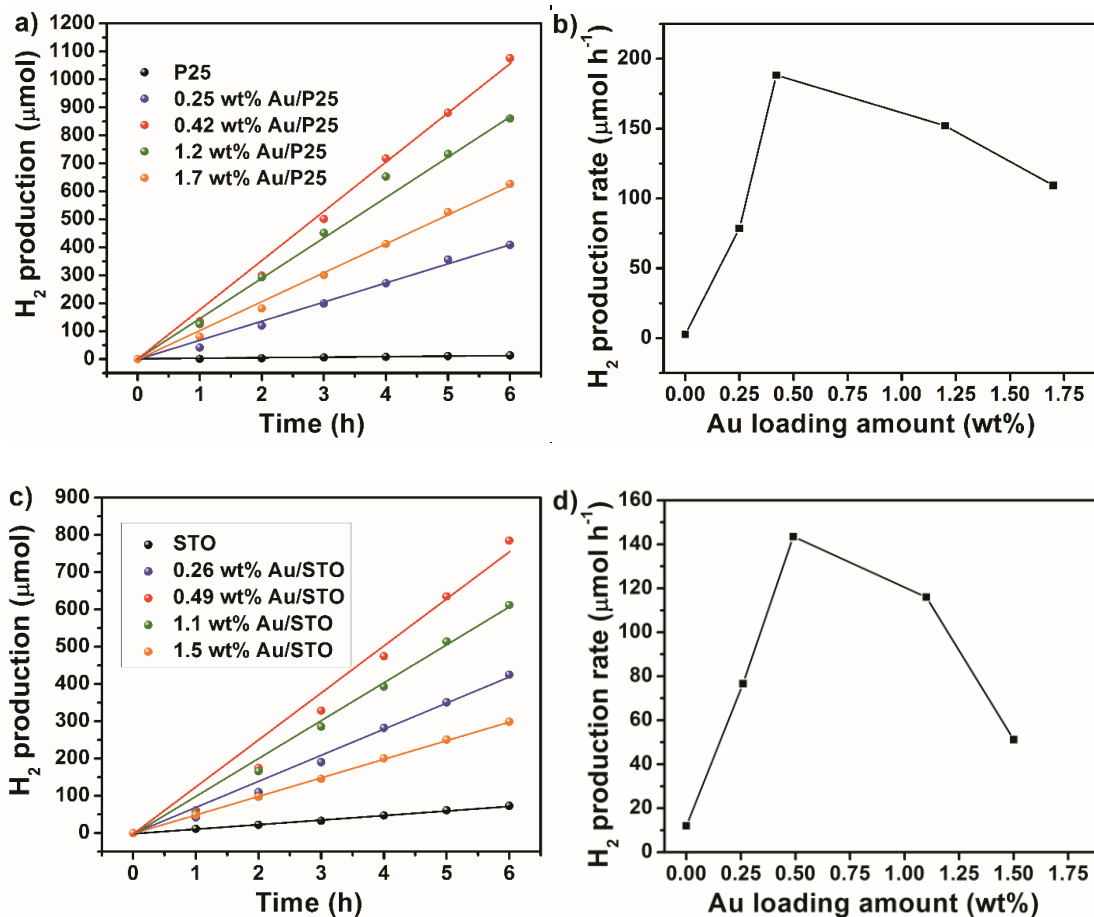


Fig. 3.7. H₂ evolution over (a) Au/P25 and (c) Au/STO with different Au loading amounts at pH 14 under visible light irradiation ($\lambda > 400$ nm). H₂ production rates of (b) Au/P25 and (d) Au/STO in (a) and (c).

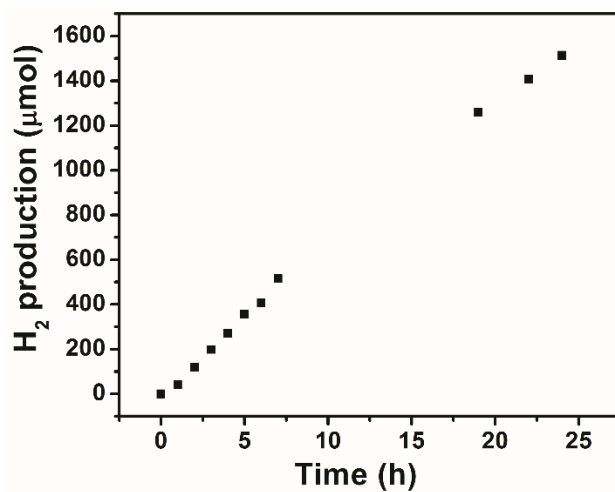


Fig. 3.8. Long-term H₂ evolution over 0.25 wt% Au/P25 at pH 14 under visible light irradiation ($\lambda > 400$ nm).

Chapter 3

The hot electrons in a plasmonic nanometal can be generated through both the intraband (between the Fermi level and *sp* conduction band) and interband transitions (between *d* band and *sp* conduction band) during the SPR decay.^{8, 11} The contributions of intraband and interband transitions to a typical UV-Vis spectrum of ordinary Au NPs without special nanostructures are schematically shown in Fig. 3.9b.²⁶⁻²⁸ It is noteworthy that the AQE profile is in a perfect agreement with photoabsorption through interband transition of Au NPs, which is similar to our previous report.⁴ This result can be possibly explained from two aspects. On one hand, the oxidation ability of Au originates from the ionization of Au NPs (transient generation of Au⁺) in SPR process.^{3, 8, 29} Quantitative investigation using nanosecond pulse-laser has evidenced that the ionization of Au NPs is mainly contributed by the interband excitation.²⁷ Therefore, the interband excitation can be directly correlated with the photooxidation ability of Au NPs to methanol. On the other hand, seeing from the energy band alignment, the *d* band is lying lower than Fermi level of gold.⁸ This means that the potential of the holes formed by interband transition should be more positive than that formed by intraband transitions and the former should have stronger photooxidation ability to methanol. These facts indicate that interband transition plays more dominative role in the photooxidation process than intraband transition, which will be finally reflected on the feature of AQE.

Chapter 3

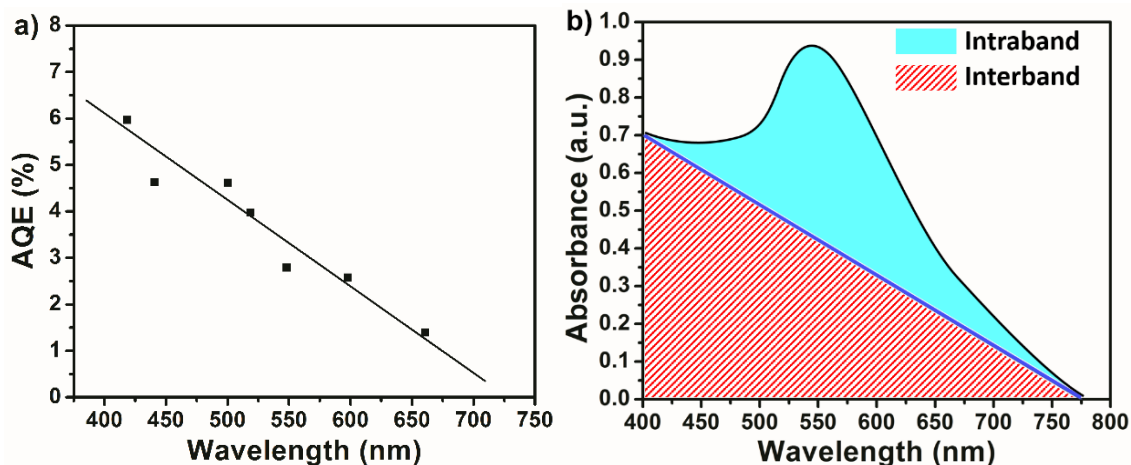


Fig. 3.9. (a) The apparent quantum efficiency of H₂ evolution over 0.42 wt% Au/P25 photocatalysts in the visible light range. Reaction was carried out under pH = 14. (b) The schematic absorption spectrum of Au NPs (black line). The spectrum consists of the absorptions from both intraband and interband excitation.

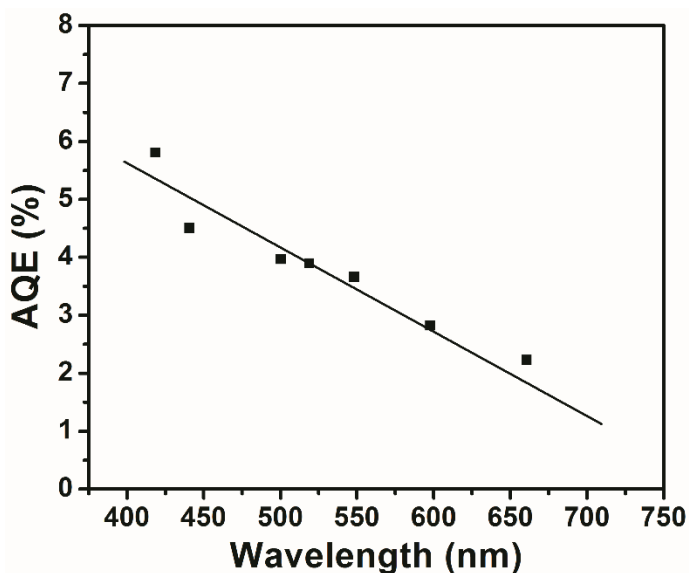


Fig. 3.10. The apparent quantum efficiency of H₂ evolution over 0.49 wt% Au/STO photocatalysts in the visible light range. Measurement was carried out at pH 14 using monochromatic light.

STO support has a much more negative conduction band level than P25 TiO₂ and will render higher reduction potential to the separated hot electrons from Au NPs for proton reduction. This indeed contributed subtle H₂ production to Au/STO in comparison with

Chapter 3

only trace amount of H₂ evolution over Au/P25 at low pH range (Fig. 3.5 and Fig. 3.6). However, this enhancement is almost negligible when compared with the enhanced H₂ production by increasing the pH value for each sample (Fig. 3.5 and Fig. 3.6). In fact, Au/P25 showed higher activities than Au/STO at high pH range. Therefore, the mechanism of the enhanced H₂ production over semiconductor photocatalysts (non-Nernstian shift of band edges)¹ is not completely applicable to explain how the alkaline environment enhanced the H₂ production over plasmonic Au/TiO₂ photocatalysts. We speculate that the alkaline environment may exert direct influence on the surface redox reaction. Because the proton reduction will be generally suppressed in concentrated alkaline environment, it is very likely that the alkaline environment enhanced the methanol photooxidation by the holes in the plasmonic Au NPs. Actually, the electrocatalytic oxidation of alcohols (methanol, ethanol, glycerol etc.) over Au can only readily occur under alkaline environment, whereas under acidic and neutral conditions the reaction becomes significantly sluggish.¹⁶⁻²⁰ Koper and co-workers proposed that the alkaline environment dominated the main process of alcohols oxidation over Au electrode which involved two deprotonation steps, including a “base-catalyzed” step to produce reactive alkoxide at high pH values and a further “gold catalyzed” step for alkoxide oxidation.¹⁶ The oxidation behavior of these alcohols generally varies in a highly nonlinear fashion with pH, showing a highly consistent trend with the variation of photocatalytic H₂ production rate with pH in this work.

3.3.2 Photoelectrochemical measurements

The (photo)electrochemical analysis is a powerful tool to simulate the microscopic electron transfer mechanism and provide the information related to the surface chemical

Chapter 3

reaction pathway in a photocatalytic reaction.^{1, 2, 30, 31} Photoelectrochemical measurements in this work further provided conclusive evidences for the above mentioned interpretations. The working electrodes were fabricated by spin-coating the well dispersed Au/P25 or pure P25 suspension on ITO substrates followed by a heat treatment at 400 °C. Under the dark condition, the Au NPs on the photoanode just served as electrocatalysts and there was a sudden increase of the dark current when the pH reached 14 (Fig. 3.11a). This result showed a consistent conclusion with the previous electrocatalytic studies, confirming that alkaline environment can effectively enhance the methanol oxidation over Au.¹⁶⁻²⁰ An obvious inflection point at pH 14 was also observed in the photoresponse of Au/P25 film (Fig. 3.11b), clearly showing that, under alkaline environment, enhanced photooxidation of methanol was achieved by the SPR excitation of Au NPs to realize the solar-to-chemical energy conversion. Pure TiO₂ is incapable of effectively driving the methanol oxidation electrocatalytically or photocatalytically under visible light, leading to negligible current responses in control experiments (Fig. 3.11). For Au/TiO₂ composite, the injected hot electron to TiO₂ will decay back to the Au NPs just after ~1.5 ns to recombine with a hole if no donor can be timely consumed on Au NPs.^{8, 10, 11} The fast photooxidation of methanol enhanced consumption of the holes in plasmonic Au NPs and suppressed the recombination of e⁻/h⁺ pairs, resulting in effective regeneration of hot electrons for photocatalytic H₂ production.

Conclusions

In summary, alkaline environment modulation remarkably boosts H₂ production over plasmonic Au/TiO₂ photocatalysts and achieves exceptional performance. This strategy could be universally applicable to the generation of hydrogen from aqueous system containing a variety of alcohols. The fast photooxidation process effectively accelerates the consumption of holes in Au NPs and improve the AQE of plasmonic photocatalysis. In view of the growing importance of solar-to-chemical energy conversion, this is in particular attractive for the solar fuel production from photoreforming of polyhydroxy biomass over Au-based plasmonic photocatalysts under visible light. This work also hints that electrocatalytic reactions over gold are transplantable for their applications in plasmonic photocatalysis.

References

1. S. Ouyang, H. Tong, N. Umezawa, J. Cao, P. Li, Y. Bi, Y. Zhang and J. Ye, *J. Am. Chem. Soc.*, 2012, **134**, 1974-1977.
2. T. Simon, N. Bouchonville, M. J. Berr, A. Vaneski, A. Adrović, D. Volbers, R. Wyrwich, M. Döblinger, A. S. Susha, A. L. Rogach, F. Jäckel, J. K. Stolarczyk and J. Feldmann, *Nat. Mater.*, 2014, **13**, 1013-1018.
3. A. Primo, A. Corma and H. Garcia, *Phys. Chem. Chem. Phys.*, 2011, **13**, 886-910.
4. L. Liu, P. Li, B. Adisak, S. Ouyang, N. Umezawa, J. Ye, R. Kodiyath, T. Tanabe, G. V. Ramesh, S. Ueda and H. Abe, *J. Mater. Chem. A*, 2014, **2**, 9875-9882.
5. C. Wang and D. Astruc, *Chem. Soc. Rev.*, 2014, **43**, 7188-7216.

Chapter 3

6. L. Liu, S. Ouyang and J. Ye, *Angew. Chem. Int. Ed.*, 2013, **52**, 6689-6693.
7. S. Linic, P. Christopher and D. B. Ingram, *Nat. Mater.*, 2011, **10**, 911-921.
8. C. Clavero, *Nat. Photon*, 2014, **8**, 95-103.
9. H. Inouye, K. Tanaka, I. Tanahashi and K. Hirao, *Phys. Rev. B*, 1998, **57**, 11334-11340.
10. L. Du, A. Furube, K. Hara, R. Katoh and M. Tachiya, *J. Photochem. Photobiol. C: Photochem. Rev.*, 2013, **15**, 21-30.
11. A. Furube, L. Du, K. Hara, R. Katoh and M. Tachiya, *J. Am. Chem. Soc.*, 2007, **129**, 14852-14853.
12. J. B. Priebe, M. Karnahl, H. Junge, M. Beller, D. Hollmann and A. Bruckner, *Angew. Chem. Int. Ed.*, 2013, **52**, 11420-11424.
13. J. Q. Yan, G. J. Wu, N. J. Guan and L. D. Li, *Chem. Commun.*, 2013, **49**, 11767-11769.
14. Z. Zheng, T. Tachikawa and T. Majima, *J. Am. Chem. Soc.*, 2014, **136**, 6870-6873.
15. C. Colbeau-Justin, M. Kunst and D. Huguenin, *J. Mater. Sci.*, 2003, **38**, 2429-2437.
16. Y. Kwon, S. C. S. Lai, P. Rodriguez and M. T. M. Koper, *J. Am. Chem. Soc.*, 2011, **133**, 6914-6917.
17. S. C. S. Lai, S. E. F. Kleijn, F. T. Z. Öztürk, V. C. van Rees Vellinga, J. Koning, P. Rodriguez and M. T. M. Koper, *Catal. Today*, 2010, **154**, 92-104.
18. Y. Kwon, K. J. P. Schouten and M. T. M. Koper, *ChemCatChem*, 2011, **3**, 1176-1185.
19. J. Hernández, J. Solla-Gullón, E. Herrero, A. Aldaz and J. M. Feliu, *Electrochim. Acta*, 2006, **52**, 1662-1669.
20. B. Beden, I. Çetin, A. Kahyaoglu, D. Takky and C. Lamy, *J. Catal.*, 1987, **104**, 37-46.
21. A. Santasalo-Aarnio, Y. Kwon, E. Ahlberg, K. Kontturi, T. Kallio and M. T. M. Koper, *Electrochem. Commun.*, 2011, **13**, 466-469.

Chapter 3

22. T. Sheng, W.-F. Lin, C. Hardacre and P. Hu, *J. Phys. Chem. C*, 2014, **118**, 5762-5772.
23. Y. Xu and M. A. A. Schoonen, *Am. Mineral.*, 2000, **85**, 543-556.
24. R. van de Krol, Y. Liang and J. Schoonman, *J. Mater. Chem.*, 2008, **18**, 2311-2320.
25. A. V. Puga, A. Forneli, H. García and A. Corma, *Adv. Funct. Mater.*, 2014, **24**, 241-248.
26. M. M. Alvarez, J. T. Khoury, T. G. Schaaff, M. N. Shafigullin, I. Vezmar and R. L. Whetten, *J. Phys. Chem. B*, 1997, **101**, 3706-3712.
27. K. Yamada, K. Miyajima and F. Mafuné, *J. Phys. Chem. C*, 2007, **111**, 11246-11251.
28. V. Subramanian, E. E. Wolf and P. V. Kamat, *J. Am. Chem. Soc.*, 2004, **126**, 4943-4950.
29. Y. Tian and T. Tatsuma, *J. Am. Chem. Soc.*, 2005, **127**, 7632-7637.
30. D. B. Ingram and S. Linic, *J. Am. Chem. Soc.*, 2011, **133**, 5202-5205.
31. T. K. Townsend, N. D. Browning and F. E. Osterloh, *Energy Environ. Sci.*, 2012, **5**, 9543-9550.

Chapter 4 Photocatalytic CO₂ reduction into CH₄ over alkali modified TiO₂ without loading noble metal cocatalysts

4.1 Introduction

Photocatalytic conversion of CO₂ into valuable hydrocarbon compounds over photoexcited semiconductor mimics the photosynthesis of green plants through the reduction of CO₂ by water using solar energy. Such artificial photosynthesis provides a sustainable way for carbon cycle and has potential significances in solving energy and environment issues up to date. Photocatalytic CO₂ reduction involves multiple reaction steps to produce useful carbon sources such as CO, HCOOH, HCHO, CH₃OH, and CH₄, varying with the degree of H⁺/e⁻ transfer.¹ As the most abundant and stable oxidized form of carbon, CO₂ is difficult to be activated.² Activation of CO₂ is the most challenging step for CO₂ conversion. Noble metals (Pt, Rh, Au, etc.) with large work functions are excellent cocatalysts on semiconductor photocatalysts as electron sink to promote multielectron transfer process as well as the reaction rate.³ As a consequence, noble metal cocatalysts are strongly relied for photocatalytic CO₂ conversion into hydrocarbon compounds.

Surface chemistry of CO₂ demonstrated that adsorption of CO₂ molecules on the surface of metal or oxide is usually accompanied with activation processes. Compared with the normal molecule, CO₂ in chemisorption state (mainly carbonate and/or CO₂⁻

anion) has a bent O-C-O bond angle and decreased LUMO which will favor the charge transfer from photo-excited semiconductor to the surface adsorbed CO₂ molecules.^{4, 5} Therefore, photocatalytic CO₂ (an acidic molecule) reaction rate can be enhanced by co-loading of both basic metal oxides and noble metal as is reported very recently.⁶ However, additional pressure is still needed to increase the surface fixation of CO₂ on photocatalysts for a relatively high production rate of reduction products. Therefore, effective CO₂ activation and conversion method, especially noble metal free method, is in an urgent need. In this work, the effect of alkali modification on photocatalytic CO₂ conversion was investigated. Direct photocatalytic reduction of CO₂ into CH₄ was found over NaOH/TiO₂ photocatalyst without loading any noble metal cocatalysts. The enhanced CO₂ chemisorption may simultaneously play an important role for the effective activation of CO₂.

4.2 Experimental methods

4.2.1 Photocatalyst preparation

The NaOH/TiO₂ composites were prepared by impregnation of TiO₂ (commercial ST01, anatase form, mean particle size: 5 nm) in aqueous solution containing quantitative NaOH (1, 3, 5, and 7 wt%). The photocatalysts were readily obtained after drying in vacuum oven at 70 °C.

4.2.2 Sample characterization

X-ray diffraction (XRD) patterns were recorded on an X-Pert diffractometer equipped with graphite monochromatized Cu-K α radiation. The specific surface areas were determined with a surface area analyzer (BEL Sorp-II mini, BEL Japan Co.,

Japan) by the Brunauer-Emmett-Teller (BET) method. Transmission electron microscopy (TEM) images were taken by a field emission transmission electron microscope (2100F, JEOL Co., Japan) operated at 200 kV. The diffuse reflection spectra of catalysts were measured by UV-visible spectrophotometer (UV-2500PC, Shimadzu Co., Japan). Surface chemical analysis was performed by X-ray photoelectron spectroscopy (XPS, PHI Quantera SXM, ULVAC-PHI Inc., Japan). A Fourier transform-infrared (FT-IR) spectrophotometer (IR Prestige-21, Shimadzu Co., Japan) was utilized to obtain IR absorption spectra. In-situ FT-IR (FT-IR-6300, JASCO Inc.) measurement was carried out to investigate the mechanism of CO₂ conversion.

4.2.3 Photocatalytic CO₂ conversion

The gas phase photoreduction reaction was carried out in a closed circulation system equipped with a vacuum line. The NaOH-TiO₂ photocatalyst (0.08 g) was dispersed uniformly on a quartz fiber filter with the area of 7 cm². The quartz fiber filter film is fixed on the stage inside the reaction cell. 2 ml of water was injected into the system as reducer. The system was vacuumed and then 80 kPa of CO₂ was introduced. A 300 W Xe lamp was employed as light source.

The contents of CO₂, CO and CH₄ in the reaction system were sampled and measured with a gas chromatograph (GC-14B, Shimadzu) equipped with a flame ionization detector (FID) according to the standard curves. The contents of H₂ were measured with an online gas chromatograph (GC-8A, Shimadzu) with a TCD detector according to the standard curve. Isotope experiments were performed by gas chromatography-mass spectrometry (GC-MS, JMS-K9, JEOL Co., Japan). The apparent quantum efficiency was calculated as following equation,

$$AQE = N(\text{CH}_4) \times 8 / N(\text{Photons}) \times 100\%$$

in which $N(\text{CH}_4)$ and $N(\text{Photons})$ signify the molecular number of generated CH_4 in unit time and the number of incident photons in unit time, respectively.

4.3 Results and discussion

4.3.1 Photocatalytic activity and sample characterization

Photocatalytic CH_4 evolution was fundamentally improved after loading NaOH. With increase of the NaOH loading amount, the evolution amount of CH_4 increased firstly and then decreased (Fig. 4.1a). The optimized loading amount of NaOH was 3 wt% and the corresponding sample generated $52 \mu\text{mol}/(\text{g cat.})$ CH_4 within the first 6 hours' reaction (Fig. 4.1b). The AQE of CH_4 formation at the wavelength of 367.9 ± 10 nm is 0.34%. TiO_2 loaded with 3 wt% NaOH also obtained the best activity for H_2 evolution. Since the present modification of NaOH (TEM image in Fig. 4.2a) did not cause any obvious change in the crystal structure (XRD patterns in Fig. 4.2b), band gap (UV-vis diffused reflectance spectra in Fig. 4.2c), and band position (Valence band-XPS in Fig. 4.2d) of TiO_2 , some other reasons from surface or surface reaction environment should be responsible for the enhanced CO_2 conversion. Because of the acidic nature of CO_2 molecules, increasing the loading amount of strong alkali will favor the surface fixation of CO_2 for the subsequent photoreduction. However, encapsulation by NaOH also induced the aggregation of TiO_2 nanoparticles and thus decreased BET surface area of composite photocatalysts. It is reasonable that the optimized loading amount of NaOH (3 wt%) keeps a good compromise between the CO_2 chemisorption and the surface area of catalyst for heterogeneous CO_2 photoreduction (Fig. 4.3). Isotope experiments using $^{13}\text{CO}_2$ and D_2O as substrate lead

Chapter 4

to the formation of $^{13}\text{CH}_4$ and CD_4 methane, showing that the carbon and hydrogen source of reduction products come from carbon dioxide and water (gas chromatogram and mass spectra in Fig. 4.4 and 4.5).

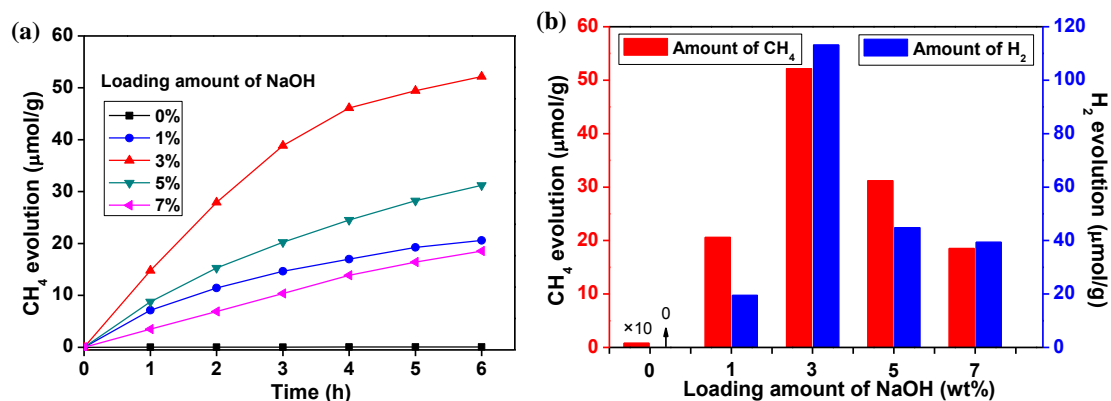


Fig. 4.1. (a) Time course of CH_4 evolution and (b) evolution amounts of CH_4 and H_2 in the first 6 hours' irradiation from photocatalytic CO_2 conversion.

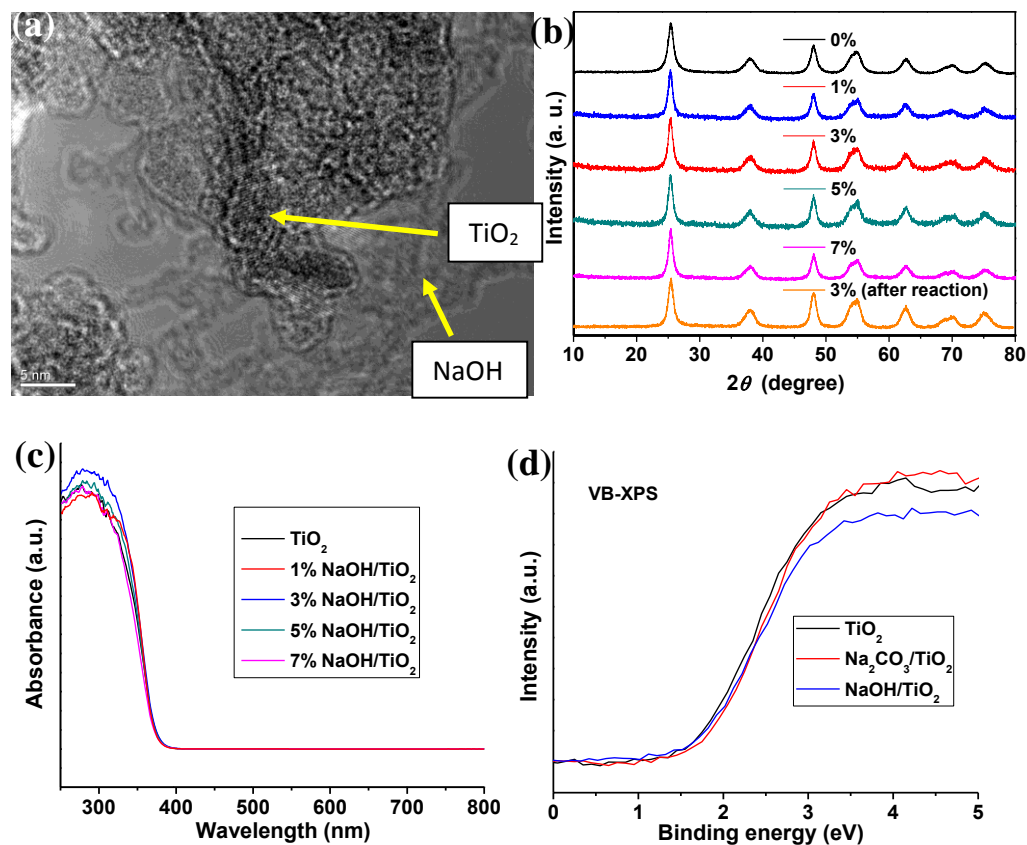


Fig. 4.2. (a) XRD patterns of TiO_2 and NaOH- TiO_2 composites; (b) TEM image of 3 wt% NaOH- TiO_2 composite; (c) UV-Vis diffused reflectance spectra of TiO_2 and NaOH- TiO_2 composites; and (d) Valence band-XPS of TiO_2 , 3.975 wt% Na_2CO_3 - TiO_2 , and 3 wt% NaOH- TiO_2 composites.

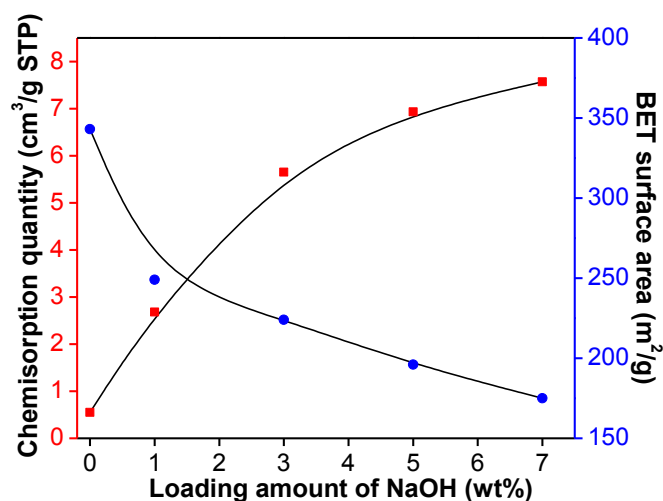


Fig. 4.3. Cumulative CO₂ pulse chemisorption quantity and BET surface area of NaOH/TiO₂ composites.

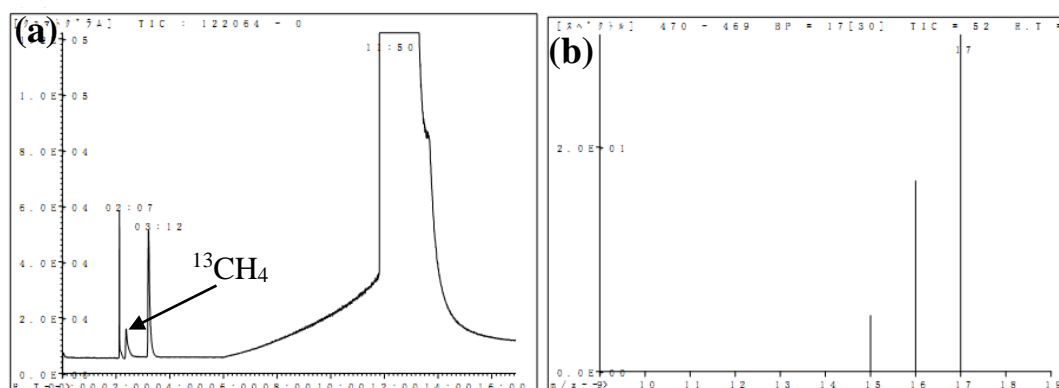


Fig. 4.4. (a) Gas chromatogram and (b) mass spectrum of ¹³CH₄ produced over 3 wt% NaOH-TiO₂ photocatalyst. Carbon dioxide ¹³CO₂ was used.

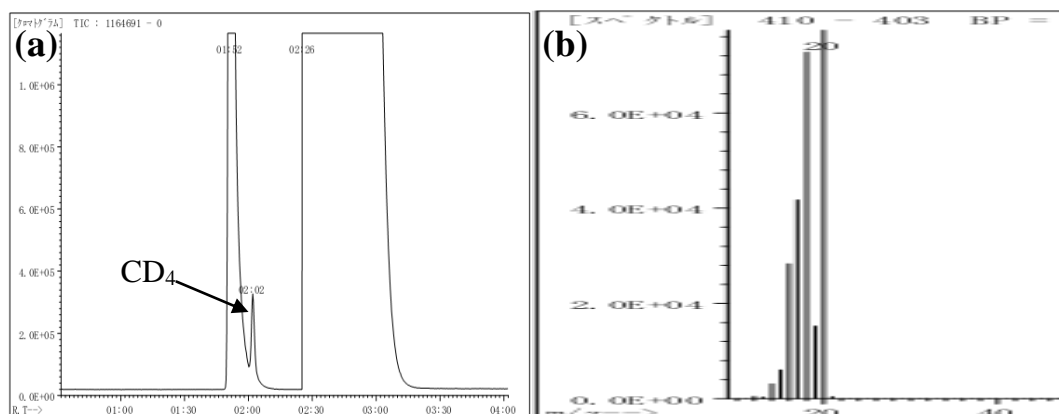


Fig. 4.5. (a) Gas chromatogram and (b) mass spectrum of CD₄ produced over 3 wt% NaOH-TiO₂ photocatalyst. D₂O water (purity 99.9%) was used.

4.3.2 Photocatalytic reaction mechanism

The bare TiO₂ can hardly show any activity for photocatalytic CH₄ evolution and the photoreduction only obviously proceeded after NaOH encapsulation. This fact indicates that gaseous CO₂ molecules is difficult to be reduced under the present test condition and the chemisorption of CO₂ molecules by NaOH possibly accomplished a meaningful activation step and promoted the photocatalytic CO₂ reduction. FT-IR spectra (Fig. 4.6a) displayed that bidentate carbonate species ($\nu_{as}(\text{CO}_3)$: 1340 cm⁻¹; $\nu_s(\text{CO}_3)$: 1550 cm⁻¹)⁷ emerged after loading NaOH. Along with increasing the loading amount of NaOH, the relative absorption intensity of bidentate carbonate species in FT-IR became stronger, indicating that loading of NaOH benefits the formation of bidentate carbonate species which are crucial in the photoreduction of CO₂ to CO and methane.⁸ In-situ FT-IR (Fig. 4.6b) was used to observe the formation of surface species related to the activation of CO₂ on NaOH/TiO₂. The characteristic adsorption bands 1335-1560 cm⁻¹ and 1610-1750 cm⁻¹ are assigned to the bending vibration of C-H, the stretching vibration of C=O and asymmetric stretching of O-C=O, which belong to the intermediate products such as aldehydes, carboxylic acids and bidentate carbonates.⁸ Therefore, transformation of CO₂ into surface carbonates is an important intermediate process for CO₂ photoreduction. This may be related to the change of O-C-O bond angle during the chemisorption of CO₂.⁴ Based on this concept, we further loaded TiO₂ directly with Na₂CO₃, the amount of which was converted from the assumption that all the NaOH (3 wt%) was transformed into Na₂CO₃ (3.975 wt%). The results demonstrated that the evolution amounts of CH₄ decreased when Na₂CO₃ was used (Fig. 4.7). It is supposed that the reaction at valence band side become the rate control step of the overall photocatalytic reaction. The micro-kinetic studies of water photooxidation over TiO₂ and other Ti based semiconductor photocatalysts showed that

the hydroxylation (by OH^- from water dissociation) of surface coordinative unsaturated Ti atom plays the key role in trapping the holes of valence band to produce the hydroxyl radicals, H_2O_2 , or O_2 .⁷ For the case of this work, it can be speculated that TiO_2 will undergo a higher degree of hydroxylation when it is impregnated in NaOH than that in Na_2CO_3 . This process is likely to happen because the high surface area TiO_2 will render abundant surface coordinative unsaturated Ti sites to afford the hydroxylation in high pH solution, which may behave in a similar manner as that of SrTiO_3 .⁸ FT-IR spectra (Fig. 4.8) showed that loading NaOH on TiO_2 increased the relative intensity of OH stretch region ($2800\text{--}3500\text{ cm}^{-1}$),⁷ implying that enhanced hydroxylation occurred by loading the alkaline chemicals.

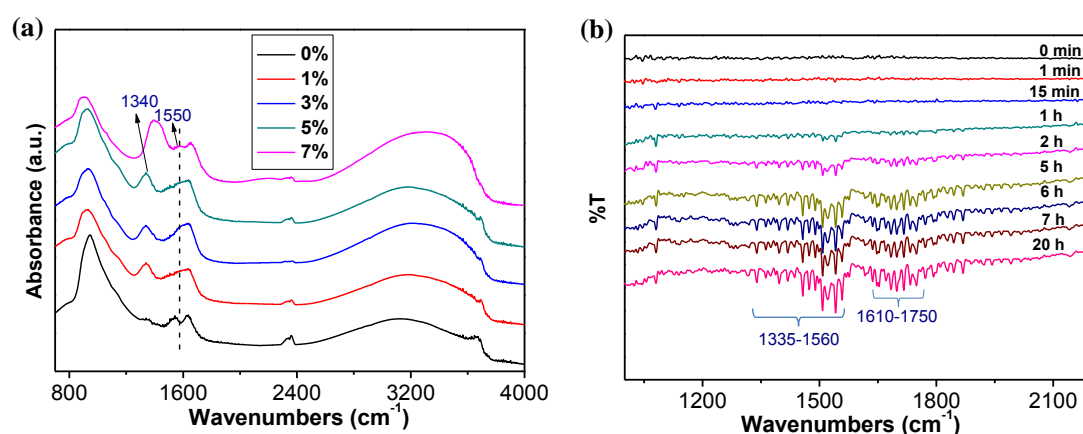


Fig. 4.6. (a) FT-IR spectra of NaOH-TiO_2 composites with different NaOH loading amount and (b) in-situ FT-IR spectra of CO_2 photoreduction over 3 wt% NaOH-TiO_2 photocatalyst at different irradiation times. The in-situ FT-IR spectra were measured in the presence of H_2O and CO_2 atmosphere under the irradiation from a 300W Xe lamp.

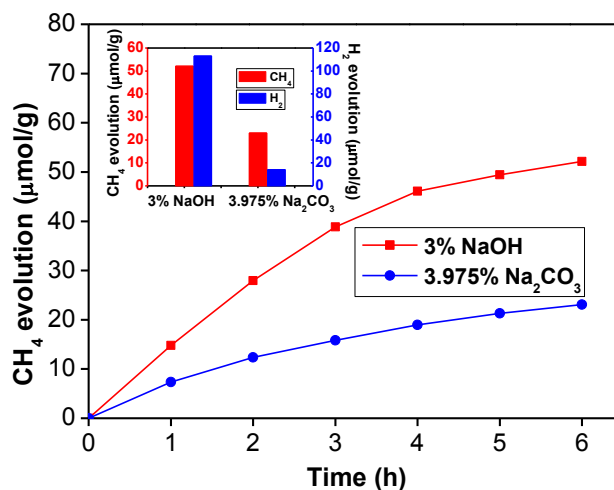


Fig. 4.7. Time course of CH₄ evolution over NaOH/TiO₂ and Na₂CO₃/TiO₂ composites. Inset: evolution amounts of CH₄ and H₂ in the first 6 hours' irradiation from photocatalytic CO₂ conversion.

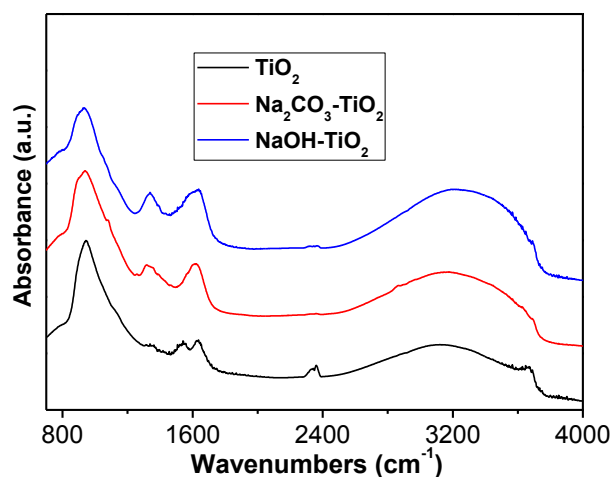


Fig. 4.8. FT-IR spectra of 3 wt% NaOH-TiO₂ and 3.975 wt% Na₂CO₃-TiO₂ composites (OH stretch region 2800-3500 cm⁻¹).

Improved photocatalytic performance of overall water splitting in alkaline reaction environment has also been reported previously⁹⁻¹¹. The hydroxide ions at or near the surface may serve as hole acceptors and decrease the recombination of electron hole recombination. The photooxidation of hydroxyl group will simultaneously provide electrons and protons (hydrogen source) for CO₂ photoreduction. This is consistent with the isotope result which clearly indicated the existence of CD₄ (m/z 20, 18, 16, 14, 12). The CD_xH_{4-x} (x = 0, 1, 2, and 3) can be also identified (m/z 19, 18, 17, 16, 15, 14, 13,

Chapter 4

12) because of the unintentional hydroxylation of TiO_2 in the impregnation process with NaOH in H_2O . Taking a careful observation to Fig. 4.1a again, the linearity of CH_4 evolution curve is improved with the increase of loading amount of NaOH . For the highest loading amount sample (7 wt% NaOH/TiO_2), CH_4 evolution showed a perfect linear characteristic in the first 4 hours, implying that the surface carbonates and hydroxylation are sufficient for both reactions at conduction band (reduction reaction) and valence band (oxidation reaction) sides, while the surface area of NaOH/TiO_2 becomes the control factor for the overall photocatalytic reaction rate when the loading amount of NaOH is higher than 3 wt%. The decay of CO_2 photoreduction rates were observed in Fig. 4.1a. The decline of CH_4 evolution rate observed in this work may be induced by slow diffusion of carbonates or hydroxyl groups in the interface of NaOH and TiO_2 for continuous photoreaction. On the other hand, the back reaction of CO_2 reduction, i.e., the photooxidation of organic intermediates may also suppress the CO_2 conversion.

In this work, CH_4 was the main product from CO_2 photoreduction (with little amount of CO). This is very interesting because photocatalytic CO_2 conversion into CH_4 is an $8\text{H}^+/8\text{e}^-$ transfer reaction.¹ While multiple electron transfer reaction is generally achieved with the help of loading noble metal cocatalysts. Wagner and Somorjai reported direct photocatalytic H_2 production (2e^- reaction) over a noble metal free SrTiO_3 in strong basic medium¹². The hydroxide ions were considered to facilitate the consumption of photo-generated holes. Although the kinetic process of multiple H^+/e^- transfer and detailed process of CO_2 photoreduction need more in situ characterizations for this work, the state of art photoreduction theory of TiO_2 , proton coupled electron transfer (PCET), may be enlightening. In PCET, the transfer of e^- and H^+ are concerted and quantitative.¹³ Recent results indicated that the PCET of TiO_2 is

Chapter 4

very effective for multiple H^+/e^- transfer hydrogenation process, including the nitrogen reduction (ex., nitrobenzene to aniline ($6H^+/6e^-$)¹⁴ and NO_3^- to NH_4^+ ($10H^+/8e^-$)¹⁵) and oxygen reduction (ex., O_2 to water ($4H^+/4e^-$)^{15, 16} and H_2O_2 to water ($2H^+/2e^-$)¹⁵). It is plausible that the photocatalytic CO_2 methanation (carbon reduction, $8H^+/8e^-$) over $NaOH/TiO_2$ may also follow a similar PECT process. The concerted transfer of excited electrons coupled with surface absorbed protons^{13, 17, 18} promotes the effective hydrogenation of carbonates into CH_4 .

The direct multiple H^+/e^- transfer in the absence of noble metal cocatalysts for the photocatalytic CO_2 reduction into CH_4 is very attractive because CH_4 is the ending hydrogenation products according to the multiple step reactions.¹ This means the reaction process in the present work is very effective in energy conversion from solar energy to chemical energy. We also investigated the effects of noble metal Pt (considered as excellent hydrogenation cocatalyst generally, loading amount 1 wt%) on the photocatalytic CH_4 evolution over $NaOH/TiO_2$. The results showed that activity of $Pt/NaOH/TiO_2$ was lower than $NaOH/TiO_2$ photocatalyst (Fig. 4.9). This may be caused by the back reaction between intermediate of CO_2 reduction and O_2 over $Pt/NaOH/TiO_2$. Similar back reactions between evolved H_2 and O_2 to form water also readily proceeds in overall water splitting because of an uphill reaction.^{3, 19}

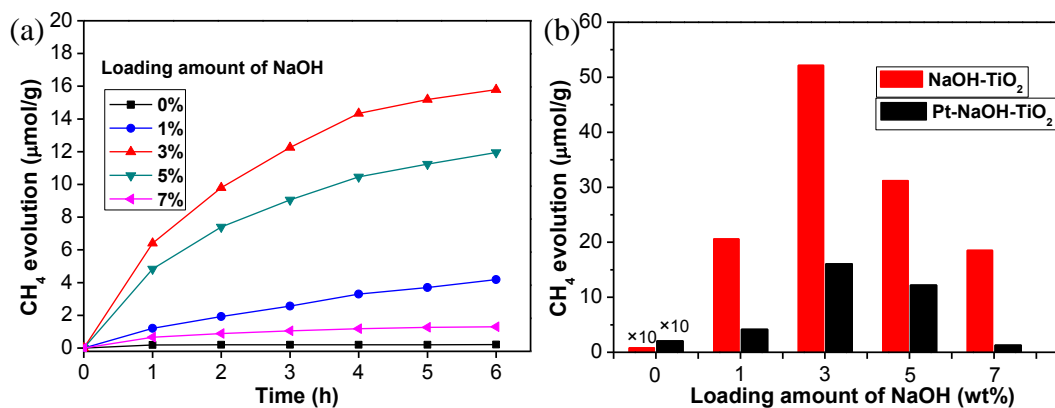


Fig. 4.9. (a) Time course of CH₄ evolution over 1 wt% Pt-NaOH-TiO₂ photocatalysts; and (b) evolution amounts of CH₄ over NaOH-TiO₂ and 1 wt% Pt-NaOH-TiO₂ in the first 6 hours' irradiation from photocatalytic CO₂ conversion. The loading of 1 wt% Pt on TiO₂ was prepared by photodeposition method in aqueous solution containing H₂PtCl₆ and methanol. The obtained Pt-TiO₂ was heated at 200°C in air for 1 hour to remove the methanol. Finally, Pt-TiO₂ was impregnated in NaOH solutions.

Conclusions

In summary, surface modification of TiO₂ with alkali was found to be an effective way for the CO₂ adsorption, activation, and lead to highly effective conversion of CO₂ into CH₄ without any noble metal cocatalyst loaded. Two important findings of this work are, first, the chemisorption of CO₂ by alkali can provide a simple activation method for the photocatalytic CO₂ conversion; second, in the absence of noble metal cocatalysts, TiO₂ can promote the direct photocatalytic reduction of carbonate into CH₄ which may be driven by PCET in the interface of TiO₂ and NaOH (or Na₂CO₃). Surface modification of TiO₂ with alkali may also find applications in other photosynthesis processes.

In order to further enhance the current CO₂ conversion efficiency, H₂ and CH₄ were used as hydrogen sources for CO₂ conversion in chapter 5. The influences of SPR-

induced photothermal or local electric field on these reactions were investigated.

References

1. S. N. Habisreutinger, L. Schmidt-Mende and J. K. Stolarczyk, *Angew. Chem. Int. Ed.*, 2013, **52**, 7372-7408.
2. W. Wang, S. Wang, X. Ma and J. Gong, *Chem. Soc. Rev.*, 2011, **40**, 3703-3727.
3. A. Kudo and Y. Miseki, *Chem. Soc. Rev.*, 2009, **38**, 253-278.
4. H. J. Freund and M. W. Roberts, *Surf. Sci. Rep.*, 1996, **25**, 225-273.
5. V. P. Indrakanti, J. D. Kubicki and H. H. Schobert, *Energy Environ. Sci.*, 2009, **2**, 745-758.
6. S. Xie, Y. Wang, Q. Zhang, W. Fan, W. Deng and Y. Wang, *Chem. Commun.*, 2013, **49**, 2451-2453.
7. M. R. Hoffmann, S. T. Martin, W. Choi and D. W. Bahnemann, *Chem. Rev.*, 1995, **95**, 69-96.
8. S. Ouyang, H. Tong, N. Umezawa, J. Cao, P. Li, Y. Bi, Y. Zhang and J. Ye, *J. Am. Chem. Soc.*, 2012, **134**, 1974-1977.
9. S. Sato and J. M. White, *J. Catal.*, 1981, **69**, 128-139.
10. K. Yamaguti and S. Sato, *J. Chem. Soc., Faraday Trans. 1*, 1985, **81**, 1237-1246.
11. H. Mizoguchi, K. Ueda, M. Orita, S.-C. Moon, K. Kajihara, M. Hirano and H. Hosono, *Mater. Res. Bull.*, 2002, **37**, 2401-2406.
12. F. T. Wagner and G. A. Somorjai, *Nature*, 1980, **285**, 559-560.
13. J. N. Schrauben, R. Hayoun, C. N. Valdez, M. Braten, L. Fridley and J. M. Mayer, *Science*, 2012, **336**, 1298-1301.

Chapter 4

14. X.-X. Zou, G.-D. Li, K.-X. Wang, L. Li, J. Su and J.-S. Chen, *Chem. Commun.*, 2010, **46**, 2112-2114.
15. H. H. Mohamed, C. B. Mendive, R. Dillert and D. W. Bahnemann, *J. Phys. Chem. A*, 2011, **115**, 2139-2147.
16. J. Rosenthal and D. G. Nocera, *Acc. Chem. Res.*, 2007, **40**, 543-553.
17. L. A. Lyon and J. T. Hupp, *J. Phys. Chem. B*, 1999, **103**, 4623-4628.
18. A. Fujishima, X. Zhang and D. A. Tryk, *Surf. Sci. Rep.*, 2008, **63**, 515-582.
19. K. Maeda, K. Teramura, D. Lu, N. Saito, Y. Inoue and K. Domen, *Angew. Chem. Int. Ed.*, 2006, **45**, 7806-7809.

Chapter 5 Plasmon-mediated CO₂ activation and conversion with active hydrogen source

5.1 Introduction

Solar fuel production from CO₂ conversion provides an attractive way to obtain clean energy by mitigating the greenhouse gas. Ideal CO₂ conversion pathway should mimic the photosynthesis of green plants by using abundant H₂O as the hydrogen source. However, due to the kinetic limitations of multiple e⁻/H⁺ transfer process in CO₂ reduction, the current artificial photosynthesis over semiconductor photocatalyst can only achieve an impractical reaction rate in (nmol-μmol)h⁻¹g⁻¹.¹ In this chapter, photothermal CO₂ conversion over Ru nanocatalysts realized a much higher reaction rate (molh⁻¹g⁻¹). This is due to several crucial features of the Ru nanocatalyst, including effective energy utilization over the whole range of the solar spectrum, excellent photothermal performance, and unique activation abilities. However, the consumption of H₂ as active hydrogen source results in a conversion process with no net energy storage because of a downhill reaction ($\Delta G < 0$). The drawbacks of both H₂O and H₂ motivate us to seek other hydrogen source for practical CO₂ conversion reactions which should meet two conditions: (i) the reactant is capable of providing active H source for CO₂ conversion at a considerable reaction rate, and (ii) an uphill-type reaction is necessary to realize the net energy conversion from solar energy to chemical energy. In this case, the abundant natural gas (mainly methane) becomes the preferred choice. Catalytic CO₂ reforming of methane (i.e., dry reforming of methane,

Chapter 5

DRM) is an important reaction to produce the useful syngas ($\text{CO} + \text{H}_2$) and mitigate greenhouse gas. Such reaction system can be deployed in the methane-abundant region to produce syngas which will be further utilized as industrial feedstocks or high-energy fuel. DRM is an extremely endothermic reaction ($\Delta H_{298\text{K}} = +247 \text{ kJ mol}^{-1}$) with obvious uphill feature.² The typical reaction of DRM uses the supported Group VIII metals co-loaded with alkaline metal oxides as promoters. Group VIII metal and alkaline metal oxides play the role in the activation of CH_4 (dehydrogenation) and CO_2 , respectively. High reaction barriers associated with the simultaneous activation of the two nonpolar molecules, CH_4 (tetrahedral structure) and CO_2 (linear structure), require this reaction to be run at high temperatures ($\sim 800 \text{ }^\circ\text{C}$),² which compromises energy input and long-term stability of catalyst.

Surface plasmon-enhanced catalytic process is a rapidly developing subject. The enhanced photocatalytic performance of plasmonic nanometals loaded semiconductor photocatalysts mainly originates from i) surface plasmon resonance (SPR) mediated hot electron transfer and ii) near-field electromagnetic enhancement.³ Plasmonic nanometals can be also directly loaded on an insulator to drive a chemical reaction independently through direct plasmonic photocatalysis or photothermal catalysis.⁴ Besides the direct hot electron transfer from plasmonic nanometals to adsorbates in the regime of direct plasmonic photocatalysis, the dipole nature of the surface plasmon field is able to attract the polar molecules and polarize the nonpolar molecules in the vicinity of plasmonic nanometals.⁵ This property offers a potential pathway for the activation of reactants, especially for the nonpolar molecules which are considered relatively more difficult to be activated than polar molecules in conventional thermocatalysis. Although Group VIII metallic nanocatalysts are extensively used in conventional thermocatalysis, their SPR effects are much weaker than the coinage

metals of Group IB (Ag, Au and Cu) in the visible light range.⁶ In this work, DRM is carried out at low temperature (500 °C) over Rh/SBA-15 (SBA-15: mesoporous SiO₂) and Rh-Au/SBA-15. No obvious photo-enhancement effect was observed over Rh/SBA-15 when varying the light intensity and wavelength. However, over Rh-Au/SBA-15 catalysts, a remarkable photo-enhancement effect was observed when exciting the plasmonic absorption band of Au nanoparticles (NPs) under visible light. Based on the analysis of the rate-limiting step and the results of electromagnetic simulation, it is supposed that the enhanced reaction rate of DRM is attributed to the assisted activation effect by the excitation of SPR of Au NPs. Interparticle coupling between Au NPs and Rh NPs greatly enhanced the SPR effect under visible light.

5.2 Experimental methods

5.2.1 Catalyst preparation

(1) Catalysts for photothermal CO₂ conversion with H₂

The catalysts were prepared by impregnation of mesoporous Al₂O₃ (BET surface area 136 m²g⁻¹) in precursor solution of Ru₃(CO)₁₂. After dried at 70 °C, the samples were heat treated in 300 °C for 2 hours. The loading amount of Ru is measured to be 2.4 wt% by ICP-OES method.

(2) Catalysts for CO₂ reforming of CH₄

A mesoporous SiO₂, SBA-15 (BET surface area 815 m²g⁻¹), was used as support of the catalysts. Firstly, Au/SBA-15 was prepared by deposition-precipitation method using urea (CO(NH₂)₂, Wako) as the precipitating base, which permits the gradual and homogeneous addition of hydroxide ions in the reaction solution. In a typical procedure, 1.0 g SBA-15 was dispersed into 100 ml of an aqueous solution of HAuCl₄

and urea (0.19 M). The suspension maintained at 80 °C was vigorously stirred for 4 h (pH increases), then centrifuged, washed, dried, and calcined at 400 °C for 4 h. As received Au/SBA-15 was further impregnated with RhCl₃ in water, then dried and calcined at 400 °C for 4 h. The amounts of Au and Rh precursor in the both preparation steps are 1 wt% of the added SBA-15.

5.2.2 Sample characterization

X-ray diffraction (XRD) patterns were recorded on an X-Pert diffractometer equipped with graphite monochromatized Cu-K α radiation. The specific surface areas were determined with a surface area analyzer (BEL Sorp-II mini, BEL Japan Co., Japan) by the Brunauer-Emmett-Teller (BET) method. Transmission electron microscopy (TEM) images were taken by a field emission transmission electron microscope (2100F, JEOL Co., Japan) operated at 200 kV. The diffuse reflection spectra of catalysts were measured by UV-3600 UV-Vis-NIR spectrophotometer (SHIMADZU Co., Japan) from 220 nm to 2600 nm. The loading amounts of VIII group elements on the support were analyzed by inductively coupled plasma optical emission spectrometry (ICP-OES, SPS3520UV-DD, SII nano technology Inc., Japan). The catalyst temperature was probed by a digital thermometer (CT-1200D, CUSTOM Co., Japan). Surface chemical analysis was performed by X-ray photoelectron spectroscopy (XPS, PHI Quantera SXM, ULVAC-PHI Inc., Japan). Carbon analysis was performed on a thermogravimetry analyzer (DTG-60H, SHIMADZU).

5.2.3 Photothermal CO₂ conversion with H₂

Photothermal CO₂ conversion by H₂ was carried out in a batch type reaction system with a total volume of 330 ml (Fig. 5.1). After evacuation of reaction system, 2-2.05 mmol CO₂ and 8.2-8.5 mmol H₂ (the molar ratio of H₂ to CO₂ is slightly larger

Chapter 5

than 4:1) were injected. A 300 W Xe lamp was used as irradiation source to drive the photothermal CO₂ conversion. For all experiments, 0.1 g of sample was used and spread onto a round shape air-permeable quartz fiber filter with the area of 7 cm². The quartz fiber filter film is fixed on the stage inside the reactor. The tip of thermometer was maintained an intimate contact to the sample (thickness of catalyst powder is about 1-2 mm).

The contents of CO₂, CO and CH₄ in the reaction system were sampled and measured with a gas chromatograph (GC-14B, Shimadzu) equipped with a flame ionization detector (FID) according to the standard curves. The contents of H₂ were measured with an online gas chromatograph (GC-8A, Shimadzu) with a TCD detector according to the standard curve. Isotope experiments were performed by gas chromatography-mass spectrometry (GC-MS, JMS-K9, JEOL Co., Japan).



Fig. 5.1. Setup of experiment.

5.2.4 CO₂ reforming of CH₄ under visible light

The DRM reaction was carried out in a flow type reaction system at 500 °C (Fig. 5.2c). The molar ratio of CH₄/CO₂ is 1:1, flow rate was controlled at 20.0 mL/min by chemisorption analyser (Fig. 5.2a), and 0.0050 g catalyst was used. A 300 W Xe lamp was used as light source and output irradiation was regulated by L42+HA30 filter set to obtain visible light (400-800 nm) with the total light intensity 0.22 W/cm² (Fig.

5.2b).



Fig. 5.2. Setup of experiment.

5.3 Results and discussion

5.3.1 Photothermal CO₂ conversion with H₂

Under photoirradiation, Ru/Al₂O₃ shows excellent reaction rate for CO₂ conversion with high CH₄ selectivity (Fig. 5.3a). UV/Vis/NIR spectra indicate that Ru/Al₂O₃ catalyst is excellent absorbers over a very broad photo-irradiation range that covers ultraviolet light, visible light, and infrared radiation (Fig. 5.3b). The intense absorption implies that a high utilization efficiency of solar energy would be feasible. Monitoring of the catalyst temperature demonstrated that the photoirradiation induced a significant thermal effect (Fig. 5.4). The temperature of Ru/Al₂O₃ catalyst reached approximately 200 °C within the first minute, whereas the temperature of pure Al₂O₃ support in a control experiment was measured to be approximately 80 °C. Under continuous photoirradiation, Ru/Al₂O₃ catalysts reached a reaction temperature of about 400 °C, which was > 200 °C higher than that of pure Al₂O₃ support. The excellent photothermal properties in conjunction with the unique activation ability of the Ru/Al₂O₃ nanocatalysts favor the highly efficient photoinduced CO₂ conversion. No additional enhancement effects on the CO₂ conversion that are due to the irradiation were observed. We then compared the CH₄ evolution over the Ru/Al₂O₃ catalyst under thermal and photothermal conditions (Fig. 5.5). In both experiments,

Chapter 5

the onset temperatures were found to be approximately 140 °C. No obvious differences between the CH₄ evolution curves for the two sets of conditions were found. To investigate whether CO₂ hydrogenation is affected by photocatalytic processes (photoexcitation processes), the CH₄ evolution over the Ru/Al₂O₃ catalyst was measured under irradiation with monochromatic light. With this method, the thermal effect was effectively suppressed (no obvious temperature increase was observed, and the temperature remained at ca. 21-23 °C over the whole experiment). We selected some typical monochromatic light filters (441, 502, 549, 601, and 710 nm) in the visible-light range for this test (Fig. 5.6a). It was found that the CH₄ evolution rate (CO evolution was not observed) was very low (ca. 0.02 mmol/100 min) in the dark, and this evolution rate remained almost unchanged no matter which monochromatic light was used (Fig. 5.6b). This result reflects the fact that photo-induced CO₂ methanation over Ru/Al₂O₃ is not mediated by photocatalysis, but by a photothermal effect. Ru/Al₂O₃ shows good cycle performance for photothermal CO₂ conversion (Fig. 5.7). No obvious changes were observed with respect to nanoparticle size and distribution for the Ru after photothermal reactions (Fig. 5.8). After the reaction, binding energy of Ru 3d shifted to the lower value (Fig. 5.9), indicating that amount of metallic Ru increased. It is easy to imagine that Ru will be slightly reduced after the methanation reaction under the H₂ atmosphere and high temperature.

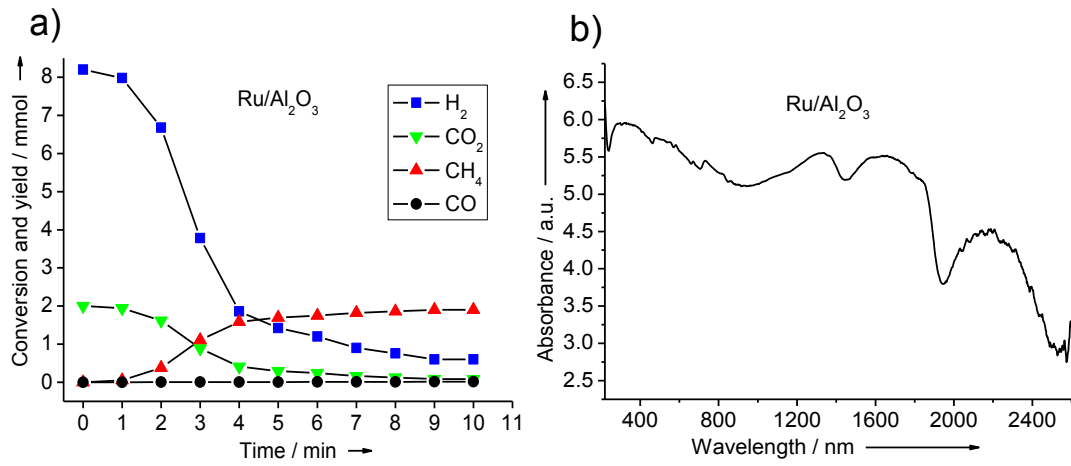


Fig. 5.3. a) Photothermal CO₂ conversion performance and b) UV-Vis-NIR spectrum of Ru/Al₂O₃ catalyst.

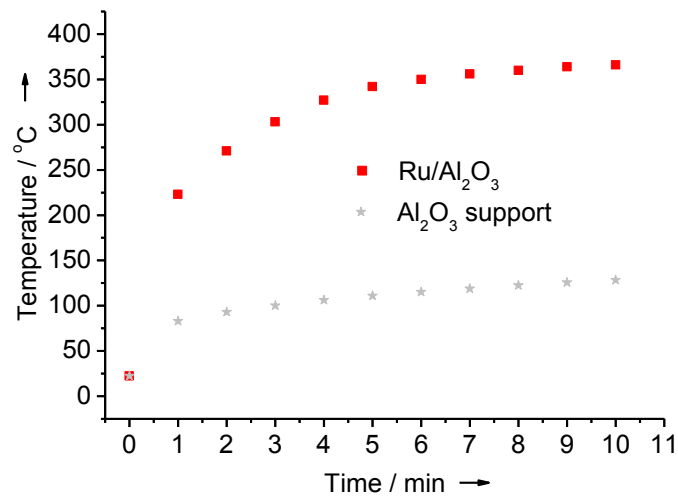


Fig. 5.4. Monitoring of catalyst temperature.

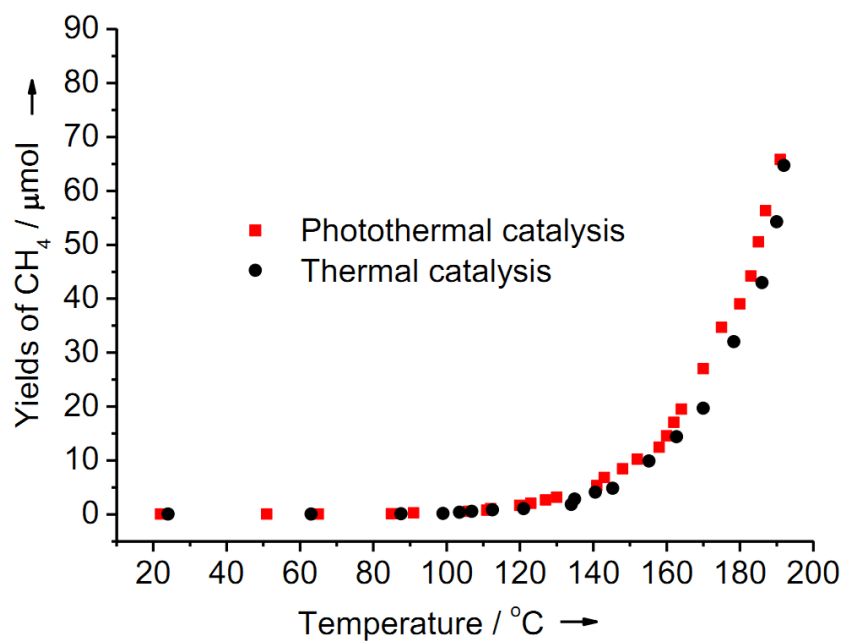


Fig. 5.5. CH₄ evolution over Ru/Al₂O₃ catalyst under photothermal and thermal catalysis condition. Under both conditions, the heating rate (4-5 °C/min between 50-190 °C) was respectively controlled by output current of light source (300 W Xe lamp) in photothermal catalysis and oil-bath in thermal catalysis.

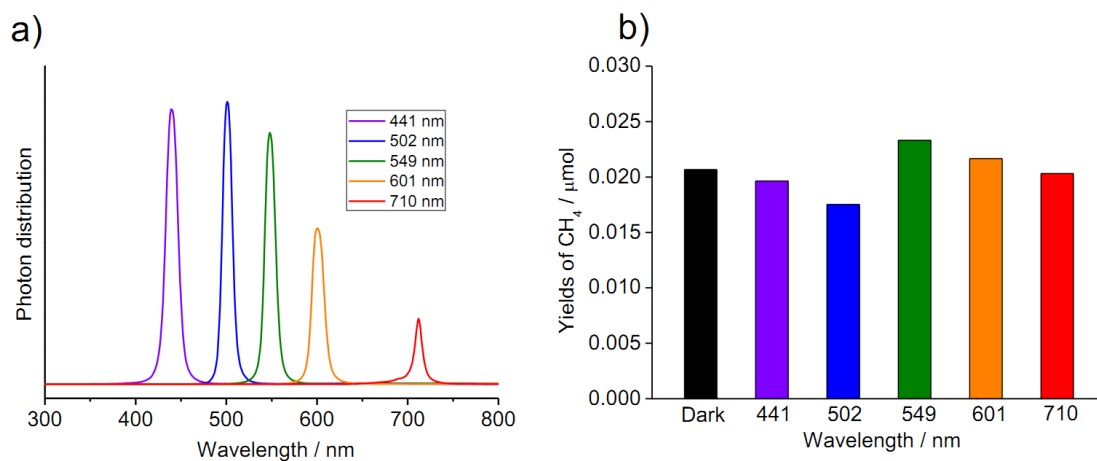


Fig. 5.6. a) Photon distribution of monochromatic light and b) CH₄ evolution amount over Ru/Al₂O₃ catalyst under dark condition and the irradiation of monochromatic light for 100 min.

Chapter 5

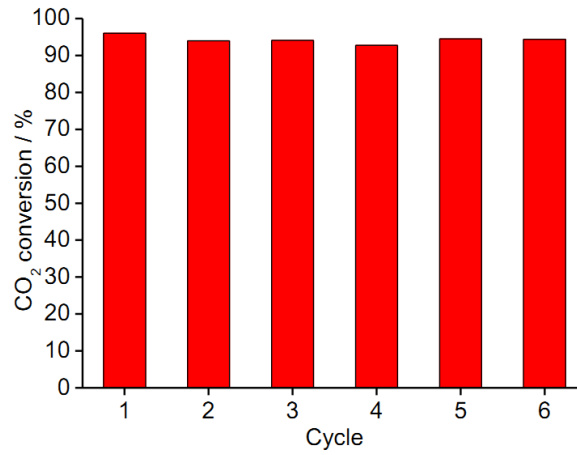


Fig. 5.7. Cycle performance of Ru/Al₂O₃ catalyst for photothermal CO₂ conversion. The duration of each cycle is 10 min.

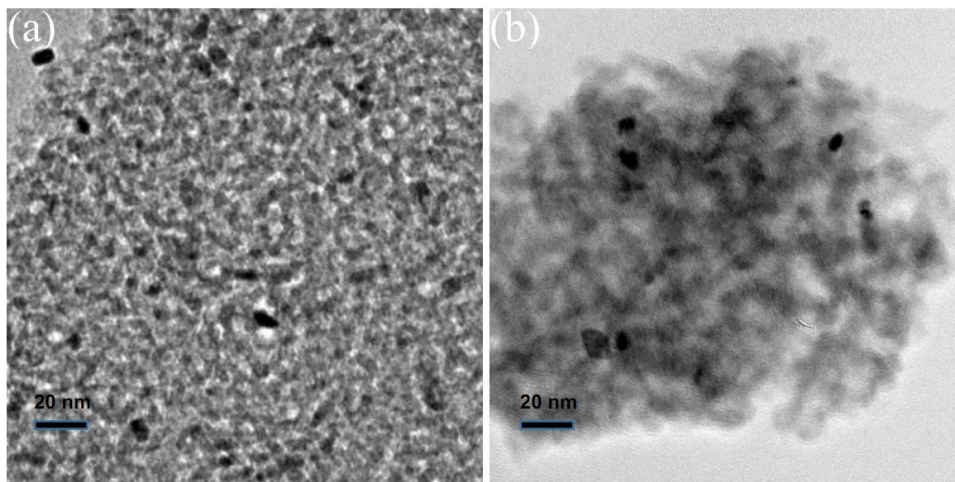


Fig. 5.8. TEM images of Ru/Al₂O₃ a) before and b) after reaction.

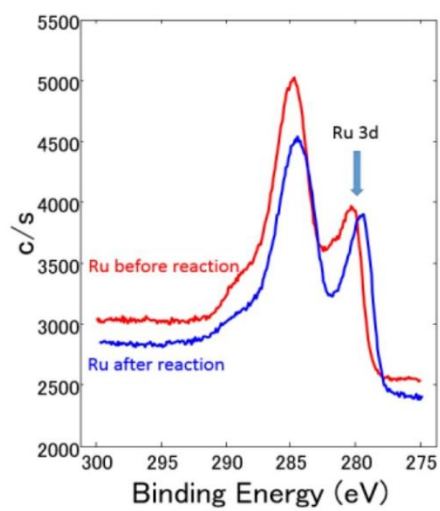


Fig. 5.9. XPS spectra of Ru/Al₂O₃ a) before and b) after reaction.

Chapter 5

Wide-band-gap semiconductors ($E_g > 3$ eV), such as Ti-, Nb-, Ta-, Ga-, and Ge-based oxides with adequate redox potentials, constitute the main materials for photocatalytic CO_2 conversion, which are highly dependent upon excitation by ultraviolet irradiation (which only accounts for 4% of the total solar energy). In contrast to traditional photocatalytic methods, the photothermal CO_2 conversion over $\text{Ru}/\text{Al}_2\text{O}_3$ catalysts does not require ultraviolet irradiation as the excellent absorption of visible light and infrared radiation (which together account for 96% of the total solar energy) can effectively drive photothermal CO_2 conversion. In the absence of ultraviolet light, photothermal CO_2 conversion can still proceed over the $\text{Ru}/\text{Al}_2\text{O}_3$ catalyst (Fig. 5.10). Therefore, $\text{Ru}/\text{Al}_2\text{O}_3$ catalysts are advantageous over traditional photocatalysts because of the highly efficient utilization of solar energy and in particular of the low-energy photons of visible light and infrared radiation.

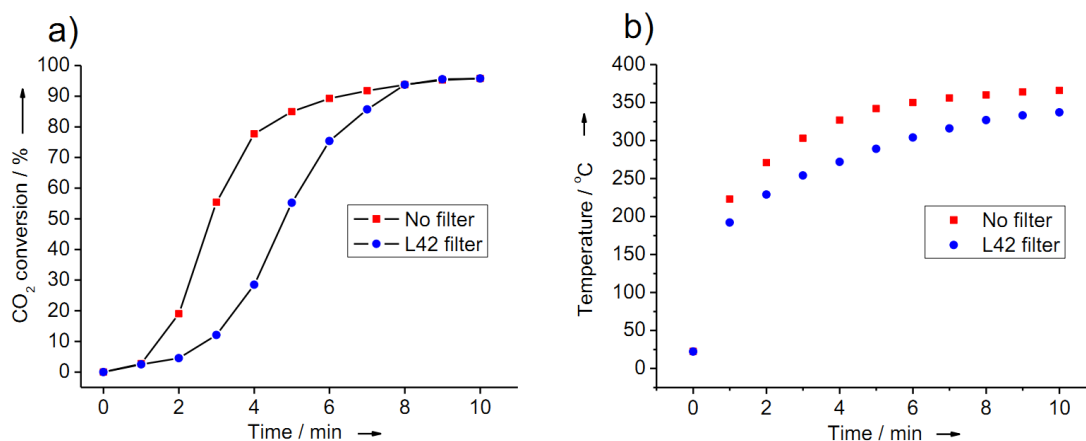


Fig. 5.10. a) Photothermal CO_2 conversion b) and temperature monitoring over $\text{Ru}/\text{Al}_2\text{O}_3$ catalyst under irradiation with and without ($\lambda > 400$ nm, cut-off filter L42) UV light.

Although photothermal CO_2 conversion shows much higher CO_2 reaction rate than conventional photocatalytic method, H_2 consumption makes the reaction have no net energy conversion from solar energy to chemical energy. In order to overcome this drawback, CH_4 was used to replace H_2 as an active hydrogen source in the next

section. The enhanced catalytic performance by the excitation of the SPR of Au NPs was investigated.

5.3.2 CO₂ reforming of CH₄ under visible light

TEM images in Fig. 5.11 show that the average particle size of Au on Au/SBA-15 and Rh-Au/SBA-15 catalysts is about several tens of nanometers, whereas Rh particles is difficult to be observed on the Rh/SBA-15 and Rh-Au/SBA-15, despite the fact that the existence of both Rh and Au could be detected through XPS (Fig. 5.11f) and ICP (Table 5.1) analysis, indicating the Rh clusters are very small and well dispersed on the SBA-15. This was consistent with the result that only crystalline Au can be clearly detected in the XRD patterns (Fig. 5.11e). The binding energy of 307.9 eV ($3d^{5/2}$) and 312.8 eV ($3d^{3/2}$) in the XPS results indicate the existence of metallic state of Rh. Rh NPs can be identified in the TEM image (Fig. 5.11d) after reaction although the Rh particle size after reaction is still much smaller than that of Au NPs, showing that Rh clusters undergo aggregation and growth in the photothermal reaction.

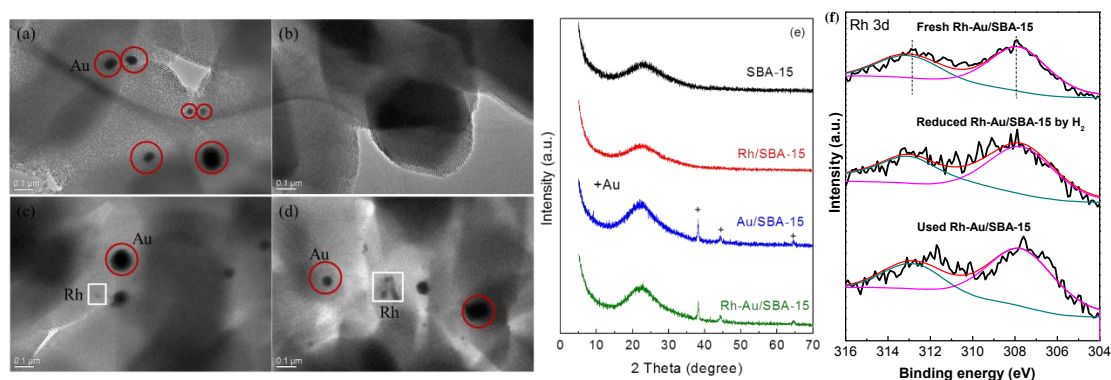


Fig. 5.11. TEM images of (a) fresh Au/SBA-15, (b) fresh Rh/SBA-15, (c) fresh Rh-Au/SBA-15 and (d) used Rh-Au/SBA-15. (e) XRD patterns of SBA-15 supported catalysts and (f) XPS patterns supported Rh clusters.

Chapter 5

Table 5.1 Elemental analysis and specific surface areas of the catalysts

Samples	Rh (wt. %)	Au (wt. %) ^a	Specific surface area (m ² /g) ^b
1% Rh/SBA-15	1.10	-	501
1% Au/SBA-15	-	0.80	322
1% Rh-1% Au/SBA-15	1.50	0.72	375

a, analyzed by ICP-OES method;

b, obtained by N₂ adsorption-desorption method through Brunauer-Emmett-Teller (BET) equation.

The catalytic performances of the catalysts for DRM were evaluated and the results are displayed in Fig. 5.12 and 5.13. With the increase of reaction time, a decay of the catalytic performance was observed due to the carbon deposition (Table 5.2). Without the irradiation of visible light, Au/SBA-15 catalyst almost exhibited no activity for DRM, while the performance was fundamentally improved over Rh/SBA-15 and Rh-Au/SBA-15 catalysts. To initialize the DRM, CH₄ should be firstly cleaved to form the active species CH_x by Rh, which then activated by CO₂ to generate CO. With the same loading amount of Rh, Rh/SBA-15 and Rh-Au/SBA-15 showed similar catalytic activity (CH₄ and CO₂ conversion, or H₂ and CO yield) in the pure thermal condition. The result was coincident with the earlier report which unambiguously demonstrated that Au didn't possess any ability to improve the catalytic performance for DRM.⁷ With the irradiation of visible light, the performance of Rh/SBA-15 almost remained constant with the variation of light intensity. However, Au/SBA-15 and Rh-Au/SBA-15 catalysts show an enhanced activity in DRM. As shown in Fig. 5.13, both the conversions of CO₂ and CH₄ slightly increased with increase of light intensity over Au/SBA-15 catalyst, from which it could be speculated that for DRM reaction over Au/SBA-15 catalyst, CH₄ could be faintly activated by the excited Au NPs. On

the contrary, the conversions of CO_2 and CH_4 were enhanced remarkably on Rh-Au/SBA-15 catalyst. The enhancement of the reaction rate ($R_{\text{Rh-Au/SBA-15}} - R_{\text{Rh/SBA-15}}$) is more than ten times larger than that of Au/SBA-15 catalyst at the same condition. Because CH_4 cleavage can proceed effectively in the presence of Rh catalysts, the activation of CO_2 becomes the rate-limiting step of the present DRM reaction. The enhanced catalytic performance of Au-containing sample further implies that the Au can promote the activation of CO_2 under visible light irradiation. The catalytic activities increases as the light intensity gets stronger in the range of 0-0.3 W/cm^2 . However, a higher light intensity did not further favor the catalytic performance.

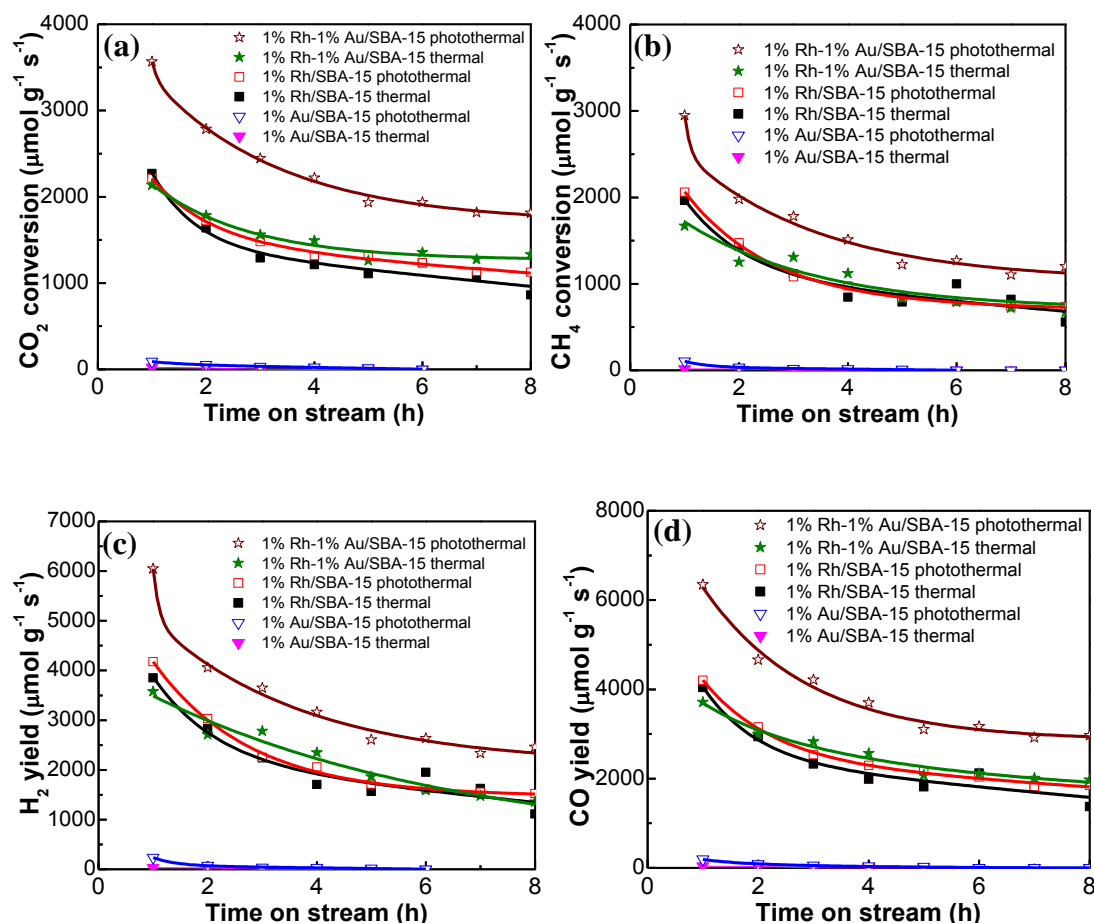


Fig. 5.12. (a) CH_4 and (b) CO_2 conversion, and (c) H_2 and (d) CO yield over the catalysts under different conditions. Reaction conditions: 500 °C, molar ratio $\text{CH}_4/\text{CO}_2 = 1$, flow rate 20.0 mL/min, 0.0050 g catalyst, with or without 0.22 W/cm^2 light irradiation.

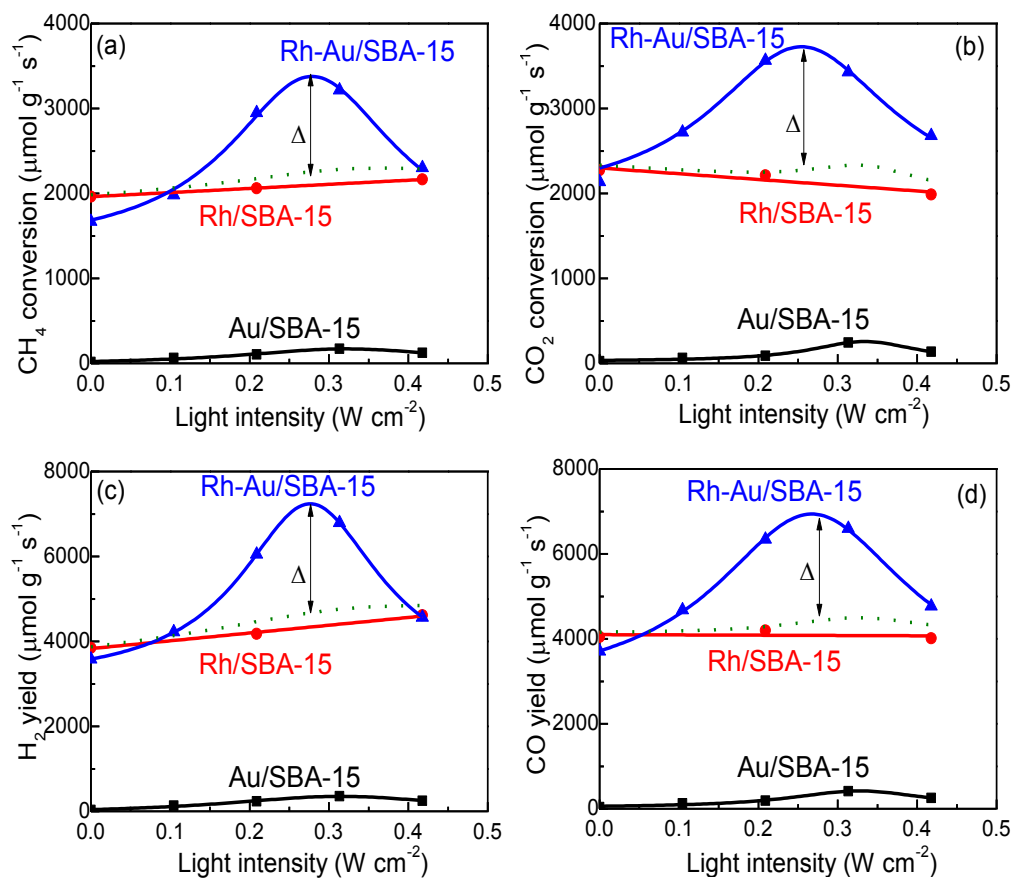


Fig. 5.13. (a) CH₄ and (b) CO₂ conversion, and (c) H₂ and (d) CO yield in the first hour of reaction. The results are obtained from Fig. 5.12.

Table 5.2 Carbon analysis of the spent catalysts

Catalyst	Reaction conditions	Carbon deposition (wt. %) ^a
Rh/SBA-15	thermal	3.0
	photothermal	2.7
Au/SBA-15	thermal	0.5
	photothermal	0.9
Rh-Au/SBA-15	thermal	2.8
	photothermal	2.7

a. analyzed by TGA method.

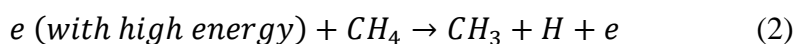
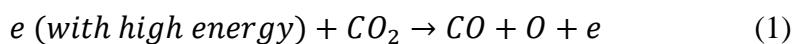
5.3.3 Optical simulations and the mechanism of enhanced activity

Interestingly, Au NPs which have no activation ability for both CH₄ and CO₂ in conventional thermocatalysis, display obvious activation ability under the visible light irradiation. Exactly, the enhanced catalytic performance originates from the excitation of SPR of Au NPs. To confirm this, the influence of the light wavelength on DRM was investigated over Rh-Au/SBA-15. Several types of filters was used to obtain desired wavelength range (Fig. 5.14a). The light intensities of 305-485 nm, 485-520 nm, and 620-745 nm were 17300, 160, and 12050 $\mu\text{W}/\text{cm}^2$, respectively. Through the excitation of Au SPR band (Fig. 5.14b) by the wavelength of 490-550 nm, an enhanced catalytic activity was obviously observed, while the performance under the irradiation away from the SPR band (< 500 nm or > 620 nm) shows comparable activity with the pure thermal condition (Fig. 5.14c, d). Because the light intensity adopted to excite Au LSPR was quite low and is about one hundredth of the other two cases, it was speculated that the excitation of Au SPR band promoted the catalytic performance of Au-containing catalysts in DRM.

For Au-based catalysts, with the irradiation of visible light, Au LSPR could be triggered and positive ions and electrons could be generated on its local surface,^{8, 9} which could be considered as a kind of plasma. The movement of the generated positive ions and electrons could induce electromagnetic field, with its intensity serving as an indicator of the energetic electrons. In order to study Au LSPR, the electromagnetic fields of the catalysts were simulated by the rigorous coupled-wave analysis (RCWA) and finite-difference time-domain (FDTD) methods, with the results displayed in Fig. 5.15. Note that the ordinary Rh NPs only show plasmonic behavior in UV range,⁶ the experiment in this work was carried out under visible light and will only cause weak SPR effect on Rh NPs (Fig. 5.15a). By contrast, the Au NPs

Chapter 5

with sparse distribution show higher SPR effect when using the excitation wavelength of SPR band of Au NPs (Fig. 5.15b). The SPR effect is further dramatically amplified through the interparticle coupling between the Rh NPs and the co-loaded Au NPs (Fig. 5.15c). With the irradiation of visible light (taking 530 nm single wavelength light as an example), the electrons in Au particles have the tendency to escape from its Fermi level to the surfaces with an energy of 1.8 eV vs. SHE, and the energy could be further increased at the more intensive electromagnetic field. What's more, at elevated temperature (500 °C), the free electrons move more randomly and violently due to thermal excitation and become more energetic.¹⁰ Considering the properties of plasma and Au LSPR, it could be speculated that CO₂ and CH₄ could be partially polarized by the plasmonic nanometals^{5, 11} and electronically excited by the highly energetic plasmon electrons via collisional processes¹²⁻¹⁴ (steps (1) and (2), shown below).



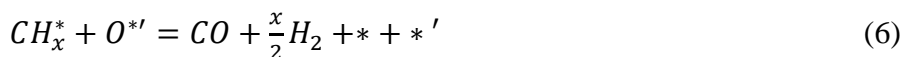
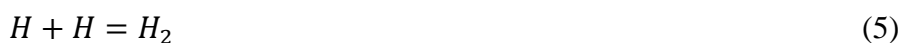
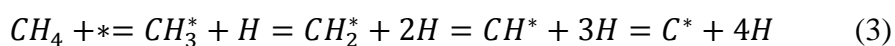
Therefore, the catalytic activities of Au/SBA-15 and Rh-Au/SBA-15 increased with light intensity in the range of 0-0.22 W cm⁻² (Fig. 5.13). However, excessive light irradiation was not favorable for the reaction and the performance deteriorated with the light intensity further increased to 0.44 W cm⁻² (Fig. 5.13). The melting point of Au NPs is much lower than bulk Au materials and unstable at high temperature or high light intensity.¹⁵⁻¹⁷ The Tammann temperature of Au particles is 395 °C,¹⁸ namely, at temperatures higher than 395 °C, the Au particles begin to melt and aggregate. It was reported that the local temperature of Au particle surface would increase with the irradiation of visible light,¹⁹ and the higher intensity of visible light, the higher temperature of the Au particles. Therefore, with the further increase of visible light intensity to 0.44 W cm⁻², the local temperature of Au particles increased

Chapter 5

and the mobility of Au particles was enhanced, which resulted in the transformation of Au plasmon energy to its melt energy⁵ and ultimately decreased the catalytic performance.

From Fig. 5.13 it could also be observed that the catalytic performances over Au/SBA-15 and Rh-Au/SBA-15 exhibited similar trend with the variation of light intensity, on the other hand, with the light irradiation intensity of 0.22 W cm⁻², the catalytic activity over Rh-Au/SBA-15 (CH₄ conversion 2900 μmol g⁻¹ s⁻¹, CO₂ conversion 3600 μmol g⁻¹ s⁻¹) was much higher than the sum of those over Rh/SBA-15 (CH₄ conversion 2000 μmol g⁻¹ s⁻¹, CO₂ conversion 2100 μmol g⁻¹ s⁻¹) and Au/SBA-15 (CH₄ conversion 90 μmol g⁻¹ s⁻¹, CO₂ conversion 100 μmol g⁻¹ s⁻¹). The different catalytic activities over the catalysts were proposed to be related with the different reaction mechanisms.

For all the three catalysts except Au/SBA-15 which exhibited very low activity in DRM without light irradiation, the thermal catalytic mechanism was widely studied²⁰⁻²² and CH₄ and CO₂ were regarded to be activated via the Rh active sites through the steps (3) and (4), with products H₂, CO and water produced via steps (5)-(9).



For Rh/SBA-15 catalyst, due to the weak SPR effect of Rh NPs, even with the irradiation of visible light, the reaction was proposed to be proceeded via the

Chapter 5

thermally activated methods, steps (3) to (9). However, CO₂ activation was the rate-limiting step over Rh/SBA-15 catalyst.²³ Addition of Au promoter didn't improve the catalytic performance in DRM in the thermal catalytic process, whereas the catalytic activity was much improved with the irradiation of visible light (Fig. 5.13), indicating that the SPR effect mainly played the role of CO₂ activation.

As for Au/SBA-15 catalyst, it could be seen from Fig. 5.13 that, it exhibited nearly no activity without light irradiation. Since the cleavage of CH₄ was requisite to initiate the reaction^{20-22, 24} whereas Au has nearly no ability to break the C-H bond in CH₄.²⁵ In fact, the energy required to activate CH₄ was much higher than that for CO₂ activation.¹²⁻¹⁴ Then it could be predicated that CH₄ cleavage was the limiting step for DRM reaction over Au/SBA-15 catalyst. Rh NPs played important role of CH₄ activation. With light irradiation, both the conversions of CO₂ and CH₄ limitedly increased with the increase of light intensity from 0.0 to 0.22 W cm⁻² over Au/SBA-15 catalyst. CO₂ and CH₄ were electronically excited by the highly energetic plasmon electrons via steps (1) and (2), but not so effective without Rh NPs. In addition, compared with Rh-Au/SBA-15, the simulated electromagnetic field in Fig. 5.15 implied that there were fewer energetic electrons on Au/SBA-15 than Rh-Au/SBA-15 catalyst with the irradiation of visible light.

SPR excitation will also cause other effects, such as the surface polarization, electronic disturbance, or local heating effect on Rh NPs to enhance the catalytic activity because the DRM is susceptible to the surface characteristic of Rh NPs.

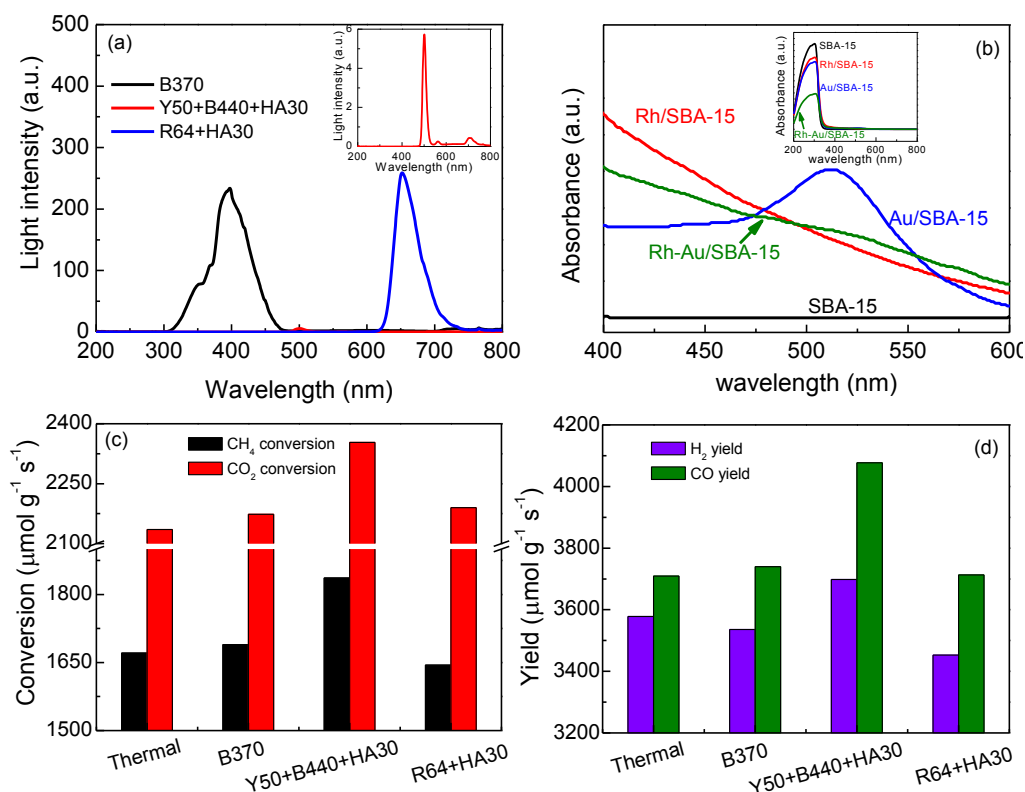


Fig. 5.14. (a) Wavelength range obtained with different filter set, (b) UV-vis spectra of catalysts, (c) CH₄ and CO₂ conversion and (d) H₂ and CO yield at photothermal reaction of different irradiation condition.

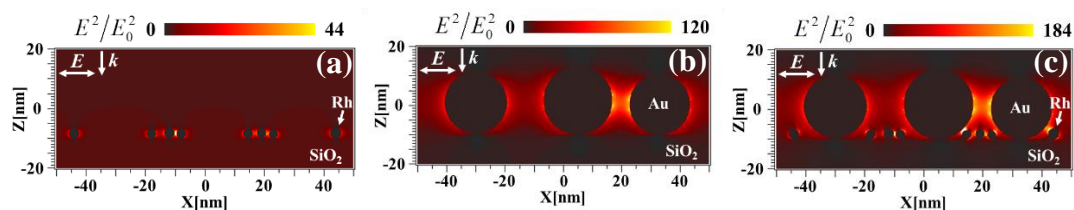


Fig. 5.15. Electromagnetic field distribution and enhancement simulated with the FDTD method. Electric field propagates along Z axis and oscillates along X axis. (a) Rh NPs on SiO₂, (b) Au NPs on SiO₂, and (c) Rh and Au NPs on SiO₂. In the presence of Au NPs, the intensity of SPR effect is obviously amplified. Excitation wavelength is 530 nm. The k indicates the wave-vector; the color scale bar shows the electric field enhancement.

5.4 Conclusions

Photothermal CO₂ conversion using H₂ as an active hydrogen source realized a much higher efficiency than conventional photocatalytic CO₂ reduction by water. This

Chapter 5

is based on two predominant features of Ru nanocatalysts, namely i) the highly efficient utilization of solar light and excellent photothermal performance, and ii) a unique activation ability for the hydrogenation of CO₂. CH₄ is a promising hydrogen for CO₂ conversion in DRM reaction due to an uphill reaction. Loading Au NPs effectively enhanced the catalytic performance of Rh catalyst for DRM at 500 °C under visible light. The intense SPR effect due to the interparticle coupling between the Rh NPs and the co-loaded Au NPs is speculated to enhance the rate-limiting step of DRM, i.e., activation of CO₂.

References

1. S. N. Habisreutinger, L. Schmidt-Mende and J. K. Stolarczyk, *Angew. Chem. Int. Ed.*, 2013, **52**, 7372-7408.
2. D. Pakhare and J. Spivey, *Chem. Soc. Rev.*, 2014.
3. S. Linic, P. Christopher and D. B. Ingram, *Nat. Mater.*, 2011, **10**, 911-921.
4. M. J. Kale, T. Avanesian and P. Christopher, *ACS Catal.*, 2014, **4**, 116-128.
5. Z. Xuming, C. Yu Lim, L. Ru-Shi and T. Din Ping, *Rep. Prog. Phys.*, 2013, **76**, 046401.
6. J. M. Sanz, D. Ortiz, R. Alcaraz de la Osa, J. M. Saiz, F. González, A. S. Brown, M. Losurdo, H. O. Everitt and F. Moreno, *J. Phys. Chem. C*, 2013, **117**, 19606-19615.
7. I. P. Silverwood, N. G. Hamilton, A. R. McFarlane, J. Kapitan, L. Hecht, E. L. Norris, R. Mark Ormerod, C. D. Frost, S. F. Parker and D. Lennon, *Phys. Chem. Chem. Phys.*, 2012, **14**, 15214-15225.
8. M. D. Malinsky, K. L. Kelly, G. C. Schatz and R. P. Van Duyne, *J. Am. Chem. Soc.*, 2001, **123**, 1471-1482.
9. S. K. Ghosh and T. Pal, *Chem. Rev.*, 2007, **107**, 4797-4862.

Chapter 5

10. C. Starkey, *Therapeutic modalities*, 4th edition, 2013, F.A. Davis Company, page 235.
11. S. Sun, W. Wang, L. Zhang, M. Shang and L. Wang, *Catal. Commun.*, 2009, **11**, 290-293.
12. A. Oumghar, J. C. Legrand, A. M. Diamy and N. Turillon, *Plasma Chem. Plasma Process.*, 1995, **15**, 87-107.
13. C.-j. Liu, R. Mallinson and L. Lobban, *J. Catal.*, 1998, **179**, 326-334.
14. C.-j. Liu, G.-h. Xu and T. Wang, *Fuel Process. Technol.*, 1999, **58**, 119-134.
15. P. Buffat and J. P. Borel, *Phys. Rev. A*, 1976, **13**, 2287-2298.
16. W. Luo, K. Su, K. Li, G. Liao, N. Hu and M. Jia, *J. Chem. Phys.*, 2012, **136**, 234704.
17. S. Link, C. Burda, M. B. Mohamed, B. Nikoobakht and M. A. El-Sayed, *J. Phys. Chem. A*, 1999, **103**, 1165-1170.
18. G. M. Veith, A. R. Lupini, S. Rashkeev, S. J. Pennycook, D. R. Mullins, V. Schwartz, C. A. Bridges and N. J. Dudney, *J. Catal.*, 2009, **262**, 92-101.
19. F. Wang, C. Li, H. Chen, R. Jiang, L.-D. Sun, Q. Li, J. Wang, J. C. Yu and C.-H. Yan, *J. Am. Chem. Soc.*, 2013, **135**, 5588-5601.
20. H. Y. Wang and C. T. Au, *Appl. Catal. A: Gen.*, 1997, **155**, 239-252.
21. J. Wei and E. Iglesia, *J. Catal.*, 2004, **224**, 370-383.
22. M. M. V. M. Souza, D. A. G. Aranda and M. Schmal, *J. Catal.*, 2001, **204**, 498-511.
23. J. Nakamura, K. Aikawa, K. Sato and T. Uchijima, *Catal. Lett.*, 1994, **25**, 265-270.
24. J. Z. Luo, Z. L. Yu, C. F. Ng and C. T. Au, *J. Catal.*, 2000, **194**, 198-210.
25. P. Ferreira-Aparicio, I. Rodríguez-Ramos, J. A. Anderson and A. Guerrero-Ruiz, *Appl. Catal. A: Gen.*, 2000, **202**, 183-196.

Chapter 6 General conclusions and future prospects

6.1 General conclusions

In this thesis, the main objective is to investigate the influence of surface reaction environment on the photo-induced reactions. The promotion effect of alkaline reaction environment on photocatalytic degradation, H₂ evolution and CO₂ reduction was studied. In these studies, alkaline environment demonstrated multiple functions, such as modulating surface band position of photocatalyst, accelerating rate-limiting steps, changing reaction pathway, etc. Besides, the influence of SPR on highly efficient CO₂ conversion with H₂ and CH₄ was investigated. The detailed results could be concluded in the following parts.

1. The influence of alkali modification on photocatalytic degradation performance of WO₃ under visible light.

WO₃ is an acidic oxide and unstable at alkaline environment. Alkali modification changed the surface structure of WO₃ through mild reaction, which induced an upshift of the surface energy band position and promoted the reduction of oxygen by photoexcited electrons. On the other hand, the alkaline surface environment suppressed the accumulation of H₂O₂ because H₂O₂ becomes reactive in alkali conditions. Decomposition of H₂O₂ produced reactive OOH⁻ which can further accept the photoexcited electrons. Therefore, for NaOH-loaded WO₃, photoexcited electrons

Chapter 6

and H_2O_2 intermediate can be consumed more easily, leading to stable and high activity of NaOH-loaded WO_3 for photocatalytic IPA degradation.

2. The influence of alkaline environment on photocatalytic H_2 production over plasmonic Au/ TiO_2 /Pt photocatalyst.

Alkaline environment modulation remarkably boosted H_2 production over Au/ TiO_2 /Pt photocatalyst under visible light. The photocatalytic reaction was mainly driven by the interband transition of plasmonic Au nanoparticles, and the apparent quantum efficiency of plasmon-assisted H_2 production at pH 14 reached 6% at 420 nm. The photoelectrochemical studies showed that alkaline environment promoted the photooxidation of alcohol over plasmonic Au NPs. This will accelerate the consumption of holes in Au NPs and suppress the recombination between hot electrons and holes, leading to improved H_2 evolution rate and high AQE of plasmonic photocatalysis.

3. The influence of alkali modification on photocatalytic CO_2 reduction over TiO_2 photocatalyst.

Due to the acidic nature of CO_2 molecules, surface modification of TiO_2 with alkali was found to be an effective way for the CO_2 adsorption and activation. Modification of alkali on TiO_2 also enhanced the photooxidation half-reaction by increasing the hydroxylation of TiO_2 surface, which also made contribution to effective conversion of CO_2 into CH_4 without loading any noble metal cocatalyst.

4. The influence of surface physical environment (SPR) on photothermal CO_2 conversion with H_2 and CH_4 .

Photothermal CO_2 conversion over Ru nanocatalyst using H_2 as an active hydrogen source realized a much higher efficiency than conventional photocatalytic CO_2 reduction by water. This is based on two predominant features of Ru

nanocatalysts, namely i) the highly efficient utilization of solar light and excellent photothermal performance, and ii) a unique activation ability for the hydrogenation of CO₂. However, this reaction was mainly driven by photo-induced thermal effect and no obvious photo-enhancement effect was observed. Compared with H₂, CH₄ is a promising hydrogen source for CO₂ conversion in DRM reaction due to an uphill reaction. Loading Au NPs effectively enhanced the catalytic performance of Rh catalyst for DRM at 500 °C under visible light. The intense SPR effect due to the interparticle coupling between the Rh NPs and the co-loaded Au NPs was speculated to enhance the activation of CO₂.

6.2 Future prospects

1 Influence of surface environment control on photocatalysis

Since the photocatalytic mechanism is equivalent to an electrochemical process in which the CB side can be regarded as a cathode, the VB side can be regarded as an anode, and the reaction is driven by the photovoltaic effect, the analysis of a photocatalytic reaction can be simplified into the analysis of two electrocatalytic redox reactions. Specifically, photocatalytic degradation, water splitting, and CO₂ reduction can be simplified into electrocatalytic ORR, organic oxidation, HER, water oxidation, CO₂ reduction and water oxidation, respectively. The experiences and results in the previous electrocatalysis studies on these reactions can be fully referenced in photocatalysis. Likewise, the results of the influence of reaction environment on a specific electrocatalytic reaction can be applied in photocatalytic reaction. Fortunately, electrocatalysis has achieved abundant research results in these aspects, which is very instructive to improve the performance of various

Chapter 6

photocatalytic systems in future.

This thesis mainly investigated the influence of alkaline environment on photocatalytic reactions. Photocatalytic reaction might be also modulated by other reagents. For an example, photocatalytic O₂ evolution reaction (OER) from water oxidation is a tough and key reaction in both overall water splitting and CO₂ reduction. Highly effective artificial photosynthesis must be based on efficient water oxidation in future. However, this reaction can only proceed effectively in the presence of sacrificial agent over limited kinds of photocatalysts to date. Some ions or small molecules, such as carbonates,^{1,2} phosphates,³ pyridine and its derivatives⁴ have been reported to effectively improve the OER performance of electrocatalysts. Phosphate ions in the liquid phase can also participate in the construction of electrocatalysts. As an example, CoPi (phosphate of cobalt) is a new type and excellent OER catalysts.³ It is also very interesting that an orthophosphate of silver, Ag₃PO₄, is the most effective material for photooxidation of water with very high AQE (~90%).⁵ The PO₄³⁻ ions may play important roles in the intermediate step of water oxidation beyond constructing the structure of electrocatalyst or photocatalyst. These ions or small molecules mentioned above can be potentially used as useful additives to enhance the efficiency of water oxidation half-reaction of future artificial photosynthesis systems.

In addition to photocatalytic OER, photocatalytic CO₂ conversion is also an important subject in artificial photosynthesis. Aqueous solution is commonly used reaction medium for photocatalytic or electrocatalytic CO₂ reduction. However, aqueous solution has two obvious drawbacks. The first is that the water reduction for hydrogen evolution reaction (HER) is a competitive reaction to CO₂ reduction. The second is that the solubility of CO₂ gas is very low in the aqueous phase. New type of

Chapter 6

solvent used in electrocatalytic CO₂ reduction might shine a light on photocatalytic CO₂ reduction (Table 6.1).⁶ These solvents show better solubility for CO₂ than that of aqueous media. Ionic liquids are also potential media for CO₂ capture and allow CO₂ reduction in very low overpotentials.⁷ All of these new types of solvents can potentially suppress H₂ formation and enhance CO₂ reduction efficiency.

Table 6.1 Solubility of CO₂ gas in various solvents at 298 K, 1 atm.⁶

Solvent	CO ₂ concentration [M]
Water	0.033
Methanol	0.06
Dimethylsulphoxide (DMSO)	0.135
Propylene Carbonate (PPC)	0.14
<i>N,N</i> -Dimethylformamide (DMF)	0.175
Tetrahydrofuran (THF)	0.211
Acetonitrile (AN)	0.28

2 The application of plasmonic nanometals for solar to chemical energy conversion

The control of surface environment not only include the chemical environment, but also the physical environment, such as the SPR enhanced catalysis through photothermal effect or local electrical field. SPR-mediated catalysis over plasmonic metal NPs shows promising prospects for highly efficient solar to chemical energy conversion. In addition to Group IB nanometals, Group VIII elements will attract new study interests. Because Group VIII and Group IB elements generally show catalytic performance intrinsically and involve extremely large category of thermocatalytic reactions, in principal, these thermocatalytic reactions can be directly transplanted to the photo-assisted reaction systems. Therefore, it is necessary to expand the

Chapter 6

application of plasmonic metal NPs by using more extensive kinds of transition metals to enhance the existing reaction rates, modulate the reaction selectivity, or open up new reaction pathways. The potential photo-enhancement effect and support effect in the SPR-mediated catalysis are worthy of further investigations. It can be anticipated that the SPR effect of plasmonic metal NPs will find applications in more extensive heterogeneous catalytic processes. Plasmonic metal NPs can convert the light into either e^-/h^+ pairs or heat to drive chemical reactions, which will increase the utilization efficiency of solar energy. This will be an important supplement to semiconductor photocatalysis towards practical solar-to-chemical conversion in future.

References

- 1.S. Koroidov, D. Shevela, T. Shutova, G. Samuelsson and J. Messinger, *Proc. Natl. Acad. Sci.*, 2014, **111**, 6299-6304.
- 2.Y. N. Kozlov, S. K. Zharmukhamedov, K. G. Tikhonov, J. Dasgupta, A. A. Kazakova, G. Charles Dismukes and V. V. Klimov, *Phys. Chem. Chem. Phys.*, 2004, **6**, 4905-4911.
- 3.M. W. Kanan and D. G. Nocera, *Science*, 2008, **321**, 1072-1075.
- 4.A. Yamaguchi, R. Inuzuka, T. Takashima, T. Hayashi, K. Hashimoto and R. Nakamura, *Nat. Commun.*, 2014, **5**, 4256.
- 5.Z. Yi, J. Ye, N. Kikugawa, T. Kako, S. Ouyang, H. Stuart-Williams, H. Yang, J. Cao, W. Luo, Z. Li, Y. Liu and R. L. Withers, *Nat. Mater.*, 2010, **9**, 559-564.
- 6.J. Lee, Y. Kwon, R. L. Machunda and H. J. Lee, *Chem-Asian J.*, 2009, **4**, 1516-1523.

Chapter 6

7.B. A. Rosen, A. Salehi-Khojin, M. R. Thorson, W. Zhu, D. T. Whipple, P. J. A.

Kenis and R. I. Masel, *Science*, 2011, **334**, 643-644.

Acknowledgement

Acknowledgement

I would like to express my sincere gratitude to my supervisor, Prof. Jinhua Ye. During my Ph. D course, Prof. Ye gave me meticulous direction about my research. My life and career has been changed since I was introduced into the field of photocatalysis. The understanding, encouragement and guidance from Prof. Ye made my achievements in the Ph. D course. I am also grateful to the platform of Catalytic Materials Group and various kinds of support from it.

I am also grateful to my supervisor, Prof. Tetsuya Kako and Naoto Umezawa. They gave me a lot of detailed and constructive suggestions based on their abundant knowledge of photocatalysis. These supports are very precious for my Ph. D study and lead to better understanding towards photocatalysis for me.

I would like to thank the members in Catalytic Materials Group in NIMS. I wish to express my warmest thanks to Dr. Li Peng and Shuxin Ouyang, who shared me with the fundamental knowledge and the experimental skills of photocatalysis. I also would like to thank Dr. Lequan Liu and Tao Wang, who shared me with the fundamental knowledge of thermocatalysis and electrocatalysis, respectively. They offered unselfish help and guidance in my research work. During Ph. D course, Ms. Haruna and Hagino provided me with best assistances in my experiments and daily life. I still wish to thank Miss Yu Qing and the other companions working together for their helps in my daily life. They let me live a happy life in Japan.

I wish to thank my parents and sister for their constant support and encouragement in all my Ph. D endeavors.